

PLASMONIC-ENHANCED FLUORESCENT CONJUGATED POLYMER  
CHEMOSENSOR FOR ULTRA-SENSITIVE DETECTION OF NITROAROMATIC  
VAPORS

---

A Dissertation  
presented to the Faculty of the Graduate School  
University of Missouri-Columbia

---

In Partial Fulfillment  
of the Requirements for the Degree  
Doctor of Philosophy

---

by  
CHARLES MATTHEW DARR  
Dr. Shubhra Gangopadhyay and Dr. Luis Polo-Parada, Dissertation Supervisors

DECEMBER 2014

© Charles Matthew Darr, 2014

The undersigned, appointed by the Dean of the Graduate School,  
have examined the dissertation entitled

**PLASMONIC-ENHANCED FLUORESCENT CONJUGATED POLYMER  
CHEMOSENSOR FOR ULTRA-SENSITIVE DETECTION OF NITROAROMATIC  
VAPORS**

Presented by Charles M. Darr

A candidate for the degree of Doctor of Philosophy

And hereby certify that in their opinion it is worthy of acceptance.

---

Dr. Shubhra Gangopadhyay (Co-Advisor)  
Department of Bioengineering  
Department of Electrical and Computer Engineering

---

Dr. Luis Polo-Parada (Co-Advisor)  
Department of Bioengineering  
Department of Molecular Pathology and Physiology

---

Dr. Sheila Grant,  
Department of Bioengineering

---

Dr. Gary Baker,  
Department of Chemistry

This work is dedicated to the people who have stood before me, behind me, and around me, who have guided me along the path to knowledge and personal development.

## **ACKNOWLEDGEMENTS**

I would first and foremost like to acknowledge the guidance and support of my co-advisors Dr. Shubhra Gangopadhyay and Dr. Luis Polo-Parada. Dr. Gangopadhyay has been a continual source of guidance, motivation, and support during the course of this study. She has provided an amazing facility and academic environment in which to learn and interact with colleagues from all over the world and to gain a better understanding of nanotechnology research. She also afforded me the opportunity to be involved in significant administrative projects for the group, including writing and editing proposals and papers as well as grant maintenance, which have been an immense education to that aspect of academic life.

Dr. Polo-Parada has been a great source of inspiration for performing interdisciplinary research in nanotechnology from a biological background and example of ingenuity, self-reliance, and the balance between work and family. More than that, he has been a huge source of support and encouragement for me professionally and personally to persevere in my graduate studies and continue toward a career in research.

I would like to thank the other members of my committee, Dr. Sheila Grant and Dr. Gary Baker. Both have been enthusiastic and dutiful members of a larger support network for my research and career. I respect, admire, and appreciate their professional advice and opinions on my research, guidance, and constructive criticism. I also appreciate their continued guidance and support as I move on to the next step of my journey in science.

I would like to thank Dr. Venumadhav Korampally for his mentorship throughout this study. His enthusiasm, skill, and teaching ability helped develop my skills of interpretive observation, an invaluable skill in the field I would not have without him.

My sincere gratitude goes to all of my colleagues in Dr. Gangopadhyay's Research Group: Dr. Joseph Mathai, Dr. Sangho Bok, Dr. Sagnik Basuray, Dr. Rajagopalan Thiruvengadathan, Dr. Jorge Castorena-Gonzalez, Dr. Steven Hamm, Dr. Madhuri Korampally, Dr. Balavinayagam Ramalingam, Dr. Clay Staley, Kunal Bhatnagar, Biyan Chen, Adam Drewery, Saman Gheytani, Arnab Ghosh, Bryant Harris, Lining Huang, Jerry Leung, Vamsi Mamidi, Somik Mukherjee, Avinash Pathak, Francisco Ramirez, Kaveh Shervin, Shahab Shervin, Aaron Wood, and Haisheng Zheng. I would also like to thank administrative members Janice Rudeen, Audrey Clark, Jami Thompson, and Shirley Holdmeier. There are not enough words to acknowledge how much you have meant to me. My time here with all of you has been an incredible experience and your presence has made the late nights and long hours a little more bearable and enjoyable.

I would like to thank my family and friends for their support throughout this undertaking. Firstly, I want to extend every possible thanks to my wife, Dr. Kathryn Murphy Darr, for standing beside me, holding me up, making sure I was well-fed, and so much more. To my parents, Joseph and Elizabeth Darr, my grandparents Kelly and Jerry Kemp, and my brother William and his wife Lauren, thank you for being there for me no matter the hour. A heartfelt thanks also goes to my friends from The Crossing Church and Calvary Chapel of Saline County. Finally, I would like to thank my God for everything He has done in and through my life. I owe my success, my work, and my life to Him.

## **TABLE OF CONTENTS**

<b>ACKNOWLEDGEMENTS .....</b>	ii
<b>TABLE OF FIGURES.....</b>	viii
<b>LIST OF TABLES .....</b>	xii
<b>ABBREVIATIONS .....</b>	xiii
<b>ACADEMIC ABSTRACT .....</b>	xvi
<b>CHAPTER 1 INTRODUCTION .....</b>	1
<b>1.1 Motivation .....</b>	1
<b>1.2 Focus.....</b>	2
<b>1.3 Overview of Dissertation .....</b>	4
<b>CHAPTER 2 LITERATURE REVIEW .....</b>	7
<b>2.1 Introduction .....</b>	7
<b>2.2 Fluorescence and Fluorescence-based Sensing.....</b>	7
<b>2.2.1 Basics of Fluorescence .....</b>	7
<b>2.2.2 Fluorophores .....</b>	10
<b>2.2.3 Plasmonic Enhancement of Fluorescence .....</b>	11
<b>2.2.4 Fluorescence-based Sensing.....</b>	16
<b>2.2.5 Fluorescence Dynamics for Ratiometric Sensing.....</b>	17
<b>2.3 Detection of Nitroaromatic Compounds .....</b>	19
<b>2.3.1 Traditional Methods .....</b>	19
<b>2.3.2 Molecularly Imprinted Polymers.....</b>	20
<b>2.4 Conjugated Polymers.....</b>	22
<b>2.4.1 Introduction to Polymers .....</b>	22

2.4.2 Polymer Thin Film Stability .....	23
2.4.2 Conjugated Polymers.....	25
2.4.3 Fluorescence-based Sensing with Conjugated Polymers .....	27
<b>CHAPTER 3 PLASMONIC-ENHANCED CONJUGATED POLYMER FLUORESCENCE CHEMOSENSOR FOR TRACE NITROAROMATIC VAPOR DETECTION.....</b>	<b>30</b>
<b>3.1 Introduction .....</b>	<b>30</b>
<b>3.2 Experimental Section .....</b>	<b>34</b>
3.2.1 Chemicals and Materials .....	34
3.2.2 Substrate Preparation.....	34
3.2.3 Substrate Characterization.....	36
3.2.4 Intensity, Bleaching, and Long-term Stability.....	36
3.2.5 Response to Dinitrotoluene and other Nitro-containing Compounds .....	37
<b>3.3 Results and Discussion.....</b>	<b>38</b>
3.3.1 MEH-PPV Film Morphology .....	38
3.3.2 Photophysical Characterization .....	44
3.3.3 Optimization of SiO <sub>2</sub> -Coated Silicon .....	51
3.3.4 Fluorescence Characterization.....	52
3.3.5 Photostability .....	57
3.3.6 Exposure to Nitroaromatics .....	61
<b>3.4 Conclusions &amp; Future Direction .....</b>	<b>65</b>
<b>CHAPTER 4 MONITORING STEADY-STATE NITRO-AROMATIC VAPOR DIFFUSION THROUGH A HETEROGENEOUS LAMINATE THIN FILM .....</b>	<b>67</b>
<b>4.1 Introduction .....</b>	<b>67</b>
<b>4.2 Experimental Section .....</b>	<b>69</b>

4.2.1 Chemicals and Materials .....	69
4.2.2 Substrate Preparation.....	69
4.2.3 Response to Nitroaromatics.....	70
<b>4.3 Results and Discussion.....</b>	<b>71</b>
4.3.1 Response to Nitroaromatic Vapors.....	71
4.3.2 Comparison of Quenching Rates .....	74
4.3.3 Sensor Cross-reactivity to Other Nitroaromatics.....	76
<b>4.4 Conclusions .....</b>	<b>79</b>
<b>CHAPTER 5 CONCLUSIONS AND RECOMMENDATIONS FOR FUTURE WORK .....</b>	<b>80</b>
<b>5.1 Conclusions .....</b>	<b>80</b>
<b>5.2 Future Direction .....</b>	<b>81</b>
5.2.1 Surface Energy-Mediated Polymer Morphologies .....	81
5.2.2 Molecularly Imprinted Fluorescent Conjugated Polymers.....	83
<b>5.3 Wider Implications of Research .....</b>	<b>84</b>
<b>APPENDIX A A COMPARATIVE EVALUATION OF MICROARRAY SLIDES AS SUBSTRATES FOR THE DEVELOPMENT OF PROTEASE ASSAY BIOSENSORS .....</b>	<b>87</b>
<b>A-1 Introduction.....</b>	<b>87</b>
<b>A-2 Materials and Methods.....</b>	<b>88</b>
A-2-1 Slide Selection and Preparation .....	88
A-2-2 Protein Binding .....	89
A-2-3 Long-term Stability .....	90
A-2-4 Protease Assay .....	90
<b>A-3 Results .....</b>	<b>91</b>

A-3-1 Slide Selection and Protein Binding .....	91
A-3-2 Protease Assay .....	94
<b>A-4 Discussion.....</b>	<b>94</b>
<b>REFERENCES.....</b>	<b>98</b>
<b>VITA.....</b>	<b>118</b>

## **TABLE OF FIGURES**

Figure 2-1 Jablonski diagram showing electron transitions of a fluorophore from ground to excited states. Fluorescence is the primary (faster) transition while phosphorescence allows transition to a triplet (T1) state that decays on the order of tens of seconds. ( <a href="http://www.olympusmicro.com">http://www.olympusmicro.com</a> ).....	10
Figure 2-2 (A) Dispersion relation indicating the light line (blue) and surface plasmon condition (solid red) [70]; (B) Kretschmann and (C) Otto prism configurations for surface plasmon resonance ( <a href="https://en.wikipedia.org">wikipedia.org</a> ). .....	14
Figure 2-3 (a) Fluorescence and (b) bright-field images of Rhodamine 6G spin-cast on gratings with nano-gaps, note the gaps appear black under bright field, indicating low reflectance (i.e. coupling) of the light; (c) mean and (d) maximum fluorescence enhancement factors of nanostructured surfaces versus glass [65]. .....	16
Figure 2-4 (A) Common nitroaromatics and nitroamines [98]; (B) Charge transfer complex between TNT and APTES with associated absorbance curve overlapped with fluorescence of fluorescein (green) and ROX (red) dyes. Adapted from [99].....	20
Figure 2-5 AFM images of a 45 Å polystyrene film dewetting from silica [111].....	24
Figure 2-6 Common conjugated polymers ( <a href="https://photonicswiki.org">photonicswiki.org</a> ). ....	26
Figure 3-1 (A,B) Schematic of capped plasmonic-enhanced fluorescence-based chemosensor; (C-K) AFM images and height profile of the oxide-capped MEH-PPV thin films of various thicknesses on (C,F,I) SiO <sub>2</sub> -coated silicon, (D,G,J) flat silver, and (E,H,K) plasmonic silver gratings, respectively. ....	39
Figure 3-2 (A-D) Reflectance curves for capped MEH-PPV thin films on silver plasmonic gratings with respect to unmodified silver plasmonic gratings; (E) Theoretical (open) and experimental (solid) coupling maxima with experimental dispersion curves comparing capped MEH-PPV-coated silver gratings with unmodified silver gratings; (F) FDTD simulated maximum electric field components coupled at 15° for each MEH-PPV film thickness.....	45

Figure 3-3 FDTD simulations of reflectance of (A) unmodified silver plasmonic gratings and (B-D) gratings with increasing thickness of MEH-PPV thin films and 5 nm SiO <sub>2</sub> capping layer.....	47
Figure 3-4 Electromagnetic field results from FDTD simulations at 15° and the center of the excitation wavelength band used (475 nm).....	49
Figure 3-5 Electromagnetic field results from FDTD simulations at 15° and the 0-0 and 0-1 emission wavelengths for each capped film. ....	50
Figure 3-7 (A) Tunable oxide etch rates by AF:HF mixtures as calculated by Honeywell [138] and (B) Expected and observed etched oxide thicknesses using a 15:1 AF:HF mixture and beginning with 124 nm oxide thickness.....	51
Figure 3-6 Fluorescence spectra of uncapped 6.5 nm MEH-PPV thin films spun from 0.05% chloroform solution onto silicon oxide thin films of increasing thickness.....	51
Figure 3-8 MEH-PPV fluorescence of (A) chloroform solution (same for all concentrations used due to effect of high extinction coefficient); (B-E) Uncapped and capped 6.5 nm thin films on (B&C) SiO <sub>2</sub> -coated silicon and (D&E) silver plasmonic gratings; (F-I) Uncapped and capped 13 nm thin films on (F&G) SiO <sub>2</sub> -coated silicon and (H&I) silver plasmonic gratings; (J-M) Uncapped and capped 30 nm thin films on (J&K) SiO <sub>2</sub> -coated silicon and (L&M) silver plasmonic gratings. Peak intensities are the CPS intensity values scaled to 500 ms integration time and divided by 10,000 so that all values are on a common scale. ....	53
Figure 3-9 (A) Normalized fluorescence spectra of uncapped and capped 6.5 nm MEH-PPV thin films with respect to 0.05% (w/v) chloroform solution; (B-D) Fluorescence spectra and associated wavelength-specific grating fluorescence enhancement factors of capped MEH-PPV thin films; (E) Comparison of wavelength-specific fluorescence enhancement factors of MEH-PPV thin films on plasmonic gratings with respect to SiO <sub>2</sub> -coated silicon; (F) Mean enhancement factors of capped 6.5 nm MEH-PPV thin films on various substrates with respect to flat silver. ....	54
Figure 3-10 (A) Peak fluorescence intensity values of MEH-PPV thin films on different substrates; (B) Mean enhancement factors of MEH-PPV thin films on different substrates normalized to film on silica. ....	56
Figure 3-11 (A) Comparison of photodegradation of uncapped and capped MEH-PPV thin films on different substrates under constant illumination; (B) Long-term fluorescence	

stability of uncapped and capped MEH-PPV thin films on different substrates stored in dark, ambient conditions.....	58
Figure 3-12 (A-D) Fluorescence spectral evolution of uncapped and capped MEH-PPV thin films during continuous illumination; (A) Uncapped 6.5 nm film on optimized SiO <sub>2</sub> -coated silicon; (B) Capped 6.5 nm film on optimized SiO <sub>2</sub> -coated silicon; (C) Uncapped equivalent film on silver gratings; and (D) Capped equivalent film on silver gratings....	59
Figure 3-13 Quenching response and recovery of (A-C) uncapped and (D-F) capped (A&D) 6 nm, (B&E) 13 nm, and (C&F) 30 nm MEH-PPV thin films on silica.....	61
Figure 3-14 (A) Spectra of progressive fluorescence quenching of MEH-PPV on SiO <sub>2</sub> -coated silicon (black) and plasmonic gratings (blue) by exposure to 2,4-DNT; (B) Quenching of capped MEH-PPV films on SiO <sub>2</sub> -coated silicon, flat silver, and silver plasmonic gratings(Inset); (C) Band diagram showing competing interactions of MEH-PPV, Silver, and 2,4-DNT in the grating setup; and (D) Recovery of capped MEH-PPV films on SiO <sub>2</sub> -coated silicon and silver substrates after 30 s quenching by 2,4-DNT....	63
Figure 3-15 Long-term fluorescence recovery after quenching by DNT. ....	64
Figure 4-1 Fluorescence images of capped 6.5 nm MEH-PPV thin film on SiO <sub>2</sub> -coated silicon on exposure to saturated 2,4-DNT vapor. Image Parameters: 10× objective, 475 nm excitation, 25% and 6% ND filters, 100 ms exposure time, and 200× gain.....	71
Figure 4-2 (A-C) Box-and-whisker plots of quenched spot areas of (A) 6.5 nm, (B) 13 nm, and (C) 30 nm capped MEH-PPV thin films after exposure to 2,4-DNT vapor. ....	72
Figure 4-3 Box-and-whisker plots from Figure 4-2 focused on means (□), numerical population 25/75 percentiles (boxes), and whiskers (outliers). ....	73
Figure 4-4 (A & B) Modified Stern-Volmer plots showing quenching rate of capped MEH-PPV thin films with exposure time to 2,4-DNT (line in B represents fit of linear region). ....	76
Figure 4-5 (A & B) Fluorescence quenching response to different nitroaromatic vapors of MEH-PPV thin films on (A) SiO <sub>2</sub> -coated silicon and (B) silver plasmonic gratings; (C & D) Modified Stern-Volmer plots for (A) and (B), respectively (Note: Curves in A & B are guides to the eye. Curves in C & D represent linear fits to initial points for rate calculation). ....	78

Figure A-1 (A) SNAP fluorescence intensities on different slide substrates (AL - aldehyde, E - epoxysilane, H - hydrogel, P - polymer, T - GPTS) (n=5); Optical micrographs of spots on Slide P without (B) and with (C) glycerol and humidity chamber; (D) Effect of increasing both SNAP and wash buffer surfactant concentrations on mean fluorescence intensity (% indicate concentration of surfactant in wash buffers before and after SNAP incubation) (n=10, FITC fluorescence intensity expressed as mean  $\pm$  SE). ..... 91

Figure A-2 (A) Effect of buffer additives on fluorescence stability at 37 °C (G = 0.5% Glycerol, P = 0.05% PVP, T = 0.5% Trehalose); (B) Effect of buffer additives on long-term binding stability at 4 °C (spotting/storage additives: black = Glycerol/HEPES, red = Glycerol/PVP, green = PVP/HEPES, blue = PVP/PVP), (Inset) Initial intensity of chips spotted with unmodified HEPES (black), HEPES + Glycerol (red), and HEPES + PVP (blue). ..... 93

Figure A-3 (A) Assay schematic and (B) Results of 2-hr assay of BoNTA light chain (● = 2 hrs, ▲ = 4 hrs, ▼ = 12 hrs) ..... 94

## **LIST OF TABLES**

Table 3-1 Concentration-dependent MEH-PPV Thickness on SiO <sub>2</sub> .....	42
Table 3-2 Sample Surface Roughness, R <sub>a</sub> ± SD (nm) .....	42
Table 3-3 Summary of Grating Reflectance Dip Locations and Associated Quality Factors. .....	46
Table 3-4 Peak Positions and Relative Intensities of 0.05% MEH-PPV Thin Film Fluorescence .....	55
Table 4-1 Summary of Optical and Electrochemical Properties of Reactants and Reaction Rates.....	79

## **ABBREVIATIONS**

1,3-DNB – 1,3-Dinitrobenzene

2,4-DNT – 2,4-Dinitrotoluene

2,6-DNT – 2,6-Dinitrotoluene

AFM – Atomic force microscope

APTES – 3-(Aminopropyl)-triethoxysilane

BOE – Buffered oxide etchant

BoNTA – Botulinum neurotoxin A

BuPA - Poly[1-(*p*-*n*-butylphenyl)-2-phenylacetylene]

CJP – Conjugated polymer

DET – Dexter energy transfer

DNA – Deoxyribonucleic acid

DNT - Dinitrotoluene

DP10-PPV - Poly(2,3-diphenyl-5-*n*-decyl-*p*-phenylenevinylene)

ELISA – Enzyme-linked immunosorbent assay

FCP – Fluorescent conjugated polymer

FDTD – Finite-difference time-domain

FITC – Fluorescein isothiocyanate

FRET – Förster resonance energy transfer

GPTS - 3-(Glycidoxypipethyl)-trimethoxysilane

HEPES - 4-(2-hydroxyethyl)-1-piperazineethanesulfonic acid

HOMO – Highest occupied molecular orbital

IED – Improvised explosive device

IFA – Immunofluorescence assay

ITO – Indium tin oxide

LSPR – Localized surface plasmon resonance

LUMO – Lowest unoccupied molecular orbital

MEF – Metal-enhanced fluorescence

MEH-PPV - Poly-[2-methoxy-5-(2-ethylhexyloxy)-*p*-phenylenevinylene]

MIP – Molecularly imprinted polymer

NA – Nitroaromatic

NB – Nitrobenzene

NHS – *N*-hydroxysuccinimide

OLED – Organic light-emitting diode

OTS - Octodecyltrichlorosilane

PDMS – Polydimethylsiloxane

PMSSQ - Polymethylsilsesquioxane

PMT – Photomultiplier tube

PVD – Physical vapor deposition

PVP – Polyvinylpyrrolidone

R6G – Rhodamine 6G

RET – Resonance energy transfer

RF – Radio frequency

ROX – Rhodamine X

SAM – Self-assembled monolayer

SET – Surface energy transfer

SNAP – Synaptosomal associated protein 25

SNR – Signal-to-noise ratio

SPCE – Surface plasmon-coupled emission

SPP – Surface plasmon polariton

SPR – Surface plasmon resonance

STP – Standard temperature and pressure

TNT – 2,4,6-Trinitrotoluene

UXO – Unexploded ordnance

VASE – Variable angle spectroscopic ellipsometry

VP – Vapor pressure

## **ACADEMIC ABSTRACT**

Rapid degradation of fluorescent conjugated polymers in ambient conditions imposes severe restrictions on their utility for long-term, portable sensing applications. This dissertation discusses the combined use of low-density, ultra-thin oxide capping layers and plasmonic silver gratings as a means of improving the utility of fluorescent conjugated polymer ultra-thin films (<50 nm) for long-term, portable chem/bio sensing applications. Silver gratings produced by a low-cost micro-contact printing method enhanced emission of poly-[2-methoxy-5-(2-ethylhexyloxy)-p-phenylenevinylene] (MEH-PPV) by as much as 12-fold with respect to films on flat silver through a mechanism of surface plasmon-coupled emission, which directs specific emitted wavelengths toward the detection window of the fluorescence microscope. Addition of a low-density, ultra-thin silica capping layer ( $d = 5.07\text{ nm}$ ,  $n = 1.38$ ) improved MEH-PPV photostability significantly with respect to uncapped films under both short-term continuous illumination as well as long-term storage in dark, ambient air, while retaining a rapid quenching response to nitroaromatic vapors. Capped, plasmonic-enhanced MEH-PPV film showed a response to 2,4-dinitrotoluene vapor at a rate more than 7-fold faster than capped films on  $\text{SiO}_2$ -coated silicon, attributed to a combination of sensitization effects of the silver on the conjugated polymer molecules in close proximity to the metal. Lateral diffusion of nitroaromatic vapor into the film is tracked by monitoring growth of quenched regions through fluorescence imaging. Most importantly, the devices recover fluorescence spontaneously on removal from the

nitroaromatic vapor source, suggesting they could be used for long-term, real-time measurements of nitroaromatic vapors.

# CHAPTER 1 INTRODUCTION

## 1.1 Motivation

Maslow's hierarchy of need places securing the safety of self and family as the second most basic need after physiological well-being [1]. Establishing a secure local environment is weighted so heavily in the hierarchy because protection from the ‘elements’ and predation is essential to ensuring the survival of progeny and, by extension, the fitness and persistence of a species. Thus, there is a very high natural prerogative to provide for safety. A very large portion of providing safety involves the detection or *sensing* of external or internal physical, chemical, and biological threats to physiological homeostasis [2]. Such detection is innate to human existence; each of the senses is designed to provide some form of feedback and physical information about safe and unsafe stimuli. Unfortunately, the senses are only well-developed enough to identify external threats that have reached a sufficient threshold level as to invoke sensation and reflex or response and internalized chemical, viral, or bacterial threats that have progressed to a symptomatic level of pathogenesis. Innate and acquired immunity as well as intrinsically selective semipermeable cell membranes mitigate the effects of some contaminants and pathological threats, but others retain their effectiveness in spite of these specialized systems. The development of artificially derived or concentrated chemical and biological threats has further confounded our innate or natural protections [3]. Not only have threats increased in potency to a point where the pathological dose is lower than what is detectable by simple physiological cues, but the ramifications of exposure to these threats have increased beyond what simple avoidance can afford or a brief recovery period can cure [4]. As such, some

means of detecting and identifying chemical and biological threats below their threshold pathological levels is of critical importance to modern day needs in the areas of medicine, homeland defense, and personal protection. Various defensive capabilities have been developed to meet the unique challenges of today's threats including personal protective equipment to isolate an individual or group from a threat, countermeasures to lessen the effects of a threat, and sensor systems for early detection and identification of a threat. Among these three options, sensors offer the ability to identify threats at sub-pathological levels and, thus, the greatest opportunity to prevent threat exposure or identify the threat to which a person is exposed [3, 5-10]. Development of ever more accurate, rapid, and sensitive sensors is critical to ensuring future safety and security and is the motivation for the research presented herein.

## **1.2 Focus**

The development of rapid, sensitive, compound-specific sensors is prevalent in every area of diagnostics research, including defense against unexploded ordnance, improvised explosive devices, and dangerous chemical run-off in our lakes, streams, groundwater, and other waterways [6, 8, 9, 11-16]. While novel explosives continue to be developed, a great majority still utilize traditional energetic compounds such as trinitrotoluene (TNT). Thus, the emphasis of much nitroaromatic sensor research is on identifying ways to detect and quantify the presence of this compound and its more prevalent degradation byproducts (e.g. 2,4- and 2,6- dinitrotoluene, DNT) [11, 13, 15-17]. Nitroaromatic sensors function on the observable interaction of nitroaromatic compounds with electron donors under specific environmental conditions, as will be discussed more

fully in the following chapters. The focus of this dissertation is the development of a nanostructure-enhanced fluorescence-based sensor for the detection of trace quantities of vapor-phase nitroaromatic compounds. Central to the function of this chemical sensor is the fluorescent conjugated polymer poly-[2-methoxy-5-(2-ethylhexyloxy)-p-phenylenevinylene] (MEH-PPV), which has shown promise as an optoelectronic signal transducer indicating the presence of nitroaromatic compounds [6, 11-13, 17, 18]. As with plasmonic silver gratings and ultra-thin oxide capping layers for the purpose of ultra-sensitive nitroaromatic vapor detection.

Sensor development in the modern era is pushing towards detection of ever smaller quantities of threat agents, rapidly approaching the critical limit of single molecule detection from a bulk environment [16, 19, 20]. Such an extreme level of sensitivity has been deemed necessary to address current infrastructure and military needs to allow advance warning or rapid confirmation of the presence of threat agents in high-population, high-stress, and low-resource environments with rapidly changing conditions (e.g. public venues, airport checkpoints, battlefield, etc.).

Approaching the single molecule level of sensitivity raises a number of critical questions about the sensor design itself. First, and foremost, a single analyte interaction event must be capable of producing an observable change in the transducer signal properties to indicate presence and, if necessary, activity of that analyte. Furthermore, the signal change must be statistically significant over and above the noise and signal drift resulting from interfering analytes as well as thermal, electrical, and chemical changes to the sensor transducer (i.e. thermal noise, dark noise, oxidation/reduction reactions, etc.).

This statistical significance is defined by the sensor signal-to-noise ratio (SNR) [21, 22], a parameter that will be a major focus of this dissertation. Isolating and positively identifying positive events in light of the myriad noise sources, in other words increasing SNR, is a massive undertaking, resulting in decades of thoughtful research on every aspect of sensor design from the signal transducer itself to signal amplification processes.

Signal amplification by post-transduction processing dominates the current market in terms of number of available products and techniques, including photomultiplier tubes (PMTs) for optical signals and digital signal processing through digital gain and increased integration time [23]. Unfortunately, these forms of signal processing amplify not only the positive signal to be detected, but also the noise associated with that signal. Noise in this sense refers to background electrical or optical signal that can be produced by defects in the electronics (i.e. dark current), thermal noise, shot noise, as well as competing, non-diagnostic signals coming from the sample. Instead, the focus has turned to systems that provide *intrinsic* signal amplification, which refers to direct modulation of signal inputs or outputs to increase the analyte-positive sensor signal emitted or transduced without resorting to bulk amplification of the entire sensor signal stream [20, 24, 25]. The exact mode of detection depends on the particular physicochemical properties and activity of the threat agent, often taking the form of an apportioned real or artificial chemical or biological substrate of activity.

### **1.3 Overview of Dissertation**

The present work is centered on the integration of conjugated polymers with plasmonic silver gratings and ultra-thin oxide capping layers for the fabrication of an ultra-

sensitive fluorescence chemosensor capable of rapid trace nitroaromatic vapor detection. Chapter 2 comprises a review of the literature on a number of topics related to the development of this sensor with particular focus placed on the phenomena responsible for the function and benefit the described sensor system has with respect to previous designs. This review includes an introduction to fluorescence and fluorescence-based sensors, the development and unique photophysics of fluorescent conjugated polymers that make them such powerful transducers for nitroaromatic detection, the basic surface plasmon resonance theory, and an overview of nitroaromatic sensors research as it has progressed so far. Particular emphasis in the review is placed on the phenomena responsible for the function and benefit of the described sensor system over previous attempts.

Following the review, Chapter 3 presents the design, integration, and further development of the plasmonic-enhanced conjugated polymer chemosensor and semipermeable, ultra-thin silicon oxide capping layer for enhanced polymer stability against photooxidation. Attention is given to the specific design parameters that dictate the function of the sensor and the importance of the plasmonic grating platform to the enhancement of conjugated polymer fluorescence through surface plasmon-coupled emission. Characterization of the ultra-thin silicon oxide layer will show how stopping the deposition process at such an early stage allows for protection against atmospheric oxygen and moisture while simultaneously allowing the nitroaromatic vapors access to the sensitive conjugated polymer beneath.

Chapter 4 is dedicated to describing a unique phenomenon associated with diffusion of the nitroaromatics through the disconnected porosity of the silicon oxide capping layer.

While the spectroscopic scans integrated entire sensor areas several tens of microns in diameter, the fluorescence images capture the infiltration of nitroaromatics into individual pores or pore groups through preferred fluorescence quenching at ‘nodes’ throughout the imaged area. These nodes grow and analysis of this growth elucidated further information about diffusion of nitroaromatics through the conjugated polymer film, which can be used to expand knowledge of the interactions involved in the quenching process.

Chapter 5 provides conclusions derived from the previous chapters and expands the discussion of the importance and potential applications of these results to further study. Attention is given to the applicability of the integrated capped plasmonic platform design toward enhancement of other fluorescence or optical sensor systems plagued by oxidative damage. Finally, future directions for the research are provided with recommendations for immediate and long-term experiments to expand on the research described.

# **CHAPTER 2 LITERATURE REVIEW**

## **2.1 Introduction**

Generally, sensors are tools that measure and respond to some quantity of input [3, 5, 7, 12, 13]. This response can take the form of a physical reaction to the input through linkage with an actuator or conversion of the input event into a signal capable of observation. The possible inputs are numerous and include physical or chemical pressures as well as the mere presence of chemical or biological moieties of every level of complexity. Although responses need not be observable, inputs are usually transduced by some piezoelectric, electrochemical, or optical means into a characteristic observable signal capable of determining input quantity or quality by thorough calibration. Signal transducers for chemical and biological sensors typically consist of platforms loaded with moieties capable of recognizing and responding to part or all of a threat agent. One of the most common signal transducers for chemical and biological sensor systems is fluorescence [9, 10, 14, 15, 26, 27], a process of light absorption and emission as will be described in Section 2.2.

## **2.2 Fluorescence and Fluorescence-based Sensing**

### **2.2.1 Basics of Fluorescence**

Luminescence is the emission of light from a molecule or supramolecular complex after an input of energy through excitation by an internal or external energy source [28]. The luminescence phenomenon is distinct from incandescence in that the excitation/emission process is not strongly related to the temperature of the molecule [29].

Rather, energy is transferred from the source to an electron in the molecule (i.e. absorbed) to excite it to a higher energy state and then re-emitted as light as the electron falls back to its resting energy state. Luminescence is divided into a number of classes defined by the unique forms of excitation and emission phenomena. Excitation sources include chemical reactions [30, 31], electrical (i.e. current) sources [32-36], mechanical stresses and forces [37], thermal [38], as well as incident photons [34, 39]. Molecular excitation by chemical reactions produces chemiluminescence, as in the reaction of iron with luminol in forensic blood detection assays as well as bis-(2,4,5-trichloro-6-carbopentoxyphenyl) oxalate (CPPO) reaction with hydrogen peroxide in glow sticks [40]. Chemiluminescence occurring within living organisms is further classified as bioluminescence [41, 42], the most prominent example thereof being the luciferase-mediated oxidation of luciferin as evinced by Lampyridae fireflies and others [43]. Photoluminescence (PL) is the form of luminescence whereby light is emitted from a molecule after absorption of a photon [34, 39]. PL is broken down into two further classes based on the nature of the excited state: fluorescence and phosphorescence for short- and long-lived excited states, respectively [28]. Of these two classes, fluorescence is far more sensitive to measure in response to the presence of analytes of interest due to its shorter lifetime ( $\tau$ ), meaning less time in the excited state per excitation event. Whereas phosphorescence emission can occur over the course of seconds to hours post-excitation, fluorescence occurs on the order of nanoseconds. Thus, fluorescence is extremely sensitive to local environmental conditions (e.g. temperature, solvent, concentration both of fluorophore and of other solutes, etc.).

In physical terms, fluorescence and phosphorescence are photon emissions from a molecule (i.e. fluorophore) that occur as a result of a photon absorption-induced transition of an electron in the fluorophore to an excited energy state [28, 44, 45]. This process of absorption → excitation → relaxation → emission is often illustrated using a Jablonski diagram of the electron states and transitions (**Figure 2-1**). In the first step, an incident photon is absorbed by an electron sitting in a relaxed/ground state also known as the highest occupied molecular orbital (HOMO). This photon must have energy sufficient to bridge the band gap of the fluorophore from the HOMO ( $S_0$ ) to the lowest unoccupied molecular orbital (LUMO or excited state or  $S_1$ ). Within each electronic energy state ( $S_0, S_1, \dots$ ) are vibrational states labeled 0 – 5. These represent the high density of possible electron states the electron may take in each orbital. The absorbed photon excites the electron from the ground state  $S_0$  to the excited state  $S_1^*$ , where \* represents one of the many vibrational states (time scale  $\sim 10^{-15}$  s). From the  $S_1^*$  state, the electron will rapidly ( $\sim 10^{-12}$  s), nonradiatively relax to a lower vibrational energy level within the  $S_1$  state through a process of internal conversion. From  $S_1$ , the electron further relaxes back across the band gap to  $S_0$  ( $\sim 10^{-8}$  s). This much larger relaxation can result in the radiative emission of a photon, known as fluorescence, or through a number of pathways that do not result in photon emission such as nonradiative relaxation, quenching by another absorptive medium with appropriate band gap, or transition to a triplet state, which results in the much slower phosphorescence emission ( $\sim 10^1$  s). As can be seen from the ‘length’ of the arrows in the energy diagram, the emitted photon (shorter, red arrow) has lower energy than the incident photon. In terms of wavelength, lower energy results in a red-shifted photon from the

initial incident one, often leading to absorption of one ‘color’ and emission of another (i.e. blue absorption, green emission). This shift is known as Stokes’ shift [31] and can be exploited to identify the presence of fluorophores by separating the excitation and emission wavelengths through appropriate filter sets.

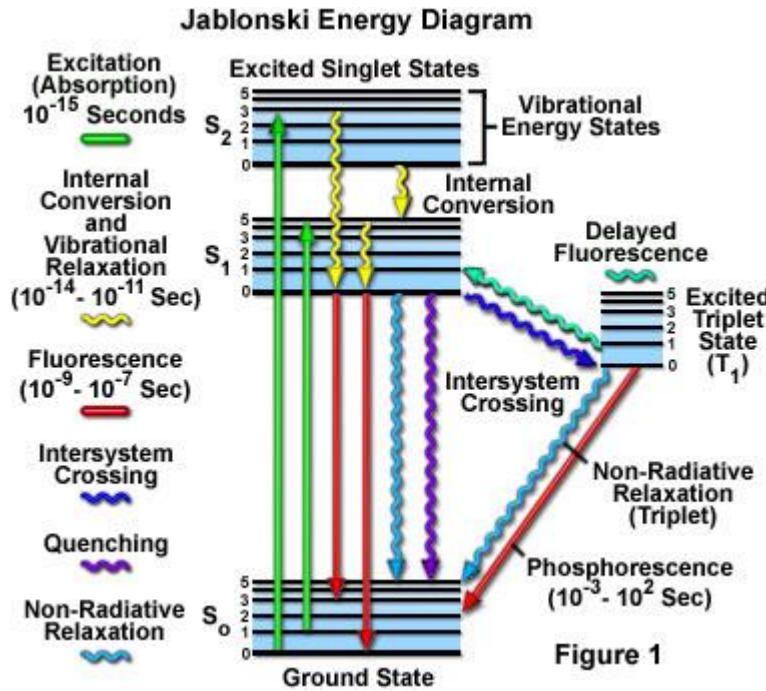


Figure 1

**Figure 2-1 Jablonski diagram showing electron transitions of a fluorophore from ground to excited states. Fluorescence is the primary (faster) transition while phosphorescence allows transition to a triplet (T<sub>1</sub>) state that decays on the order of tens of seconds. (<http://www.olympusmicro.com>).**

## 2.2.2 Fluorophores

Fluorophore design [46] is contingent upon providing an appropriate density of electron states such that that incident photons of the desired wavelength provide sufficient energy to jump the band gap between HOMO and LUMO levels to reach the excited state. This has been achieved most readily using organic dyes with numerous  $\pi$  bonds of carbon-carbon chains and rings and semiconductor nanoparticles (i.e. quantum dots), which have an appropriate band gap for excitation/emission at particular wavelengths [28, 29].

Organic fluorophores typically consist of interconnected aromatic ringed structures with various ligands (e.g. NH<sub>2</sub>, COO<sup>-</sup>, halides, etc.) attached around the core structure. Conjoining multiple ringed structures increases the density of states and allows for a lower band gap material, allowing electronic HOMO/LUMO excitation at lower energies, corresponding to longer wavelengths. For instance, the Coumarin family of UV-absorbing, blue-emitting dyes consists of a benzoyprone core with decorations leading to fine-tuning of the absorption/emission spectra [47] while the Rhodamine family, which absorbs blue-green and emits yellow-orange, consists of a fluorone core, again with decorations [25, 48, 49]. Fluorophores have been developed across the EM spectrum from Near-UV, across the visible range, and into the Near-IR part of the EM spectrum simply by tuning the number of conjoined rings, connectors, and decorating ligands to produce well-defined band gaps.

### 2.2.3 Plasmonic Enhancement of Fluorescence

Constraints on illumination intensity to reduce photobleaching, limits of modern low-cost photodetectors, and small number of fluorophores required to improve sensitivity all lead to low intrinsic fluorescence signal, which could quickly lead to low signal-to-noise ratio (SNR) and poor quantitation of NA vapor [6, 15, 50-52]. Several approaches have been developed to increase SNR, including improving photodetection systems through reduction of dark current and increasing the apparent emission output by engineering the underlying substrate to provide intrinsic signal amplification. A number of modalities to affect these improvements have been developed, but platforms incorporating some form of metal-enhanced fluorescence (MEF) have offered the most

significant signal enhancement values to date [53-55]. MEF comprises a number of effects metals can have on the photophysics of associated fluorophores, mainly increased excitation and radiative decay rates [53-55], but also increased non-radiative resonance energy transfer (RET) properties [56-58]. Chief among the mechanisms of MEF are localized and propagating surface plasmon resonance (SPR) occurring at the interface between a plasmonic active metal (e.g. gold, silver) and a dielectric layer (e.g. air, water) [5, 59-67]. Surface plasmons are defined as extant oscillating charges at a metal-dielectric interface [68]. These surface plasmon oscillations are intrinsic to the metal and are associated with the so-called plasma frequency ( $\omega_p$ ) that can be observed as a steep dip in reflectance measurements. Light at the plasma frequency is transmitted through the metal as the electrons in the metal are incapable of screening them. The plasma frequency is most often located in the UV region for silvered metals (e.g. silver, aluminum) and decreases in frequency (increases in wavelength) to the visible range for metals such as gold or copper [69]. Coupling incident photons to the surface plasmons requires rigorous matching of the optical momentum of the incident photon to the surface plasmon. When successful, resonance with the surface plasmons (i.e. SPR) is achieved and a surface plasmon polariton (SPP) is formed, an electromagnetic wave that propagates along the interface as well as to some depth into the dielectric or bulk medium.

Propagating SPPs rely on a delicate balance of several parameters including the dielectric constants of the interfacing materials and angle of incidence of the incoming light, but additional modification of the light is usually required to match the wavenumber of the existing oscillating plasmons at the metal-dielectric interface [5, 62]. The

conditional equation for coupling light to an extant surface plasmon at a smooth metal-dielectric interface is

$$k_{sp} = \frac{\omega}{c} \sqrt{\frac{\varepsilon_m \varepsilon_d}{\varepsilon_m + \varepsilon_d}} - (\text{Eq. 1})$$

where  $k_{sp}$  is the wave vector of the surface plasmon,  $\omega$  is the resonant frequency,  $c$  is the speed of light, and  $\varepsilon_m$  and  $\varepsilon_d$  are the dielectric constants of the metal and dielectric, respectively [70]. Generally, the surface plasmon resonance condition cannot be reached in free space as  $k_{sp}$  will be greater than the wave vector for the incident light ( $k_o = \omega/c$ ) for any particular frequency of incoming light (**Figure 2-2A**). Initial propagating SPP methods required the use of high-index prism coupling to account for the difference between the wave vector of the incoming light and the resonance wave vector of the oscillating plasmons in the metal, the most common being the Krestchmann and Otto configurations (**Figure 2-2B,C**) [66, 67]. This led to the modified dispersion relation equation

$$k_{sp} = \frac{\omega_o}{c} \sqrt{\frac{\varepsilon_1 \varepsilon_2}{\varepsilon_1 + \varepsilon_2}} = n_p \frac{\omega_o}{c} \sin \theta_p - (\text{Eq. 2})$$

where  $n_p$  is the index of the prism,  $\omega_o$  is the frequency of the incoming light, and  $\theta_p$  is the angle at which the light travels through the prism. However, periodically structured surfaces have also been shown to introduce additional momentum to the dispersion relation such that incident light can be coupled to SPPs in free space (i.e. without such bulky optical setups) [60-63, 65]. These extra terms are related to the grating order and pitch as seen in the grating dispersion relation

$$k_{sp} = \frac{\omega_o}{c} \sqrt{\frac{\varepsilon_1 \varepsilon_2}{\varepsilon_1 + \varepsilon_2}} = n_d \frac{\omega_o}{c} \sin \theta_{SPR} \pm \frac{2\pi m}{\Lambda} - (\text{Eq. 3})$$

where  $n_d$  is the refractive index of the dielectric (i.e.  $\sqrt{\epsilon_d}$ ),  $\theta_{SPR}$  is the angle of incidence,  $m$  is the diffraction order integer, and  $\Lambda$  is the grating pitch. Continuous, nanoscale periodic metallic gratings enable free space coupling of the incident photons to surface plasmons, making them keenly appropriate platforms for optical sensors. In fact, the angles required for coupling the visible wavelengths to the gratings are often within the acceptance cones of microscope objectives and microplate readers, making metallic gratings amenable surfaces for a number of chemical and biological sensing applications.

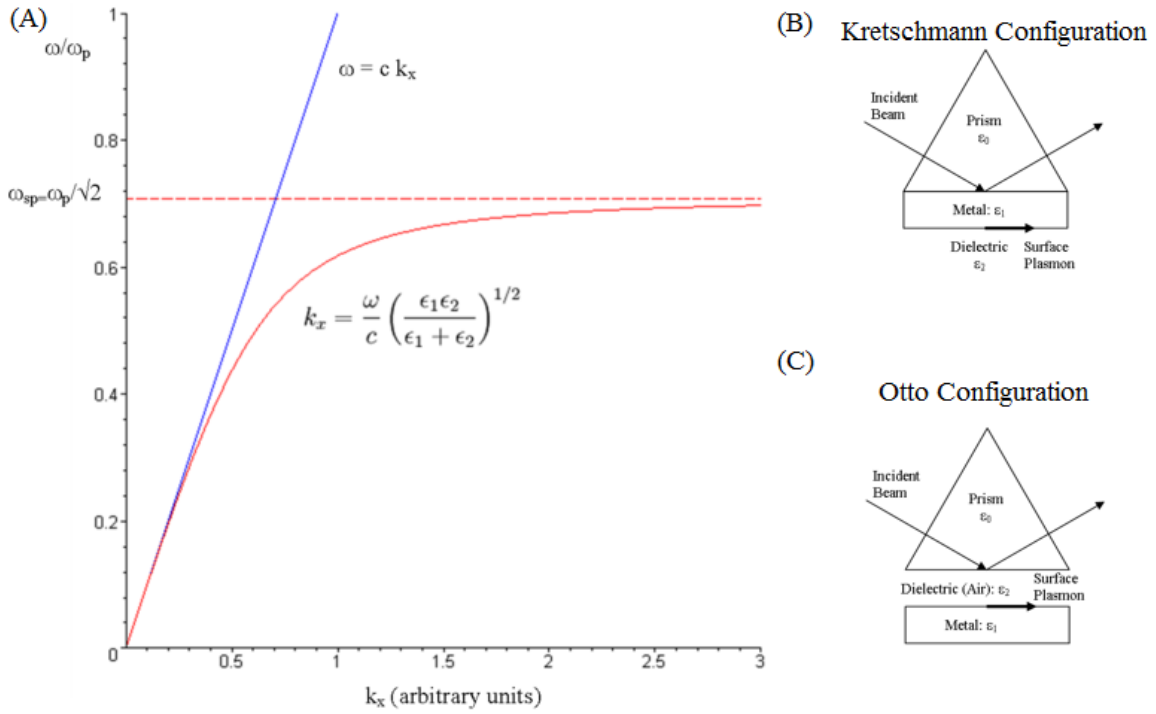


**Figure 2-2 (A)** Dispersion relation indicating the light line (blue) and surface plasmon condition (solid red) [70]; **(B)** Kretschmann and **(C)** Otto prism configurations for surface plasmon resonance ([wikipedia.org](https://en.wikipedia.org)).

SPR-enhanced fluorescence is achieved by incorporating the target fluorophore into or atop the dielectric layer with the exact mode of SPR enhancement determined primarily by the nanoscale structure of the metal layer. Metal nanoparticles and nano-islands exhibit localized surface plasmon effects (LSPR) [5, 57-59], while nanoscale

coalesced metal sheets and other continuous nanostructures produce a propagating surface plasmon polariton (SPP) [60-64]. SPPs have proven very useful for sensors as the plasmonic metal itself or interfacing dielectric coating can be used as the substrate for ligand attachment.

While metallic gratings have shown great promise as a uniform enhancing surface, their construction by electron beam lithography is prohibitively time-consuming and expensive for mass production of devices. In response to this need, our group has recently developed a micro-contact printing process that provides a backbone for metallic plasmonic gratings using the periodic structure inherent to CDs, DVDs, and HD-DVDs as the master template [65]. The master mold is used to prepare a stamp of polydimethylsiloxane (PDMS) and then the polymer ink (polymethylsilsesquioxane, PMSSQ) is spin-coated on the stamp and transferred to a cleaned glass slide or silicon wafer. The result is a highly stable PMSSQ ink grating with pitch  $\sim 395 \pm 5$  nm and height  $\sim 60 \pm 3$  nm. In addition to the grating structures, we have found that this micro-printing technique also results in spontaneous generation of nanoscale gaps as a result of stress that develops in the ink as the PDMS stamp is pressed and peeled off (**Figure 2-3A,B**). These nano-gap-embedded polymer gratings provide the foundation for the metallic gratings, which are produced by RF sputter deposition. After silver deposition, the incident light can be coupled resonantly to the surface plasmons in the gratings using specific wavelengths of light at their characteristic angles ( $\theta_{\text{SPR}}$ ) satisfying the equation above, as indicated by the dip in reflectance measured by ellipsometry. These gratings were shown to offer more than  $25\times$  average enhancement over glass while the nano-gap regions have

an enhancement factor nearly  $70\times$  that of glass (**Figure 2-3C**). Meanwhile, the maximum enhancement factor found for the gratings was  $\sim 36\times$  with respect to glass, while the highest nano-gap regions were almost  $120\times$  brighter than the fluorescence from glass, an increase of more than two orders of magnitude from the same concentration of dye (**Figure 2-3D**).

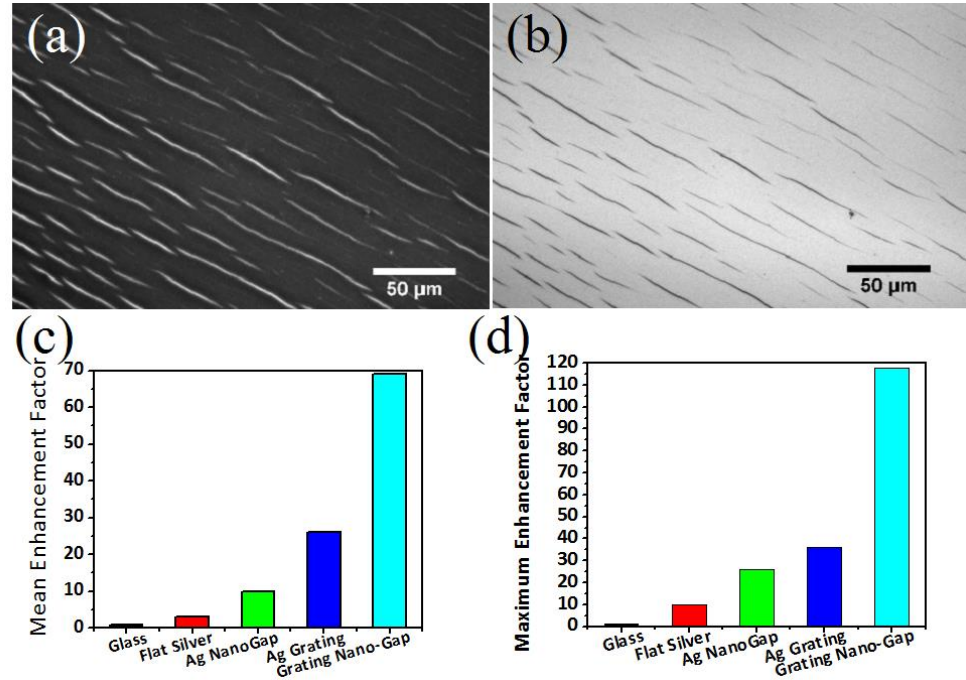


**Figure 2-3** (a) Fluorescence and (b) bright-field images of Rhodamine 6G spin-cast on gratings with nano-gaps, note the gaps appear black under bright field, indicating low reflectance (i.e. coupling) of the light; (c) mean and (d) maximum fluorescence enhancement factors of nanostructured surfaces versus glass [65].

#### 2.2.4 Fluorescence-based Sensing

As can be seen, fluorescence is a delicate, yet consistent property of organic and semiconductor fluorophores. With appropriate consideration for fluorophore stability, the Stokes' shifted fluorophore emission can be used to identify the presence and, in some cases, quantity of an analyte of interest in a sensor architecture. This requires functionalization of the fluorophore to an analyte-specific reagent, often taking the form of a chemical or biological substrate [10, 14, 71-75], reactive binding element such as

antibody or molecularly imprinted polymer [3, 7, 9, 14], or fluorophore design for intrinsic analyte sensitivity [48, 49]. In-depth examination of fluorophore emission dynamics can provide further information leading to more powerful sensor data than simply looking at base fluorescence emission intensity. Intensity alone is often considered a ‘weak’ measurement as the fluorescence is dependent upon excitation of a molecule existing in a bulk, often unknown fluid solution. The presence of interfering analytes or quencher molecules, changes in physical environmental properties (e.g. temperature, pressure, pH, fluid solvent polarity or solid surface energy), bleaching as a result of photon-induced disruption of the molecular structure by bonding to some outside moiety (e.g. oxidation), and even the enhancing effects of SPR coupling can all have a confounding impact on the intrinsic fluorescence emission properties of a fluorophore that disrupts any quantitative analysis one might perform on intensity alone.

#### 2.2.5 Fluorescence Dynamics for Ratiometric Sensing

Although intensity alone is ‘weak’ for analyte quantitation, sensor architectures that measure relative or ratiometric changes in fluorescence intensity between two (or more) time points can be used to assess the impact of the presence of analytes on the fluorophore system. This often takes the form of resonant energy transfer (RET) between the excited-state fluorophore (labeled as donor) and some other molecule (labeled as acceptor) capable of absorbing photons of energy associated with the donor emitted fluorescence. Förster described a specific mechanism for RET that occurs when appropriate donor/acceptor pairs are within close proximity and which decays with inverse-sixth power order of the fluorophore separation distance ( $1/R^6$ ) [76]. The acceptor molecule in Förster RET (FRET)

can be a quencher or another fluorophore that absorbs photons at the emitted wavelength. In case of quenching, the fluorescence dynamic is a lights off (interaction → quenching) or lights on (interaction → fluorescence recovery) [10, 14, 77]. In the case of an absorbing fluorophore as acceptor, donor fluorescence is exchanged for that of the acceptor so that fluorescence is observed farther red-shifted than the donor fluorescence [78, 79]. FRET efficiency measured as the relative intensity of the two dyes is an extremely powerful transducer as the transfer occurs on very short length scales and only with appropriate dipole-dipole orientation and spectral overlap [45, 78].

Other RET mechanisms exist including surface energy transfer (SET) [80], Dexter energy transfer (DET) [81], excimer/exciplex formation [82, 83], and contact/static quenching [84, 85]. SET refers to the aforementioned quenching of fluorescence by metallic surfaces [86, 87], which decays with distance  $1/R^4$  as opposed to the  $1/R^6$  dependence of FRET. Meanwhile, DET differs from FRET in that the excited state electron of the donor actually physically exchanges places with a ground state electron from the acceptor. This means that the transfer must occur on extremely short distance scales (typically,  $<1$  nm as opposed to  $\sim 10$  nm for FRET) and there must again be spectral overlap between the molecules. Excimer and static quenching are both processes in which a dimer is formed in the excited or ground state, respectively by  $\pi$ - $\pi$  bond, hydrophobic interaction or even covalent bonding. The difference between them is that excimer/exciplex supramolecular complex is only formed when the molecules are in the excited state whereas static quenching dimerization occurs in the ground state. This dimerization leads to a band gap shift sufficiently far from the incident photon that no

excitation of the new supramolecular complex can take place. Each of these quenching mechanisms has the effect of drastically reducing fluorescence intensity of the donor and can be used for detection of analytes. Herein, we will focus on fluorescence quenching for detection of vapor-phase nitroaromatic compounds.

## 2.3 Detection of Nitroaromatic Compounds

### 2.3.1 Traditional Methods

Trace vapor-phase detection of nitroaromatic (NA) compounds and their decomposition products is a central focus of sensor development for many defense applications including public venue security, detection of unexploded ordinance and improvised explosive devices, and remediation of environmental contamination (**Figure 2-4A**) [16]. Conventional methods to detect NA compounds exploit the partial electron deficiency afforded by their electron-withdrawing nitro groups to form observable color complexes through induced dipole formation (i.e. Meisenheimer Complex) or absorb photoelectrons through contact quenching or DET (**Figure 2-4B**) [8, 16, 88-90]. It is this property that allows most NA to absorb photoelectrons through nonradiative transfer (i.e. fluorescence quenching) [8, 16, 89, 90]. However, fluorescence-based NA vapor sensors have experienced a number of setbacks with regard to sensitivity and selectivity due to photodegradation and quenching by nonspecific, chemically similar analytes [14, 89-92]. The combined effect of low atmospheric vapor pressure of target NAs and large quantity of bulk fluorescent molecules inaccessible to the target quenchers means that the number of NA molecules required to effect an appreciable change in signal slows down the

detection process considerably. As such, these methods have proved insufficient to accomplish the goal of real-time *in situ* NA vapor detection.

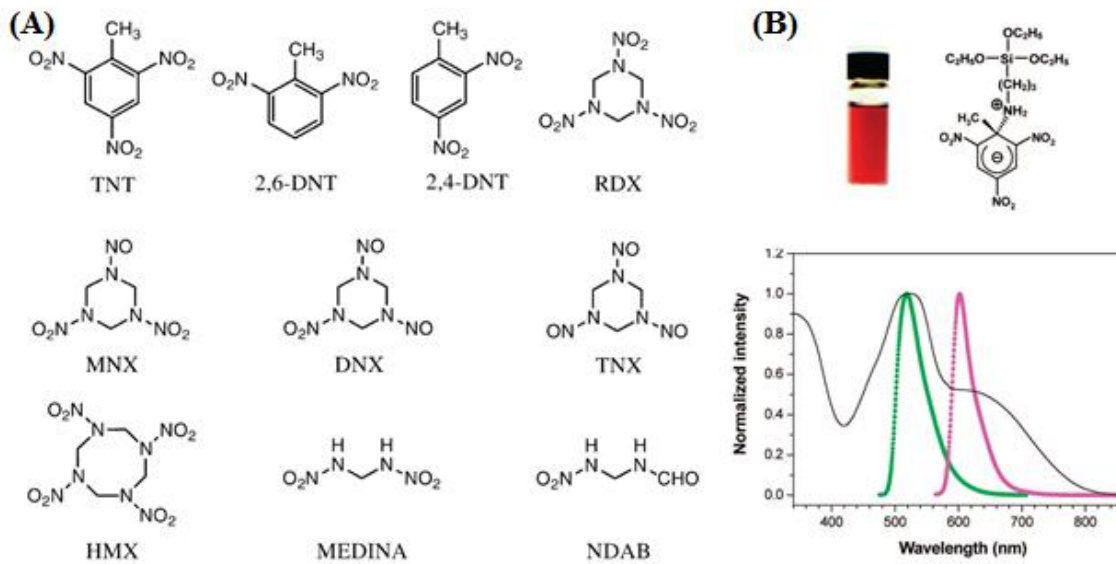


**Figure 2-4 (A) Common nitroaromatics and nitroamines [98]; (B) Charge transfer complex between TNT and APTES with associated absorbance curve overlapped with fluorescence of fluorescein (green) and ROX (red) dyes. Adapted from [99].**

### 2.3.2 Molecularly Imprinted Polymers

While fluorescence-based sensors have the potential to be quite powerful transducers of molecular interactions, traditional approaches applying fluorescence-based sensors to vapor-phase detection of NAs have experienced a number of significant issues forestalling the development of field-deployable sensors, especially sensitivity at trace levels and selectivity over chemically-similar analytes [8, 14, 89, 90, 92]. The low selectivity of some quenching-based sensors in general is due to the fact that there are several mechanisms by which fluorescence may be lost in the course of sensor use, including photodegradation and quenching by nonspecific electron-withdrawing groups (dubbed interfering analytes) such as nicotine [14, 89-92]. This issue has been addressed

to an extent by the advent of molecularly imprinted polymers (MIPs), a form of biomimicry that seeks to replicate the selectivity of protein-based sensors while circumventing the degradation issues of biologicals by replacing them with chemically-reactive porous sol gels [9, 50, 52, 91-97]. Briefly, functional monomers, in this case amine groups provided by 3-aminopropyltriethoxysilane (APTES), are combined with silica sol-gel precursors, the NA template, and NA-sensitive dyes [9, 50, 52]. The amine groups are known to form a charge transfer complex with NA molecules, which improve their spectral overlap with blue-green fluorescent molecules such as Fluorescein (FITC) and others [88, 91]. After reaction and template extraction, the remaining porous gel has a physicochemical binding site capable of capturing a NA molecule with some specificity over other molecules.

While MIPs improve selectivity significantly over unmodified thin films of fluorophores, sensitivity issues represent a much different class of engineering problem. Even MIP sensors can lack sensitivity in the field due to low signal-to-noise ratio (SNR), a result combining the low atmospheric vapor pressure of nitroaromatics (especially TNT and RDX) at typical temperatures encountered in the field, the one-for-one quenching response of FITC to NA, and the intensity of that single affected fluorophore relative to the unaffected bulk remaining [92, 100]. In order for the vapor concentrations encountered in typical real-world exposure events to have a meaningful impact on MIP fluorescence intensity, the number of fluorophores must be extremely small, corresponding to low signal and thus low SNRs.

## 2.4 Conjugated Polymers

### 2.4.1 Introduction to Polymers

Polymers are macromolecules comprising repeating subunits (i.e. monomers) joined together in environmental conditions conducive to reaction between activated functional groups at the ends of each monomer [101, 102]. This reaction can be promoted or controlled by temperature, pressure, the presence of catalysts, as well as the functional groups themselves, resulting in a polymer chain a number of subunits long determined by the specific reaction conditions. The resultant polymers can be classified by length, shape, backbone composition, and functional side groups. Length or degree of polymerization refers to the number of monomers making up the polymer and include dimers (two subunits), trimers (three subunits), and longer “n-mers” (n subunits) and is calculated by dividing the overall polymer molecular weight by that of the monomer ( $DP = M_n/M_o$ , where  $DP$  is the degree of polymerization,  $M_n$  is the molecular weight of the polymer, and  $M_o$  is the molecular weight of the monomer). Shapes include linear, star, combs, brushes, and many other composites of these. Bonds making up polymer backbones include organic carbon-carbon (C-C) bonds, peptide (C-N) bonds, or metal oxides (e.g. Si-O), among others. The side groups can be further organic or inorganic ligands and provide the polymer with specific functionality, miscibility, strength, and other physicochemical properties. Using a single monomer type can produce homopolymers while multiple monomer species result in copolymers. Considering polymers made of two different monomer species, labeled A and B, possible copolymer arrangements include alternating (A-B-A-B-), periodic (A-A-B-B-B-), block (A-A-A-B-B-B-), as well as grafted or branched versions of

each of the above. Generation of each of these polymer types requires careful consideration to the reactants and order of reaction, as well as proper reaction quenching to prevent over-extension of a particular polymer block or branch. Through appropriate design, polymers capable of extraordinary temporary or permanent higher order structures can be created [103, 104]. Indeed, most complex biomolecules including proteins and nucleic acids (DNA, RNA) can be considered as polymers [105-107].

#### 2.4.2 Polymer Thin Film Stability

Stable polymer solutions can be made in appropriate solvents provided a polymer or set of polymers is not auto-reactive (i.e. reactive with itself or other ligands present) at the chosen temperature, pressure and solvent conditions [102, 108-111]. Polymers can, thus, be mixed into complex, useful formulations (e.g. friction-resistant silicone grease), molded and die cast into solid forms (e.g. polyvinyl chloride, PVC, used in piping), or cast onto solid surfaces. The mechanisms of each of these possible end products relies on the interplay between functional groups and, more importantly, their associated surface energy densities with reference to that of the solvent and other compounds [75, 112-115]. Surface energy density refers to the excess energy at the surface boundary of a material with respect to the bulk of that material and is usually given in  $\text{J/m}^2$  or  $\text{mJ/m}^2$  [112, 113]. When the surface energy densities of the polymer and solvent are similar, surface formation can be energetically favored and so multiple surfaces can form and the materials “go into” solution. A similar process occurs for interfaces between polymers and solid surfaces, with successful surface formation called wetting the surface [111, 113, 116, 117]. Meanwhile, the polymer will be immiscible with a surface former if the difference in surface energy

densities is sufficiently large, resulting in aggregation and polymer collapse out of the solution phase (i.e. phase separation) or dewetting from a solid surface (**Figure 2-5**) and the formation of a contact angle with the surface higher than  $0^\circ$ .

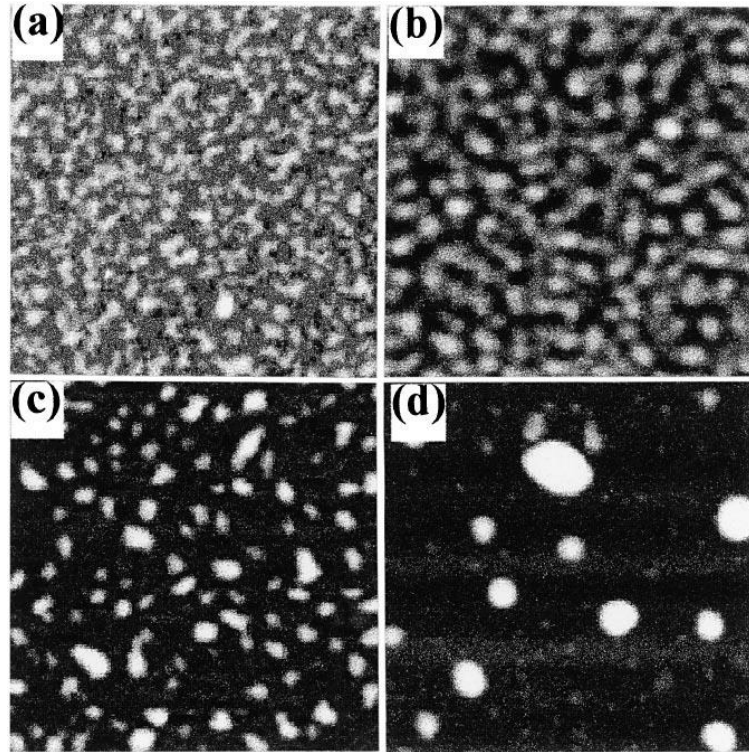


**Figure 2-5** AFM images of a 45 Å polystyrene film dewetting from silica [111].

The conditions for entropic collapse of the polymer away from the interfacing material are defined by a complex relationship between thermal energy, composition, and surface energy densities that are often described by a spinodal curve. The term ‘spinodal’ refers to the set of critical temperatures and relative pressures bounding the regions where metastable mixtures can exist. Outside of the spinodal, phase separation is inevitable. Spinodal decomposition is the phase separation of mixtures of two immiscible or only conditionally miscible liquids (e.g. oil and water) while spinodal dewetting is the related thin film-surface phenomenon [116, 117]. In the case of liquid-solid interfaces, droplet

formation is virtually instantaneous (e.g. water contact angle  $\geq 90^\circ$  on hydrophobic surfaces) due to the motility of the material in liquid form. In the polymer thin film case, materials with high contrast in surface energy density to the underlying substrate (defined by polar and Van der Waals forces) begin to pull away from the surface and coalesce into oblate spheroid droplets to minimize the contact surface area-to-volume ratio. Surface undulation of the polymer film takes place over relatively longer time periods relative to liquid-solid interfaces as a function of film height ( $h$ ), thickness fluctuation ( $\delta h$ ), and the undulation growth rate ( $R$ ) given by [111]

$$Z(x, t) = h + \delta h e^{iqx} \quad \text{Eq. 4}$$

where  $\delta h = \delta h_0 e^{Rt}$ . Film instability arises at these growing undulations if the effective Hamaker constant ( $A$ , the measure of Van der Waals interactions of a number of bodies of two types in a unit volume) is negative. Direct observation of this phenomenon requires that the thickness fluctuation, undulation growth rate, and Hamaker constant be such that AFM can be performed on the intermediate steps (**Figure 2-5**).

#### 2.4.2 Conjugated Polymers

Conjugated polymers (CJPs) or, more specifically,  $\pi$ -conjugated polymers are a unique class of organic polymers defined by alternating carbon-carbon double bonds (i.e. -C-C=C-C-) in the polymer backbone [12, 13, 33, 34, 118, 119]. Potential conjugated polymer backbones include strictly linear backbones (e.g. polyacetylenes), ringed backbones (e.g. poly-phenylenes, poly-thiophenes, poly-pyrroles) and composite linear/ringed backbones (e.g. poly-phenylenevinylanes) (**Figure 2-6**). Most organic

## Common conjugated polymers

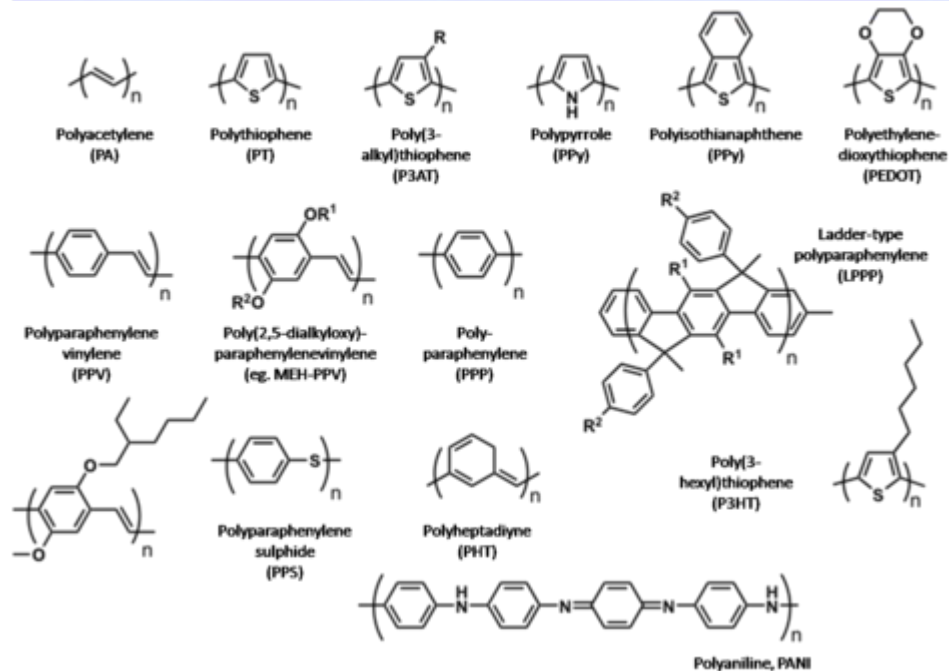


Figure 2-6 Common conjugated polymers (photonicswiki.org).

polymers consist of only  $\sigma$ -bonded carbons with strongly held s-orbital electrons or localized  $\pi$  electrons in some portion of a side group ligand. Conjugated polymers differ in that the conjugated  $\pi$  electrons are highly delocalized from their native positions on the molecule, meaning electrons can potentially diffuse across the entire length of the molecule or between multiple molecules if sufficient  $\pi$ - $\pi$  overlap exists. Delocalization across the polymer system produces a higher density of electronic states, extending the valence and conduction bands and lowering the overall energy gap between them [33]. Through appropriate tuning of the molecular structure and conjugation length, polymers of specific absorbance spectra can be generated.

#### 2.4.3 Fluorescence-based Sensing with Conjugated Polymers

Fluorescent conjugated polymers have begun to replace traditional organic fluorophores as signal generators for chemosensors over the last decade as their structure provides a largely delocalized  $\pi^*$  electron state, which allows single analyte binding events to result in multiple fluorescence quenching events [6, 11-13, 17, 18, 119]. Their unique molecular structure produces delocalized  $\pi^*$  electron states that permit significantly longer exciton and excited electron travel or ‘diffusion’ distances than traditional organic molecules, resulting in widespread, dynamic changes in fluorescence in the presence of target analytes [118, 120]. In particular, the conjugated polymer poly-[2-methoxy-5-(2-ethylhexyloxy)-p-phenylenevinylene] (MEH-PPV) has been shown to display a rapid quenching response in the presence of nitroaromatics due to its advantageous optoelectronic properties and electron-rich alkoxy side groups, which provide a conduit for excited state electron diffusion and transfer to the electron-deficient nitroaromatics [6, 11, 13, 15, 17, 100].

Fluorescent conjugated polymers (CJPs) have recently arisen as powerful signal transducers for solution- and vapor-phase chemical and biological sensors due to their advantageous electrochemical properties and flexible chemical composition [119]. One prominent example in recent years has been the detection of NA compounds (e.g. TNT and RDX) [13, 15, 26, 119, 121]. CJPs such as poly-[2-methoxy-5-(2-ethylhexyloxy)-p-phenylenevinylene] (MEH-PPV), display distinctly higher sensitivity over the one-for-one quenching response of traditional organic fluorophores as a result of the band gap of MEH-PPV overlapping with the lowest unoccupied molecular orbital (LUMO) of several NA

compounds and the electron-rich alkoxy side groups of MEH-PPV, which provide a conduit through which the excited state electron can travel to the NA molecule.

Unfortunately, MEH-PPV and other conjugated polymers degrade rapidly in the presence of oxygen and moisture through the oxidation of the vinylene groups to carbonyls, a problem exacerbated by exposure to light [122-125]. Several methods have been used to try to stabilize conjugated polymer films, including copolymerization with oxygen-resistant sub-groups, co-deposition with oxygen scavengers, and sealing under inert conditions [33, 126]. Yet while these methods avoid oxidation problems for organic light emitting diodes, solar cells, and other related applications, these arrangements are not conducive to sensing applications where the polymer should be exposed to the analyte of interest. Meanwhile, our lab has worked for several years on the development of thin oxide films (silica, alumina, etc.). Some of the thinnest films can be microporous as indicated by refractive index. Thus, we proposed the development of a microporous oxide thin film as a semi-permeable passivation layer over the conjugated polymer film, which may offer protection from photo-oxidation while allowing molecular diffusion to a degree that quenching may still occur.

Unfortunately, instability of the alternating vinylene bonds in the presence of oxygen and moisture has so far limited the application of conjugated polymers such as MEH-PPV to long-term, deployable sensors in real-world conditions [123-125, 127]. Copolymerization with oxygen-resistant sub-groups, co-deposition with oxygen scavengers, and sealing under inert conditions adequately avoid the problem of oxidation [33, 126, 128, 129], but such arrangements are not conducive to direct sensing applications

and suffer from much slower response times than unmodified thin films due to structural changes that adversely affect the polymer's optoelectronic properties [26]. Identifying an unobstructive passivation process to exclude environmental sources of oxygen while simultaneously retaining interactivity with analytes of interest is of critical importance to realizing a stable, portable fluorescent conjugated polymer sensor.

# **CHAPTER 3 PLASMONIC-ENHANCED CONJUGATED POLYMER FLUORESCENCE CHEMOSENSOR FOR TRACE NITROAROMATIC VAPOR DETECTION**

## **3.1 Introduction**

Trace vapor-phase detection of nitroaromatic (NA) explosive compounds and their decomposition products is a central focus of sensor development for many defense applications including public venue security, detection of unexploded ordinance (UXO) and improvised explosive devices (IEDs), and remediation of environmental contamination [11, 13, 15-17]. Sensing NA compounds centers around their partial electron deficiency stemming from the destabilizing effect of the electron withdrawing nitro groups spaced around the aromatic ring [8, 16, 89, 90]. It is this property that allows 2,4,6-trinitrotoluene (TNT) and dinitrotoluene (2,6-DNT and 2,4-DNT) to form observable, colored charge transfer complexes with electron donors under certain conditions (e.g. Meisenheimer complex with organic amines) and absorb photoelectrons through non-radiative energy transfer [8, 16, 89, 90]. However, conventional approaches applying optical transducers to vapor-phase detection of NAs have experienced a number of significant issues forestalling the development of long-term field-deployable sensors: sensitivity with low-power optics, selectivity over interfering analytes, and robustness under harsh environmental conditions [8, 14, 89, 90, 92]. Traditional organic dyes such as Fluorescein and Rhodamine derivatives are rapidly and efficiently quenched by NA as single molecules, but have a

tendency to exhibit poor signal-to-noise ratio (SNR) in practical vapor sensor setups, a combined effect of the low atmospheric vapor pressure of target NAs at typical temperatures encountered in the field, the one-for-one quenching response of these fluorophores to NAs, and the percent intensity change caused by a single affected fluorophore relative to the remnant unaffected bulk fluorescence [92, 100]. In order for typical trace concentrations encountered in real-world exposure events to have a meaningful (i.e. statistically significant) impact on fluorescence intensity, the number of fluorophores must be extremely small, which results in low SNR.

More recently, fluorescent conjugated polymers, originally developed for organic light-emitting diodes (OLEDs), have begun to replace traditional organic fluorophores as signal generators in NA sensing applications [6, 11-13, 17, 18]. Conjugated polymers are unique molecular structures with alternating  $\pi$ -bonded carbon (C=C) atoms, which provide highly delocalized  $\pi^*$  electron states that allow excited state electron diffusion distances in the range of 10-20 nm [130], far longer than the few angstroms afforded by typical organic fluorophores [11, 18]. This excited state electron diffusion can be visualized in the form of a widespread, reversible fluorescence quenching response to single analyte binding events. In particular, poly-[2-methoxy-5-(2-ethylhexyloxy)-*p*-phenylenevinylene] (MEH-PPV), has shown the most rapid quenching response in the presence of NAs compared to similar conjugated polymers such as poly(2,3-diphenyl-5-*n*-decyl-*p*-phenylenevinylene) (DP10-PPV) and poly[1-(*p*-*n*-butylphenyl)-2-phenylacetylene] (BuPA) due to its band gap overlapping with the lowest unoccupied molecular orbital (LUMO) levels of TNT and DNT, extended excited state electron diffusion distance from its more planar backbone,

and the more polar, electron-rich alkoxy side groups, which are believed to provide a conduit for excited state electron transfer to the electron-deficient NAs unavailable in the non-polar DP10-PPV and BuPA [6, 13].

Unfortunately, while MEH-PPV and other conjugated polymers show great promise as ultra-sensitive chemical sensors in the laboratory setting, a number of problems prevent their immediate application to portable, long-term deployable sensors. Most importantly, the alternating vinylene bonds are susceptible to rapid degradation in the presence of oxygen and moisture in open, ambient air through C=C oxidation to carbonyls or alcohols, respectively, a problem exacerbated by exposure to light [122-125, 127]. As such, exposing conjugated polymer thin films leads to severely reduced fluorescence within seconds of exposure to excitation light. Several methods have been used to attempt to stabilize conjugated polymer films, including copolymerization with oxygen-resistant sub-groups, co-deposition with oxygen scavengers, and sealing under inert conditions [33, 126, 128]. While these methods adequately mitigate the problem of photo-oxidation for OLEDs, dye-sensitized solar cells, and other related applications, such arrangements are not conducive to sensing applications where the polymer should be exposed to the analyte of interest and the sensitivity is reduced. Prior attempts to use these methods suffered from response times several orders of magnitude slower than unmodified thin films due to complete passivation or changes in the structure that adversely affect the conjugation length or optoelectronic properties [26]. Thus, identifying methods to exclude environmental sources of oxygen while simultaneously retaining rapid, measurable interactivity with analytes of interest is of critical importance to realizing a stable, portable

fluorescent conjugated polymer chemosensor. A semi-permeable membrane capable of screening out harmful moieties while simultaneously allowing selective access to the polymer by the analyte of interest would be ideal. In this work, we explore the use of an ultra-thin oxide thin film as a semi-permeable passivation layer over the MEH-PPV film, which may offer protection from photo-oxidation while allowing molecular diffusion to a degree that rapid quenching may still occur.

SNR, optoelectronic properties, and photostability can be further tuned and potentially improved by engineering the underlying substrate to provide intrinsic signal amplification, which can expand sensor dynamic range and lower the limit of detection without necessitating noise-enhancing signal post-processing. Fluorescence-based sensors can be further improved by engineering the underlying substrate to provide intrinsic signal amplification through enhancement of excitation and radiative decay rates (i.e. metal-enhanced fluorescence, MEF) [53, 55, 131] and energy transfer properties [56-58]. Chief among the mechanisms of MEF are localized and propagating surface plasmon resonance (SPR) effects occurring at the interface between a plasmonic active metal (e.g. silver, gold) and a fluorescently labeled dielectric layer [5, 59, 64, 66, 67]. The exact modes of enhancement are determined by the nanoscale structure of the metal layer. Continuous, nanoscale periodic metallic gratings enable free space coupling of the incident photons to surface plasmons, making them keenly appropriate platforms for optical sensors [60-63]. While a number of groups have reported MEF of FCPs using nanostructured metal surfaces, the focus has remained in large part on their use for semiconductor lasers [132-135]. In the present work, we present a stable, plasmonic-enhanced quenching-based

fluorescence sensor to detect NA using MEH-PPV coated over a silver grating surface. These gratings have been produced by a recently developed low-cost micro-contact printing process that takes advantage of the periodic structure of HD-DVDs as a template, replacing prohibitively expensive construction methods such as electron beam lithography [65]. Furthermore, we investigate the addition of an ultra-thin oxide film as a passivation layer to mitigate photo-oxidation. These substrates are evaluated against equivalent films on SiO<sub>2</sub>-coated silicon in terms of their stability during use and extended storage in ambient conditions as well as time-sensitive response to model NA 2,4-DNT.

### **3.2 Experimental Section**

#### **3.2.1 Chemicals and Materials**

Standard glass microscope slides were purchased from Fisher Scientific (Pittsburgh, PA) and silicon wafers from MEMC (St. Peters, MO). Polydimethylsiloxane (PDMS, Sylgard® 184, Dow Corning, Inc.), poly-[2-methoxy-5-(2-ethylhexyloxy)-p-phenylenevinylene] (MEH-PPV, M<sub>n</sub> 40,000-70,000), 2,4-Dinitrotoluene (2,4-DNT), 1,3-Dinitrobenzene (1,3-DNB), Nitrobenzene (NB), hydrofluoric acid (HF), ammonium fluoride (NH<sub>4</sub>F), and all organic solvents were purchased from Sigma-Aldrich (St. Louis, MO) and polymethylsilsesquioxane (PMSSQ, GR650F) from Techneglas (Perrysburg, OH).

#### **3.2.2 Substrate Preparation**

Silver plasmonic gratings were made by an in-house developed micro-contact printing process described previously [65]. Briefly, silicone elastomer (Sylgard® 184) was mixed in a 5:1 ratio of base to crosslinker, then poured and cured over an isopropanol-

cleaned HD-DVD to generate a master mold. Cured silicone was then cut into 1 cm × 1 cm stamps and used to print the polymer ink, 3% (w/w) PMSSQ dispersed in ethanol, onto freshly-cleaned silicon. The silicone stamp was peeled off after a few seconds and the polymer ink allowed to dry in ambient laboratory conditions. The PMSSQ gratings were then transferred to an AJA RF Magnetron sputter system and a 2 nm titanium adhesion layer was deposited followed by 100 nm silver using 100 W RF power, 20 sccm argon flow, and 4 mTorr working pressure. Samples were then stored in a nitrogen-purged glove box prior to further use.

For comparison of quenching activity, and evaluation of enhancement factor samples were prepared on silicon with varying thicknesses of thermally grown silicon oxide ( $\text{SiO}_2$ ) since silicon is known to quench fluorescence within short distances and optical interference occurs at thicknesses greater than ~100 nm [72, 136]. Before oxide growth, each 5 cm × 5 cm silicon wafer piece was cleaned by sonication in successive baths of acetone, methanol, and deionized water (18.2 MΩ-cm) and then dipped in 1:10 HF:H<sub>2</sub>O for 1 minute to remove the native oxide layer and hydrogen passivate the surface. Dry thermal  $\text{SiO}_2$  was grown at 1100 °C by flowing 5 cfm oxygen in a quartz tube furnace for 30 minutes and etched to different thicknesses by 1:15 HF:NH<sub>4</sub>F buffered oxide etching solution for 0-300 s [137, 138]. Etched  $\text{SiO}_2$  thicknesses were verified by variable angle spectroscopic ellipsometry (VASE, J.A. Woollam, Inc.) using the Cauchy model to estimate optical constants.

Immediately prior to spin-casting MEH-PPV, all substrates were cleaned thoroughly with acetone, methanol, and 2-isopropanol, blown dry with nitrogen, and

transferred to the glove box. MEH-PPV was dispersed in chloroform to 0.5, 2, or 4 mg/mL (0.05, 0.2, or 0.4% w/v) and spin-cast at 3000 rpm for 30 seconds and stored in vacuum overnight to ensure removal of excess solvent. Some of these substrates were then transferred to a Kurt J. Lesker electron beam physical vapor deposition (PVD) chamber and capped with 5 nm SiO<sub>2</sub> (deposition rate tuned to 0.05 Å/s). All substrates were then stored in the glove box until measurement.

### 3.2.3 Substrate Characterization

Thickness and optical properties of the thermal oxide spacer layer, MEH-PPV layer, and PVD oxide capping layer were characterized by variable angle spectroscopic ellipsometer (VASE, J.A. Woollam, Inc.). Due to the extremely high and broad optical absorbance of MEH-PPV, spectroscopic ellipsometry and transmission measurements were performed first on glass to verify thickness and optical constants. A separate silicon substrate dipped in 1:10 HF:H<sub>2</sub>O was used to characterize the capping layer thickness. AFM images of the substrate surfaces were collected on an Agilent 5500 microscope in tapping mode. Grating reflectance measurements for each MEH-PPV condition were acquired by ellipsometer by orienting the gratings vertically and using p-polarized light. Angles were varied from the instrument minimum at 15° up to 40° and wavelength from 470 – 650 nm.

### 3.2.4 Intensity, Bleaching, and Long-term Stability

Fluorescence spectra and images were acquired on an Olympus BX51W1 epi-fluorescence microscope using a 300 W Xenon lamp using the Semrock FITC-LP01 Filter (Excitation: 475 nm ± 15 nm band pass / Emission: 516 nm long pass) or R6G Filter

(Excitation: 520 nm  $\pm$  10 nm band pass / Emission: 542 nm long pass) and appropriate combination of focal stop and 25% and 6% neutral density filters to reduce areal illumination, bleaching, and photodetector saturation (actual illumination  $\sim$ 2 mW/cm<sup>2</sup>). Spectra were acquired using an Ocean Optics USB-4000 spectrometer and analyzed for peak position and absolute and relative intensities by PeakFit v4.12 (Systat Software, Inc.). Images were also taken using a Hamamatsu ORCA-Flash 2.8 CMOS camera with integration times: 20, 40, 60, 80, and 100 ms and 200 $\times$  *equivalent* gain and were analyzed by ImageJ particle analysis tool to correlate enhancement due specifically to the nanogap regions [139]. Bleaching studies were carried out by measuring spectra under continuous illumination for up to one minute. Some substrates were also stored wrapped in foil and kept in ambient environmental conditions for up to two months. Fluorescence measurements were taken periodically and compared to the initial values.

### 3.2.5 Response to Dinitrotoluene and other Nitro-containing Compounds

MEH-PPV sensor response to 2,4-DNT was evaluated using the BX51W1 microscope in ambient conditions in a manner similar to Östmark *et al.* [100]. Briefly, a 20 mL glass vial was filled with  $\sim$ 2 g dry 2,4-DNT powder and covered by several layers of cotton gauze to prevent direct physical contact [11, 13]. Samples were placed into the container face-up on the cotton and capped for a specified period of time (10-1200 s) to expose them to saturated 2,4-DNT vapor ( $\sim$ 300 ppb). The samples were removed from the vial and measured immediately (1-2 seconds) to prevent recovery by diffusion out of the film. Care was also taken to limit exposure to light in order to reduce photobleaching

effects. Fluorescence recovery after removal from the vapor source was also monitored for several hours after the experiment.

### 3.3 Results and Discussion

#### 3.3.1 MEH-PPV Film Morphology

Schematics of the capped ultra-thin MEH-PPV films on plasmonic gratings and SiO<sub>2</sub>-coated silicon substrates are given in **Figure 3-1A,B** and corresponding AFM images in **Figure 3-1C-K**. MEH-PPV film thickness on SiO<sub>2</sub>-coated silicon was found by ellipsometer to be 6.5 nm, 13 nm, and 30 nm for 0.05%, 0.2%, and 0.4% (w/v) solutions, respectively. These were confirmed independently by an AFM scratch test on the 13 nm film as well as by performing spectroscopic ellipsometry and transmission measurements on uncapped MEH-PPV thin films spin-cast on glass as reliable modeling of thickness and refractive index is difficult for extremely thin and highly absorbing films [140, 141].

AFM imaging revealed a complex, undulating MEH-PPV thin film morphology caused by the onset of surface energy-mediated spinodal dewetting from the pristine SiO<sub>2</sub> surface (**Figure 3-1C,F,I**) [111]. Spinodal dewetting is a thin film phenomenon related to spinodal decomposition [116, 117] (e.g. phase separation) of mixtures of two immiscible or only conditionally miscible liquids (e.g. oil and water). The term ‘spinodal’ refers to a set of critical temperatures and relative pressures bounding the regions where metastable mixtures can exist. Outside of the spinodal, phase separation is inevitable. Such separation can occur with liquid-liquid mixtures as well as at interfaces of solids/liquids/gases with a solid substrate. In the thin film case, materials with high contrast in surface energy density to the underlying substrate (defined by polar and Van der Waals forces) begin to pull away

from the surface and coalesce into spheroid droplets to minimize the contact surface area-to-volume ratio. In the case of liquid-solid interfaces, droplet formation is virtually

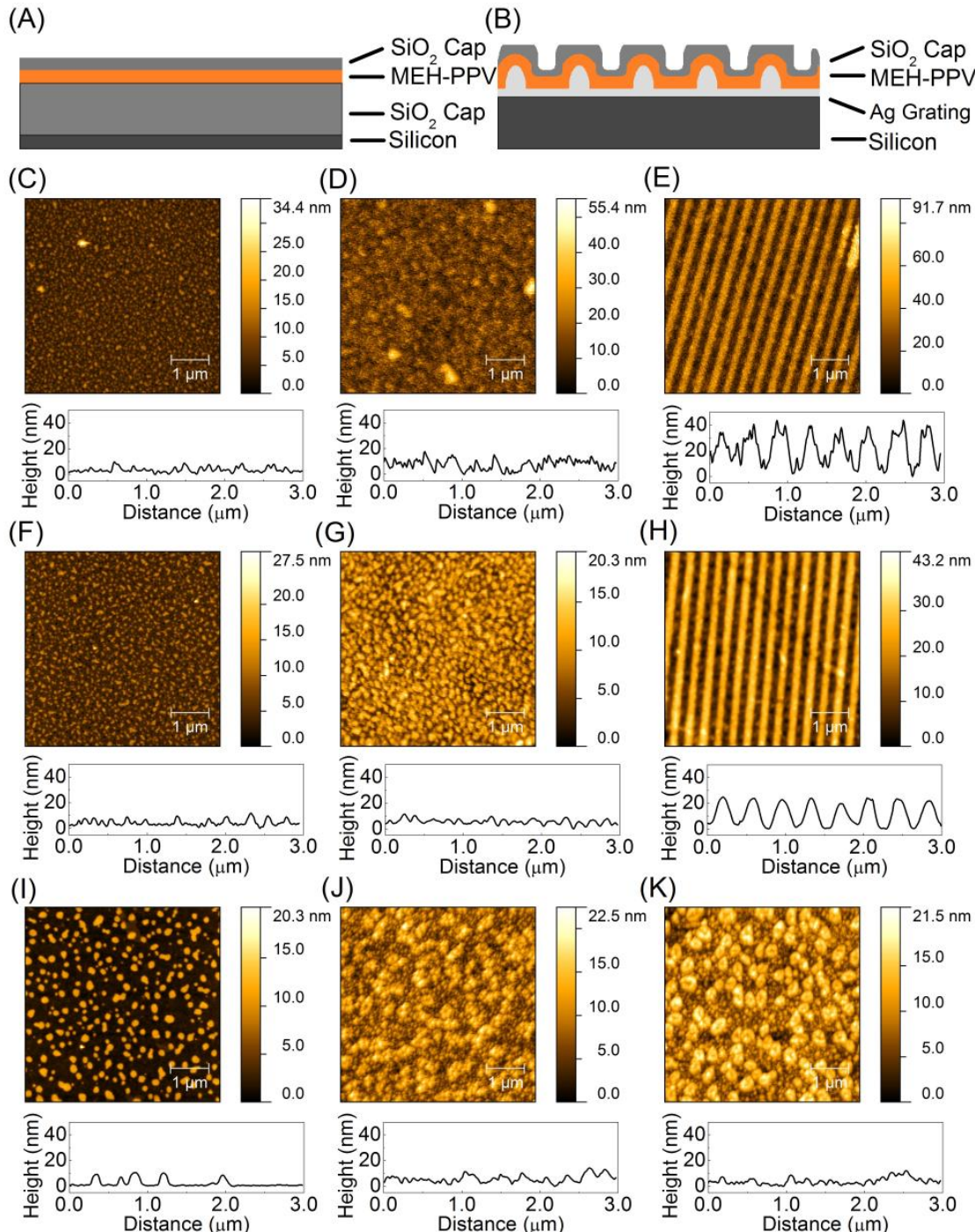


**Figure 3-1 (A,B)** Schematic of capped plasmonic-enhanced fluorescence-based chemosensor; **(C-K)** AFM images and height profile of the oxide-capped MEH-PPV thin films of various thicknesses on **(C,F,I)** SiO<sub>2</sub>-coated silicon, **(D,G,J)** flat silver, and **(E,H,K)** plasmonic silver gratings, respectively.

instantaneous (as in contact angle measurement) due to the motility of the material in liquid form. Meanwhile, for solid film-solid interfaces, surface undulation takes place over relatively longer time periods as a function of film height ( $h$ ), thickness fluctuation ( $\delta h$ ), and the undulation growth rate ( $R$ ) (see section 2.4.2) [111]. Film instability arises at these growing undulations if the effective Hamaker constant ( $A$ , the measure of Van der Waals interactions of a number of bodies of two types in a unit volume) is negative. Direct observation of this phenomenon requires that the thickness fluctuation, undulation growth rate, and Hamaker constant be such that AFM can be performed on the intermediate steps. While these steps were not able to be observed on MEH-PPV films on silica, the final result matches the characteristics of spinodal dewetting sufficiently to conclude it as such. The primary reason for MEH-PPV dewetting is due to a mismatch of surface energy density between the MEH-PPV ( $\gamma \approx 26 \text{ mJ/m}^2$  as measured on ITO) [142] and the freshly cleaned  $\text{SiO}_2$  surface ( $\gamma \approx 71\text{-}77 \text{ mJ/m}^2$ ) [113]. Significant improvements to polymer dissolution techniques were undertaken to reduce dewetting as much as possible, but some were unavoidable due to the use of chloroform as the solvent. Toluene, p-xylene, and other aromatic solvents may be used to alleviate some of the chemical pressures associated with particulate formation in a relatively poor solvent such as chloroform, but may lead to more orderly alignment through increased  $\pi\text{-}\pi$  interaction, which reduces the fluorescence efficiency of the material [143, 144]. Furthermore, “better” (i.e. more non-polar, aromatic) solvents would not address the underlying surface energy mismatch between MEH-PPV and  $\text{SiO}_2$ . Utilizing a non-polar self-assembled monolayer (SAM) such as octodecyltrichlorosilane (OTS) ( $\gamma \approx 20\text{-}25 \text{ mJ/m}^2$  [113]) may improve surface energy

matching on  $\text{SiO}_2$ , but more care would need to be taken with regards to silver, especially given that increased distance from the surface as well as degradation and oxidation by silane and solvents reduce plasmonic coupling efficiency. Furthermore, it was noted that capping the films appears to halt or significantly retard the dewetting process as capped films were stable for months. As such, the overall process was not modified to include OTS treatment.

Film thickness and surface roughness ( $R_a$ ) on  $\text{SiO}_2$ -coated silicon measured by AFM were in fairly good agreement with ellipsometer measurements: 8 nm (1.82 nm), 15 nm (1.82 nm), and 20 nm (2.51 nm) for 0.05%, 0.2%, and 0.4%, respectively. MEH-PPV on flat silver (**Figure 3-1D,G,J**) had similar apparent thickness and roughness: 7 nm (3.75 nm), 12 nm (2.1 nm), and 22 nm (2.56 nm). The larger increase in  $R_a$  for the thinnest film on both flat silver and the gratings is due to contributions from the underlying silver grains (**Figure 3-1D,E**). MEH-PPV spun on the metallic gratings planarized the grating grooves with apparent height reduction compared to the uncoated grating height (60 nm) of ~20 nm for 0.05% and ~35 nm for 0.2% while the 0.4% concentration completely planarized the grating structure and shows densely packed grains (**Figure 3-1E,H,K**) [65]. This perturbation of the periodic structure can have deleterious effects on the plasmonic coupling of the incident excitation energy as will be shown in the next section. Thickness and surface roughness data are summarized in **Table 3-1** and **Table 3-2**.

Capping MEH-PPV with a thin film by electron beam evaporation is an inherently delicate process as the technique introduces energized material capable of oxidizing the polymer. Ultra-thin films (<50 nm) of MEH-PPV have extremely low tolerance of ambient

**Table 3-1 Concentration-dependent MEH-PPV Thickness on SiO<sub>2</sub>**

[MEH-PPV]	<i>d</i> (nm)	Std Err	RI	Std Err
0.05%	6.77	0.44	1.653	0.027
0.1%	10.07	0.29	1.665	0.055
0.2%	12.68	0.11	1.676	0.004
0.3%	19.83	0.80	1.686	0.0115
0.4%	29.17	0.25	1.721	0.007

**Table 3-2 Sample Surface Roughness, R<sub>a</sub> ± SD (nm)**

Sample	Native	0.05%	0.05%	0.05%
SiO <sub>2</sub>	0.28 ± 0.03	1.82 ± 0.05	1.82 ± 0.01	2.51 ± 0.03
Ag Flat	5.93 ± 0.65 <sup>@</sup>	3.75 ± 0.1	2.1 ± 0.06	2.56 ± 0.06
Ag Grating (peak)	5.07 ± 0.45 <sup>@</sup>	3.44 ± 0.13	1.73 ± 0.06	3.01 ± 0.07*
Ag Grating (valley)	6.4 ± 1.04 <sup>@</sup>	3.8 ± 0.21	1.79 ± 0.18	3.01 ± 0.07*

\*Grating structure no longer visible, indicating complete filling.

<sup>@</sup>Silver substrates were ~1 yr old at measurement and showed signs of possible degradation.

atmosphere or oxidizing conditions, resulting in rapid photobleaching [145]. Care was taken to perform PVD oxide deposition in the absence of excess oxygen flow or post-run high-temperature annealing to prevent complete oxidation of the underlying MEH-PPV film. Optical properties of the PVD silicon oxide capping layer were measured on a hydrogen-passivated silicon substrate. Oxide thickness was found by spectroscopic ellipsometry to be 5 nm and AFM measurement revealed very low intrinsic surface roughness (R<sub>a</sub> = 0.28 ± 0.03 nm). Film density is also critically important as it represents the layer discontinuity or porosity through which analytes may diffuse into the polymer beneath. However, it is simultaneously important to limit diffusion pathways for oxygen and moisture so a delicate balance between porosity and protective layer attributes must be maintained. The measured PVD oxide refractive index at 630 nm (n = 1.38) confirms a lower density than bulk SiO<sub>2</sub> (n = 1.46), as expected when curbing deposition during the initial stages of thin film growth. The void fraction or ‘air’ space comprising pores of the

PVD oxide was evaluated by the Bruggeman model for effective medium approximation [146], which defines the void fraction  $f$  as

$$f \frac{\varepsilon_v - \varepsilon_{eff}}{\varepsilon_v + 2\varepsilon_{eff}} + (1 - f) \frac{\varepsilon_s - \varepsilon_{eff}}{\varepsilon_s + 2\varepsilon_{eff}} = 0 \quad (\text{Eq. 4})$$

in terms of the solid, void, and effective dielectric constants  $\varepsilon_s$ ,  $\varepsilon_v$ , and  $\varepsilon_{eff}$ , respectively. This is an electrically-defined approximation assuming the materials are simple dielectrics over the defined range (e.g. SiO<sub>2</sub>, PMSSQ, Al<sub>2</sub>O<sub>3</sub>, water, air, etc.) and assuming the total effect of the film on the mean electric field is zero. Since the imaginary extinction coefficient  $k$  of the dielectric constant [ $\varepsilon = (n + ik)^2$ ] of simple dielectrics is negligible in their range of dielectric effect, the dielectric constant of the PVD oxide and constituents can be approximated as  $\varepsilon \approx n^2$  and, thus, the equation becomes a function of the refractive indices of air, SiO<sub>2</sub>, and the overall film. Solving for the void volume fraction (i.e. film porosity):

$$\frac{f}{f-1} = \frac{\left(\frac{\varepsilon_s - \varepsilon_{eff}}{\varepsilon_s + 2\varepsilon_{eff}}\right)}{\left(\frac{\varepsilon_v - \varepsilon_{eff}}{\varepsilon_v + 2\varepsilon_{eff}}\right)} = C \quad (\text{Eq. 5})$$

$$f = \frac{C}{C-1} \quad (\text{Eq. 6})$$

Defining  $\varepsilon_s \approx (1.46)^2$  (i.e. SiO<sub>2</sub>),  $\varepsilon_v \approx (1.003)^2$  (i.e. air), and  $\varepsilon_{eff} \approx (1.38)^2$ , the void fraction was found to be  $f \approx 0.17$ , which is sufficient to suggest sparsely distributed and disconnected (closed) pores. Thus, this ultra-thin oxide layer represents a good candidate for a capping layer and was studied for its effects on sensor performance.

### 3.3.2 Photophysical Characterization

**Figure 3-2A-D** shows the reflectance spectra for each of the capped MEH-PPV-coated grating samples with increasing film thickness with respect to plain, unmodified silver gratings. Multiple dips and features are visible in each angle scan, corresponding to the intrinsic, angle-independent silver inter-band absorption peak (~320 nm), characteristic polymer absorption (optical band gap 2.1 eV corresponding to 590 nm), and pairs of sharp dips in reflectance at wavelengths corresponding to the lower and upper grating-coupled modes for a particular angle ( $m = \pm 1$ ). As mentioned above in Section 3.1, the grating-coupled modes are given by the dispersion relation

$$k_{sp} = k_o \sqrt{\frac{\varepsilon_m \varepsilon_d}{\varepsilon_m + \varepsilon_d}} = n_d k_o \sin \theta_{SPR} \pm \frac{2\pi m}{\Lambda} \quad (\text{Eq. 3})$$

where  $k_{sp}$  is the wavevector of the intrinsic surface plasmons,  $k_o$  is the wavevector of the incident light,  $\varepsilon_m$  is the dielectric constant of the metal,  $\varepsilon_d$  is the dielectric constant of the dielectric,  $n_d$  is the refractive index of the dielectric,  $m$  is the order of the grating mode, and  $\Lambda$  is the grating pitch [65]. The grating coupled modes at 15° for the gratings with silver-air interface (**Figure 3-2A**) are located at 387 nm and 532 nm. From the above equation, we expect and observe a red shift in the grating-coupled wavelengths on increasing polymer thickness as the dielectric interfacing with the gratings changes from that of air (~1) to MEH-PPV (~1.8) (**Table 3-3**) [141]. From **Table 3-3**, we also see that the quality factors of the dips  $Q$  increases slightly with increasing thickness while  $\gamma$  decreases for plain Ag gratings and the 6.5 nm equivalent film on gratings while increasing for 13 nm and 30 nm equivalent films on gratings. These quality factors are defined by  $Q = \lambda / \Delta \lambda$  and  $\gamma = \sigma / \Delta \lambda$ , respectively, where  $\lambda$  is the central wavelength of the dip,  $\Delta\lambda$  is the full-width half

maximum of the dip, and  $\sigma$  is the dip coupling strength (i.e. height) measured at the central wavelength. The  $\gamma$  factor is considered a stronger measure of coupling quality as it incorporates the coupling strength ( $\sigma$ ) directly and  $Q$  has a tendency to increase with

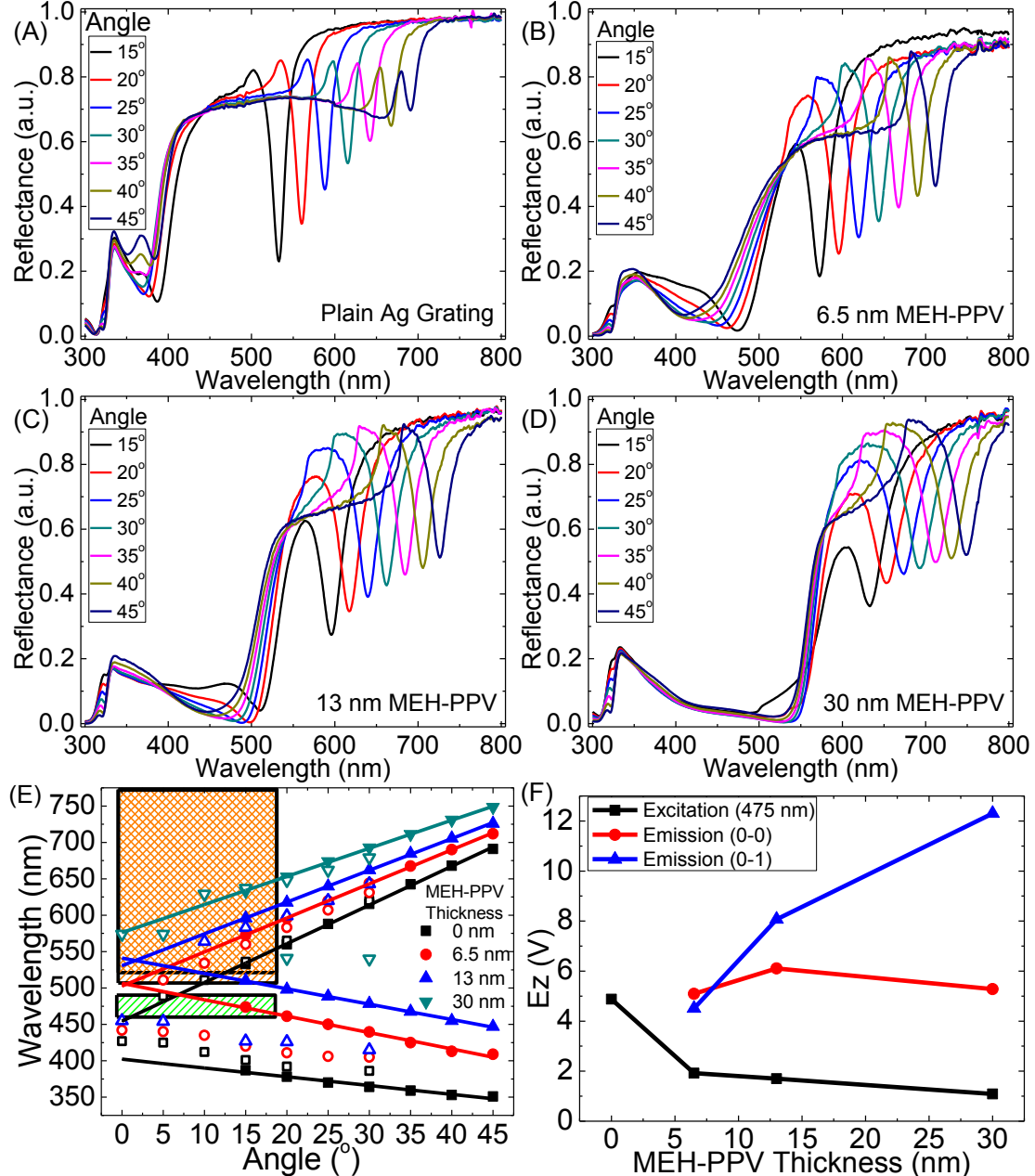


**Figure 3-2 (A-D)** Reflectance curves for capped MEH-PPV thin films on silver plasmonic gratings with respect to unmodified silver plasmonic gratings; (E) Theoretical (open) and experimental (solid) coupling maxima with experimental dispersion curves comparing capped MEH-PPV-coated silver gratings with unmodified silver gratings; (F) FDTD simulated maximum electric field components coupled at 15° for each MEH-PPV film thickness.

increasing  $\lambda$  independent of the coupling strength due to the increase in numerator. At any rate, the  $\gamma$  factors switches between higher quality at lower angles for thinner films and higher quality at higher angles for thicker films. While these trends correlate well with the

**Table 3-3 Summary of Grating Reflectance Dip Locations and Associated Quality Factors.**

<i>Ag</i>	$\lambda_c$	$\sigma$	$\Delta\lambda$	Q	$\gamma \times 100$
15	532	0.652	18	29.6	3.62
20	560	0.646	15	37.3	4.31
25	588	0.448	17.25	34.1	2.60
30	615.5	0.364	16.5	37.3	2.20
35	642	0.302	16.5	38.9	1.83
40	668	0.243	16	41.8	1.52
45	691	0.197	15.5	44.6	1.27
<hr/>					
0.05%	$\lambda_c$	$\sigma$	$\Delta\lambda$	Q	$\gamma \times 100$
15	572.5	0.534	25	22.9	2.14
20	595.5	0.541	25	23.8	2.16
25	619.5	0.525	24.75	25.0	2.12
30	643.5	0.500	23.5	27.4	2.13
35	667.5	0.474	22.5	29.7	2.11
40	690	0.440	21.35	32.3	2.06
45	712	0.419	21	33.9	2.00
<hr/>					
0.2%	$\lambda_c$	$\sigma$	$\Delta\lambda$	Q	$\gamma \times 100$
15	596	0.485	28.5	20.9	1.70
20	617.5	0.502	29.75	20.8	1.69
25	639.5	0.501	29.5	21.7	1.70
30	662	0.491	28.5	23.2	1.72
35	684.5	0.473	27	25.4	1.75
40	706	0.452	25.25	28.0	1.79
45	726	0.425	24.75	29.3	1.72
<hr/>					
0.4%	$\lambda_c$	$\sigma$	$\Delta\lambda$	Q	$\gamma \times 100$
15	633	0.363	40.75	15.5	0.89
20	652.5	0.388	38.25	17.1	1.01
25	674	0.416	37.5	18.0	1.11
30	692.5	0.429	37.75	18.3	1.14
35	711.5	0.428	36.5	19.5	1.17
40	731	0.428	34.5	21.2	1.24
45	748.5	0.423	32.6	23.0	1.30

red shift in coupling dip locations for thicker films, these may yet be an artifact of the overall slope of the blue edge of the reflectance curve caused in part by the high absorbance of the MEH-PPV, leading to a lower left-hand reflectance measurement point and, thus, lower coupling strength.

Extracting the dip location data across multiple angles allows generation of experimental dispersion curves for each of the four grating samples (**Figure 3-2E**, solid points). Wavelengths coupled at angles near normal incidence (i.e. those that lie within the  $\sim 17^\circ$  acceptance cone of a typical  $10\times$  objective lens) are of particular interest for sensing applications as their use would simplify constraints on optics and allow measurements to be performed using an upright microscope, microplate reader, or portable handheld unit. Extrapolation of the upper resonance mode dip locations provides the grating-coupled wavelengths at normal incidence for each film: 500 nm, 530 nm, and 570 nm for 6.5, 13, and 30 nm equivalent films on gratings, respectively. Meanwhile, the green

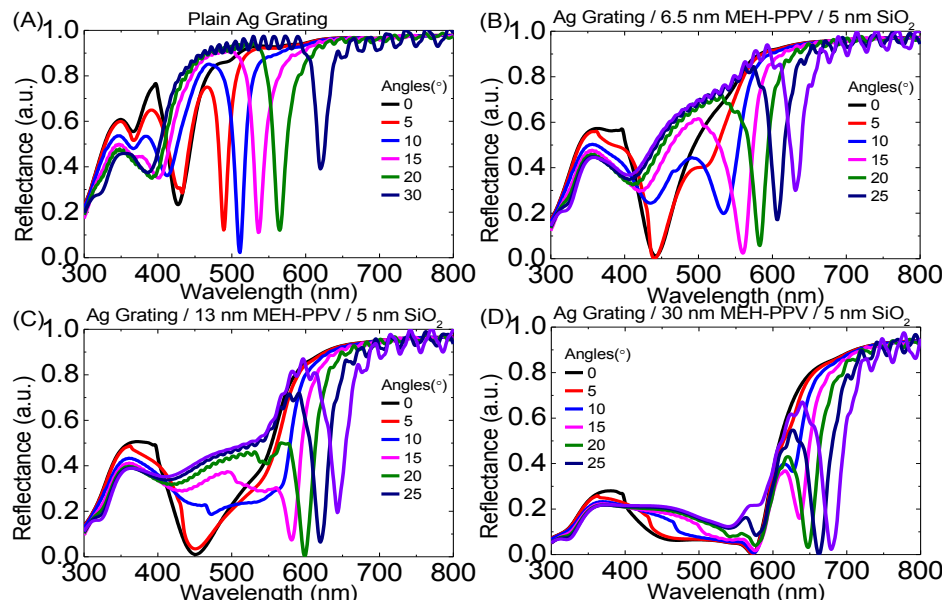


**Figure 3-3** FDTD simulations of reflectance of (A) unmodified silver plasmonic gratings and (B-D) gratings with increasing thickness of MEH-PPV thin films and 5 nm  $\text{SiO}_2$  capping layer.

hashed box in **Figure 3-2E** indicates the wavelengths used for excitation (460-490 nm) from the FITC filter. Examination of **Figure 3-2E** shows that these wavelengths are located in the lower mode regime for all samples, but are only coupled at low angles for the 6.5 nm sample, and are then only weakly coupled. Therefore, enhancement of MEH-PPV fluorescence by increased electromagnetic field resulting from coupling the incident excitation light is expected to be weak as compared to a hypothetical fluorophore with excitation in the upper resonance modes.

Further inspection of the upper resonance mode locations at angles less than 17° suggest that photons in the regime emitted by MEH-PPV may be optimally coupled to the gratings at near normal incidence. MEH-PPV produces a broad luminescence spectrum with three main peaks corresponding to vibronic transitions (0-0, 0-1, 0-2) within a single electronic state, which are located between 520-750 nm as indicated by the orange box with left hash marks [118, 147]. Finite-difference time-domain (FDTD) simulations of the gratings were performed using RSoft® to ascertain how the MEH-PPV film thickness affects coupling to the gratings (**Figure 3-3**) and the electric field enhancements in the excitation (**Figure 3-4**) and emission (**Figure 3-5**) regimes. The critical locations of the FDTD-defined theoretical reflectance dips from **Figure 3-3** were added as open points in **Figure 3-2E**. These simulations are relatively well-matched to the ellipsometry results with slight wavelength discrepancies as a result of the high MEH-PPV absorption and planarization of the gratings as seen in AFM. An important outcome of these simulations is that electric field concentration is 3-11× higher at the emission wavelengths (0-0 and 0-1 transitions) as compared to the excitation wavelength (**Figure 3-2F**), confirming strong

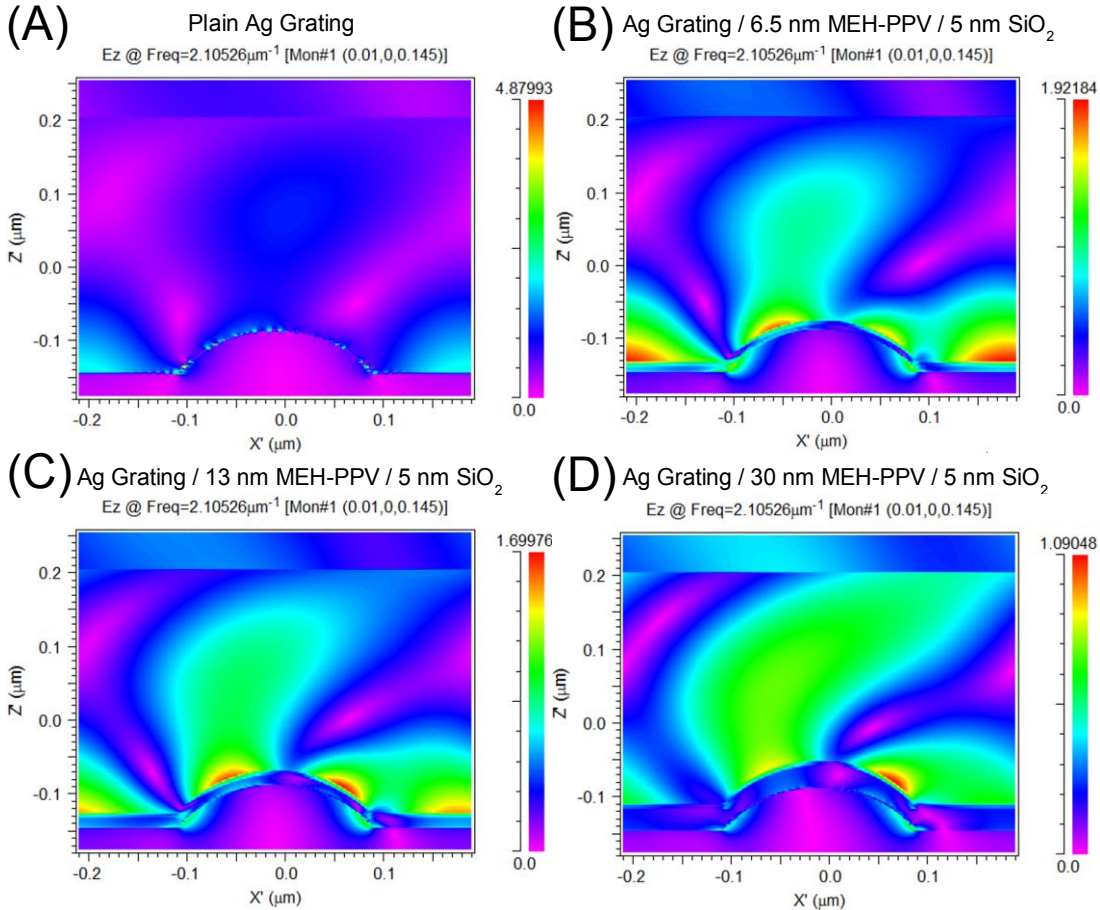


**Figure 3-4 Electromagnetic field results from FDTD simulations at 15° and the center of the excitation wavelength band used (475 nm).**

coupling in the upper mode region and the possibility for surface plasmon-coupled emission (SPCE) [131, 148]. The decrease in electric field with increasing MEH-PPV thickness in the excitation regime is ascribed to stronger photon absorption and lower mode mismatch. However, the emission wavelength (0-1 transition) matches the upper mode resonance of the 30 nm MEH-PPV film at lower incidence angles, resulting in better coupling and higher evanescent electric field with respect to the thinner films. Still, the thinnest film sample was chosen for further study as a sensor substrate due to its lower mode matching with the excitation filter wavelengths and also since the thicker films have

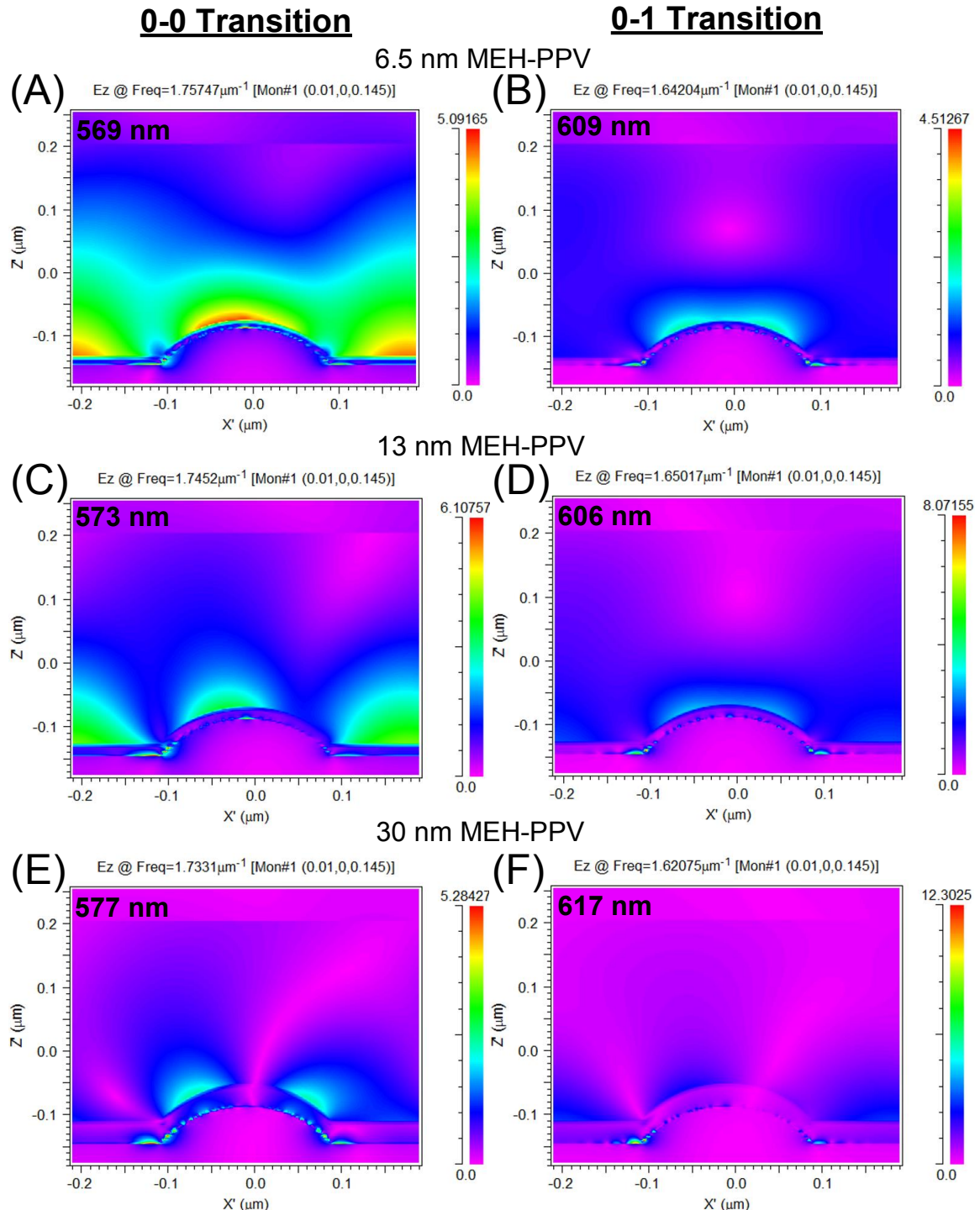


**Figure 3-5 Electromagnetic field results from FDTD simulations at 15° and the 0-0 and 0-1 emission wavelengths for each capped film.**

naturally slower response time to NA vapors [11], which would be exacerbated by the presence of the capping layer.

### 3.3.3 Optimization of SiO<sub>2</sub>-Coated Silicon

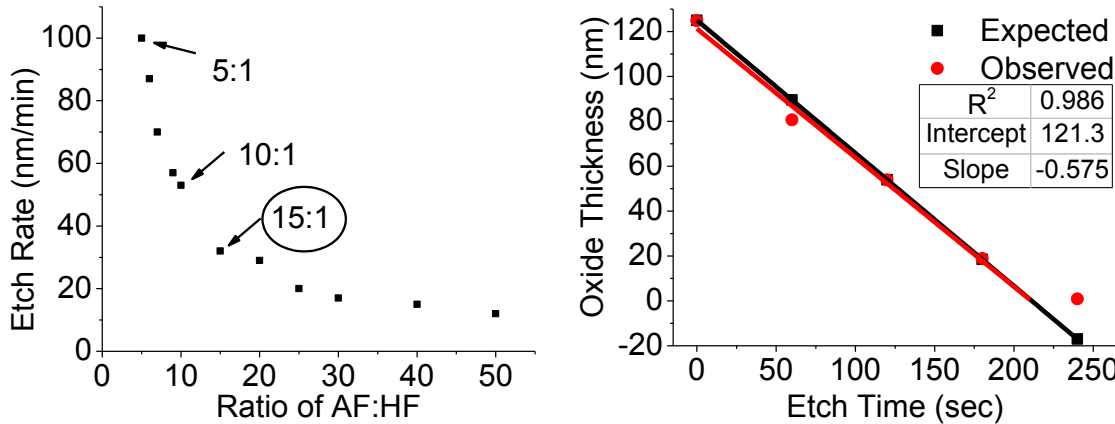


**Figure 3-6** (A) Tunable oxide etch rates by AF:HF mixtures as calculated by Honeywell [138] and (B) Expected and observed etched oxide thicknesses using a 15:1 AF:HF mixture and beginning with 124 nm oxide thickness.

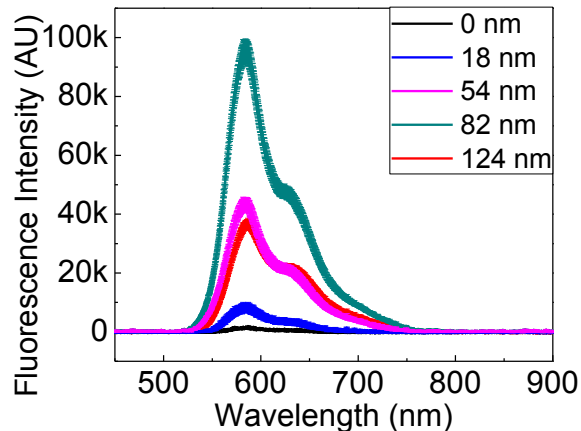


**Figure 3-7** Fluorescence spectra of uncapped 6.5 nm MEH-PPV thin films spun from 0.05% chloroform solution onto silicon oxide thin films of increasing thickness.

Thin fluorescent films on silicon are known to experience significant fluorescence quenching within a few nanometers of the silicon surface due to dipole-induced energy transfer as well as constructive and destructive interference effects for fluorophores atop

dielectric thin films (e.g. SiO<sub>2</sub>) thicker than 100 nm [72, 136]. To mitigate these effects, thermal oxide SiO<sub>2</sub> was grown onto polished, low-doped silicon and then etched by NH<sub>4</sub>F:HF buffered oxide etchant (BOE) at a rate of ~30 nm per minute using a BOE defined by the ratios in **Figure 3-6A** [138] and confirmed experimentally to provide different SiO<sub>2</sub> thicknesses between 0 and 124 nm (**Figure 3-6B**). Spin-casting 6.5 nm MEH-PPV thin films atop each substrate provided fluorescence intensities ranging from <2000 cps on 0 nm SiO<sub>2</sub>-coated silicon increasing to ~95,000 cps on 82 nm SiO<sub>2</sub>-coated silicon (**Figure 3-7**). The intensity then dropped by more than 50% on increasing SiO<sub>2</sub> thickness to 124 nm, a result of SiO<sub>2</sub> thickness entering the range of the first destructive interference fringe for back-reflected light defined by  $2nd\cos\theta = k\lambda/2$ , where  $k$  is even for constructive interference and odd for destructive interference [72]. Thus, the ~82 nm SiO<sub>2</sub> condition was reproduced on many SiO<sub>2</sub>-coated silicon substrate samples and used for all subsequent experiments.

### 3.3.4 Fluorescence Characterization

**Figure 3-9A** illustrates the fluorescence spectra of the thinnest MEH-PPV film set prepared on different SiO<sub>2</sub>-coated silicon, flat silver, and plasmonic silver grating substrates with respect to the 0.05% (w/v) chloroform solution. Detailed peak-fitting was carried out to identify the location of the 0-0, 0-1, and 0-2 vibronic emission peaks characteristic to MEH-PPV (**Figure 3-8**) and summarized for the thinnest film in **Table 3-4**. Generally, MEH-PPV thin films exhibit red-shifted fluorescence compared to their respective solution phase depending on the degree of conformational disorder and chain-chain interactions between molecules [118, 120, 147]. Primary (0-0 transition) peaks were

located at 555 nm, 582 nm, 576 nm, and 578 nm for the chloroform solution, and 6.5 nm films on SiO<sub>2</sub>-coated silicon, flat silver, and plasmonic gratings, respectively, confirming the significant red shift (**Figure 3-8A-D**). Primary peaks for the thicker films were located at 588 nm and 586 nm for 13 nm and 30 nm films on SiO<sub>2</sub>-coated silicon and 586 nm and

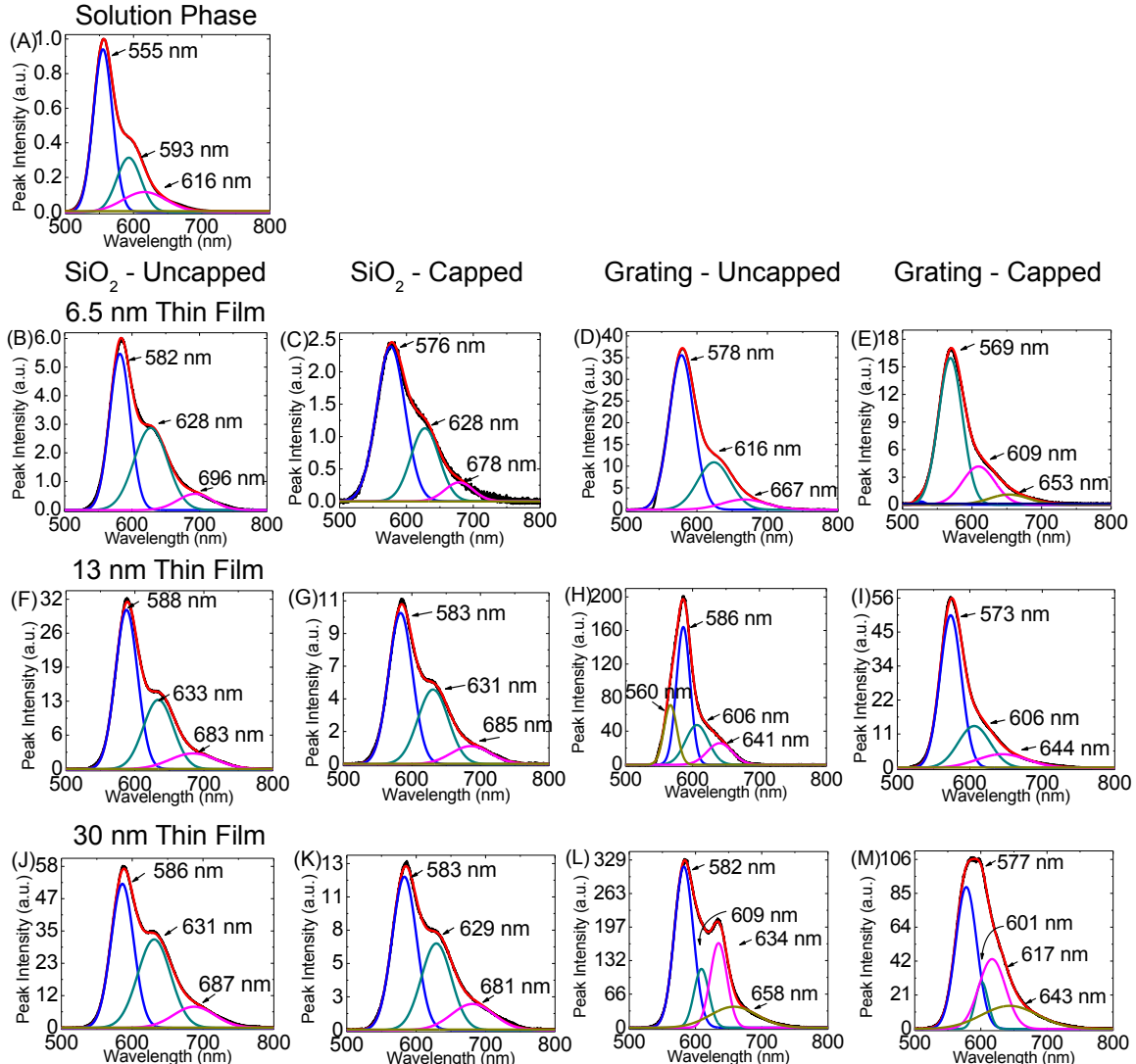


**Figure 3-8** MEH-PPV fluorescence of (A) chloroform solution (same for all concentrations used due to effect of high extinction coefficient); (B-E) Uncapped and capped 6.5 nm thin films on (B&C) SiO<sub>2</sub>-coated silicon and (D&E) silver plasmonic gratings; (F-I) Uncapped and capped 13 nm thin films on (F&G) SiO<sub>2</sub>-coated silicon and (H&I) silver plasmonic gratings; (J-M) Uncapped and capped 30 nm thin films on (J&K) SiO<sub>2</sub>-coated silicon and (L&M) silver plasmonic gratings. Peak intensities are the CPS intensity values scaled to 500 ms integration time and divided by 10,000 so that all values are on a common scale.

582 nm for films on silver gratings, respectively (**Figure 3-8E-M**). From these peak

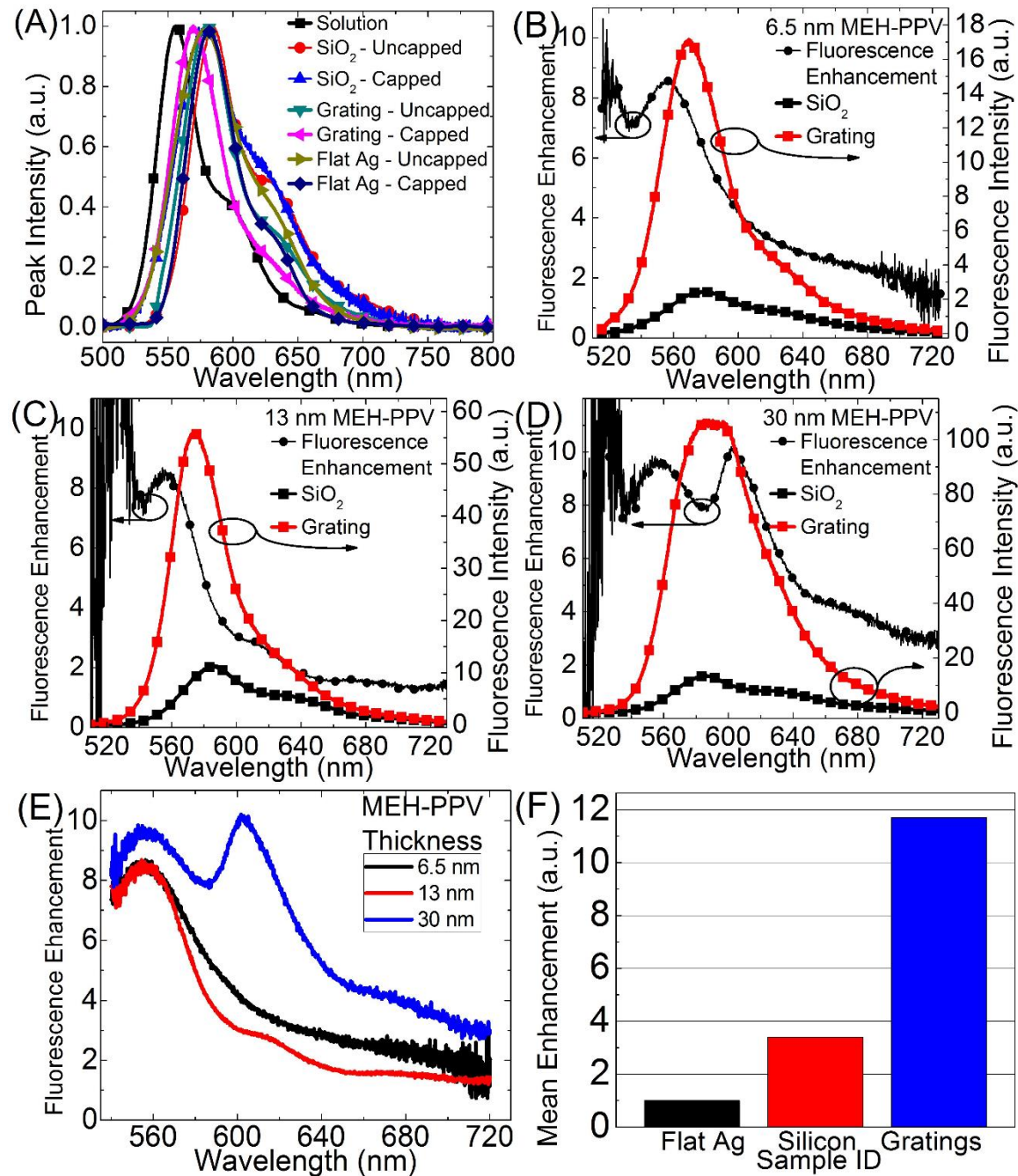


**Figure 3-9** (A) Normalized fluorescence spectra of uncapped and capped 6.5 nm MEH-PPV thin films with respect to 0.05% (w/v) chloroform solution; (B-D) Fluorescence spectra and associated wavelength-specific grating fluorescence enhancement factors of capped MEH-PPV thin films; (E) Comparison of wavelength-specific fluorescence enhancement factors of MEH-PPV thin films on plasmonic gratings with respect to SiO<sub>2</sub>-coated silicon; (F) Mean enhancement factors of capped 6.5 nm MEH-PPV thin films on various substrates with respect to flat silver.

values, we find that close proximity of MEH-PPV to the silver leads to additional apparent spectral modification aside from purely morphological characteristics. The few nanometer hypsochromic shift of the primary (0-0) peak on silver with respect to SiO<sub>2</sub>-coated silicon samples (**Figure 3-9A**) denotes shorter excited state electron diffusion distances prior to emission associated with shortened fluorescence lifetimes [149]. This was corroborated by MEH-PPV on flat silver exhibiting only ~30% the fluorescence intensity relative to SiO<sub>2</sub>-coated silicon (**Figure 3-9F**). Quenching of the polymer fluorescence by silver is in stark contrast to the fluorescence of Rhodamine-doped dielectric layers on flat silver where the dye is spaced 5-10 nm away from the metal, which show significant enhancement with respect to SiO<sub>2</sub>-coated silicon [65].

**Table 3-4 Peak Positions and Relative Intensities of 0.05% MEH-PPV Thin Film Fluorescence**

<i>Sample</i>	0-0 Peak		0-1 Peak		0-2 Peak	
	Position (nm)	Intensity (AU)	Position (nm)	Intensity (AU)	Position (nm)	Intensity (AU)
<i>Chloroform</i>	555	0.94	593	0.30	616	0.10
<i>Silica - Uncapped</i>	582	0.94	628	0.49	696	0.10
<i>Silica - Capped</i>	576	0.97	628	0.46	678	0.12
<i>Silver - Uncapped</i>	580	0.95	621	0.32	684	0.02
<i>Silver - Capped</i>	574	0.97	623	0.41	683	0.02
<i>Gratings - Uncapped</i>	578	0.96	616	0.29	667	0.06
<i>Gratings - Capped</i>	569	0.94	609	0.24	653	0.06

MEH-PPV fluorescence was significantly higher on silver plasmonic gratings than equivalent films on SiO<sub>2</sub>-coated silicon (**Figure 3-9B-D** and **Figure 3-10**) and the relative intensities of the 0-1 and 0-2 shoulder peaks with respect to the main peak were 50% lower than SiO<sub>2</sub>-coated silicon for the thinnest film (**Figure 3-9A** and compare **Figure 3-8B,C**). This spectral modification by silver plasmonic gratings leads to a wavelength-specific

fluorescence enhancement with respect to the intensity on SiO<sub>2</sub>-coated silicon that varies with increasing MEH-PPV thickness, as illustrated in **Figure 3-9B-D** and consolidated in **Figure 3-9E**. As predicted by FDTD in Section 3.3.2, we find that the wavelengths observed to be enhanced by the gratings correspond to those that would be coupled to the gratings and re-radiated at near normal incidence by a SPCE mechanism (**Figure 3-9E**). For the 6.5 nm and 13 nm samples (**Figure 3-9B,C**), enhancement is highest at  $\sim 8.5 \times$  for the blue edge of the primary (0-0) peak and decreases with increasing wavelength as the coupling angle and, thus, SPCE angles for the longer wavelengths lie beyond the  $\sim 17^\circ$  limit and are thus only partially captured by the microscope objective. Meanwhile, the 30 nm MEH-PPV films on gratings couple the longer wavelengths at near normal incidence (**Figure 3-9D**). The 0-0 transition has a near  $0^\circ$  coupling angle and the 0-1 transition also has coupling angle within the  $17^\circ$  acceptance cone (**Figure 3-2E**) and, subsequently, highest evanescent electric field component at the 0-1 transition (**Figure 3-2F**). This leads to the appearance of a fourth pseudo-peak between the 0-0 and 0-1 transition peaks in the thickest film (**Figure 3-8L,M**), which, in turn, gives rise to a sharp increase in the wavelength-

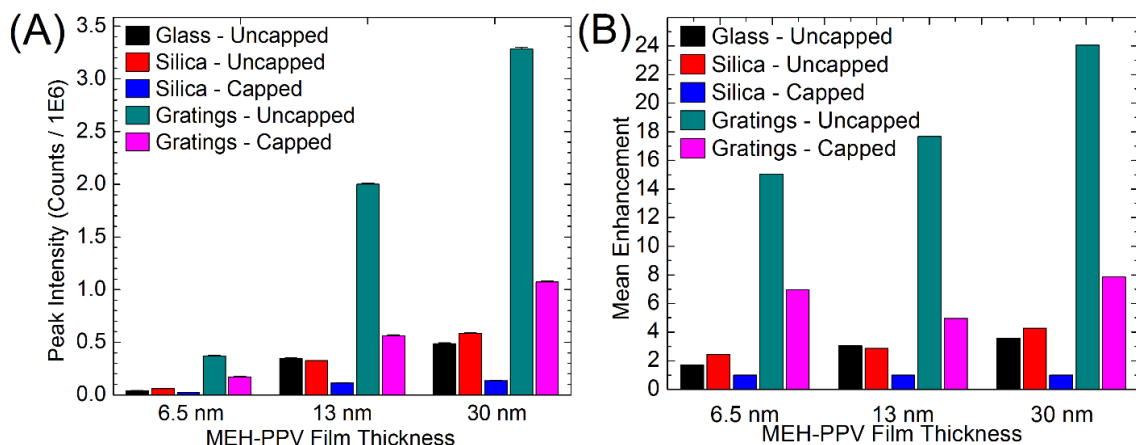


**Figure 3-10 (A) Peak fluorescence intensity values of MEH-PPV thin films on different substrates; (B) Mean enhancement factors of MEH-PPV thin films on different substrates normalized to film on silica.**

specific plasmonic enhancement curve around ~600 nm (**Figure 3-9E**) where the fluorescence curve on SiO<sub>2</sub>-coated silicon dips down sharply. Given the strong coupling efficiency and coupling angle for those wavelengths between 0-0 and 0-1, the significant enhancement is assigned to SPCE.

Capping MEH-PPV with the thin oxide film resulted in significant reduction in emission intensity (~60%) (**Figure 3-10A**), as well as further hypsochromic shifting and spectral broadening, with the primary peak blue-shifting from 583 nm to 577 nm for the film on silica and from 578 nm to 569 nm for plasmonic gratings (compare columns in **Figure 3-8**). All three spectral changes are consistent with reduced excited state electron travel distances associated with oxidative shortening of the polymer, which has the potential byproduct of reduced sensitivity to nitroaromatics should the damage-induced separation between excitable polymer sub-units be sufficiently extensive [147, 150]. As with the loss in initial intensity, the hypsochromic shift was less for the thicker films after capping due to the greater percentage of unaffected bulk material below the capping layer.

### 3.3.5 Photostability

Photostability is a primary issue in any fluorescence-based assay, but especially assays that rely on fluorescence quenching as the detection mechanism as it becomes critical to isolate potential false positives. Furthermore, oxidation shortens and isolates the conjugated molecules, leading to changing responses, increasing response times, as well as lowered sensitivity over the use life of the device. Capping or sealing fluorescent films in an impervious layer is a common method to prevent film degradation during photo- or electroluminescence [33, 126]. Protection afforded by a capping layer is related to the

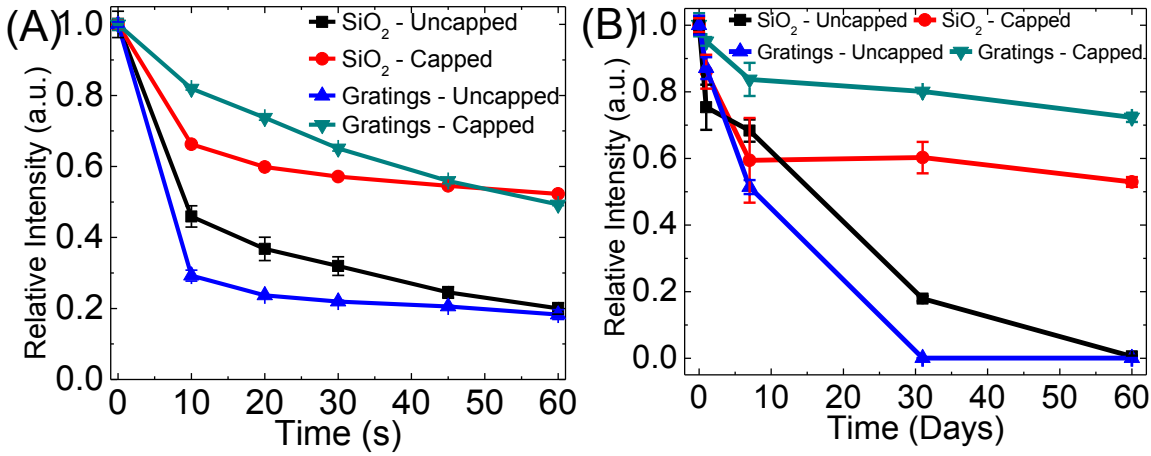


**Figure 3-11 (A)** Comparison of photodegradation of uncapped and capped MEH-PPV thin films on different substrates under constant illumination; **(B)** Long-term fluorescence stability of uncapped and capped MEH-PPV thin films on different substrates stored in dark, ambient conditions.

thickness and density of the layer affecting the permeability post-processing as well as the presence of residual oxygen or moisture in the polymer layer. As we have 0.17 void fraction or ‘porosity’, this semi-permeable oxide layer was studied for its photo-oxidation protective properties and utility for thin film fluorescence-based sensors.

MEH-PPV photostability was studied under two conditions: (1) continuous illumination of the films and (2) long-term storage under dark, ambient conditions in the lab (**Figure 3-11**). Fluorescence of the uncapped films on both SiO<sub>2</sub>-coated silicon and gratings reduced by more than 60% of the initial intensity within 10 seconds of continuous blue (475 nm ± 15 nm, ~2 mW/cm<sup>2</sup>) illumination (**Figure 3-11A**). Spectral broadening and blue-shifting of the primary peak also occurred (**Figure 3-12**), which are consistent with oxidative shortening of conjugated polymers [147]. Blue shifting and loss of shoulder peaks indicate reduced pre-emission excited state electron diffusion resulting from lower inter- and intra-chain interaction akin to dimerization in traditional organic fluorophores. Less intense and poorly-defined peaks in concert with hypsochromic shifting mark the

generation of a growing population of shortened MEH-PPV chains that are excited and emit at higher frequencies (i.e. lower wavelengths) as well as non-fluorescent species. For the films on gratings, these wavelengths quickly pass beyond the 17° SPCE range and,

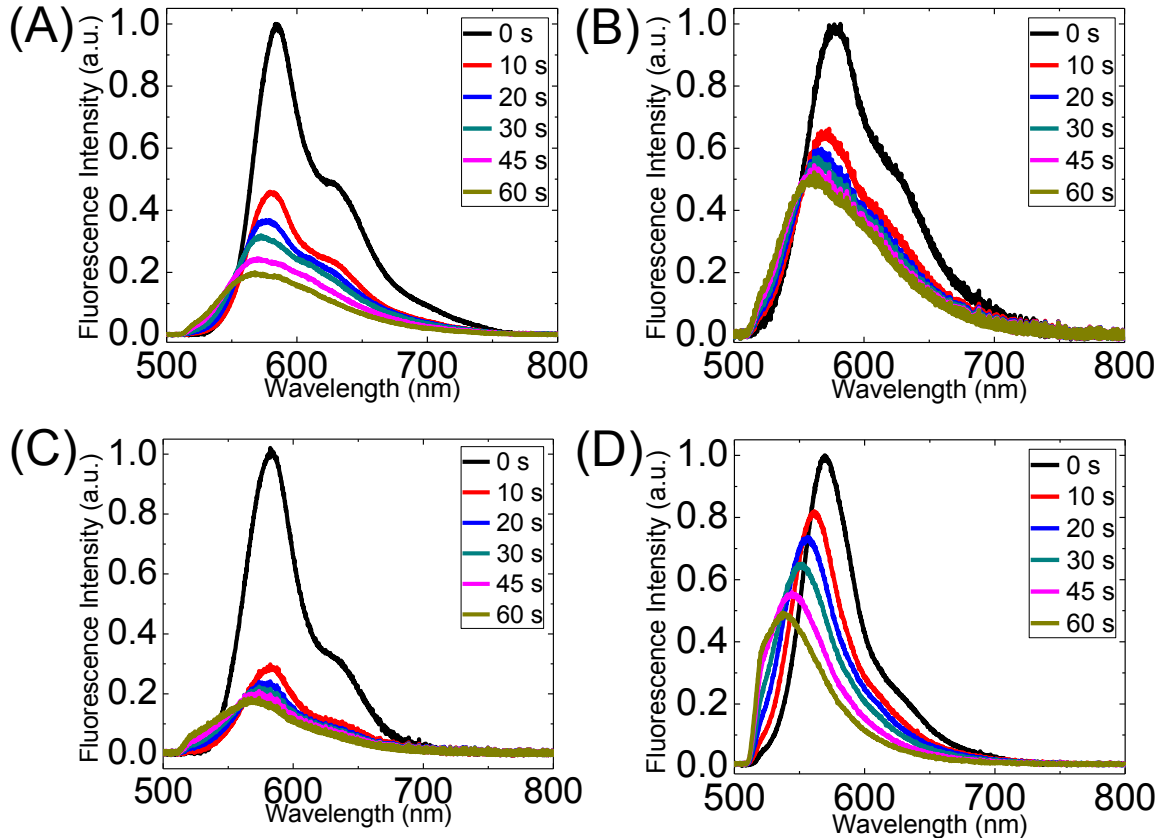


**Figure 3-12 (A-D)** Fluorescence spectral evolution of uncapped and capped MEH-PPV thin films during continuous illumination; (A) Uncapped 6.5 nm film on optimized SiO<sub>2</sub>-coated silicon; (B) Capped 6.5 nm film on optimized SiO<sub>2</sub>-coated silicon; (C) Uncapped equivalent film on silver gratings; and (D) Capped equivalent film on silver gratings.

when combined with the more frequent excitation and higher excitation evanescent field, lead to rapid drop in fluorescence intensity (blue curve, **Figure 3-11A** and **Figure 3-12C**).

Addition of the capping layer improved initial fluorescence stability to 66% for films on optimized SiO<sub>2</sub>-coated silicon and 82% for films on silver gratings owing in part to scavenging of oxygen and moisture by the oxide capping layer leading to slower permeation through the closed porosity (**Figure 3-11A** and **Figure 3-12B,D**). This was

further confirmed by the slower diffusion rate of nitroaromatics through the silica capping layer as described in Section 3.3.6. The increased stability on gratings with respect to SiO<sub>2</sub>-coated silicon was due to a combination of the substrate geometry, silver proximity, and capping layer morphology over MEH-PPV on silver, which is a matter of ongoing study. Meanwhile, the final steady-state decay rate on plasmonic gratings is slightly higher than for SiO<sub>2</sub>-coated silicon (**Figure 3-12D**). The increased steady-state decay rate is due to a competition between higher excitation rates on the silver leading to more opportunities for oxidation to occur and excited state electron quenching by the silver itself.

Long-term storage was carried out for 2 months by wrapping a set of films in foil and storing in dark, ambient lab conditions (temperature ≈ 22 °C and relative humidity ≈ 30-50%). During this time, the uncapped polymer films degraded entirely, with most of that loss occurring within the first few weeks (**Figure 3-11B**). Meanwhile, the capped films on SiO<sub>2</sub>-coated silicon retained just over 50% and gratings retained more than 70% of their initial fluorescence intensity throughout the 2 month testing period. Both capped films did experience an initial drop in fluorescence within the first week followed by a period of relative stability for the next few weeks. The gratings experienced only 15% loss in the first week compared to 40% for SiO<sub>2</sub>-coated silicon. This suggests an initial sensitization of areas exposed directly to oxygen and moisture in the air through the pores in the capping layer followed by a period of markedly slower diffusion of oxygen and moisture laterally into the film underneath the layer. This is an important result for the fact that it shows longevity of ultra-thin conjugated polymer films even in the presence of a porous capping layer and under non-inert environmental conditions. Such stability and

longevity is critical as changes in baseline fluorescence reduce dynamic range and sensitivity as mentioned above. Furthermore, this suggests the films could be used long-term as part of a semi-permanent sensor installation.

### 3.3.6 Exposure to Nitroaromatics

MEH-PPV has already been studied extensively for its specific and advantageous quenching interaction with nitroaromatic (NA) vapors with respect to alternative conjugated polymers [11, 13, 26]. Thus, we are concerned primarily with the synergistic interplay between the polymer and the plasmonic substrate as applied to improved sensor response. Quenching studies were first performed on uncapped (**Figure 3-13A-C**) and capped (**Figure 3-13D-F**) 6.5, 13, and 30 nm thin films on SiO<sub>2</sub>-coated silicon. Uncapped films of all thicknesses achieved greater than 90% quenching of initial fluorescence intensity within 10 s exposure to saturated DNT vapor, consistent with previous reports [13]. Also significant was the substantial recovery of fluorescence on removal from the vapor source as shown by the + time curves in the graph. The uncapped 6.5 nm film

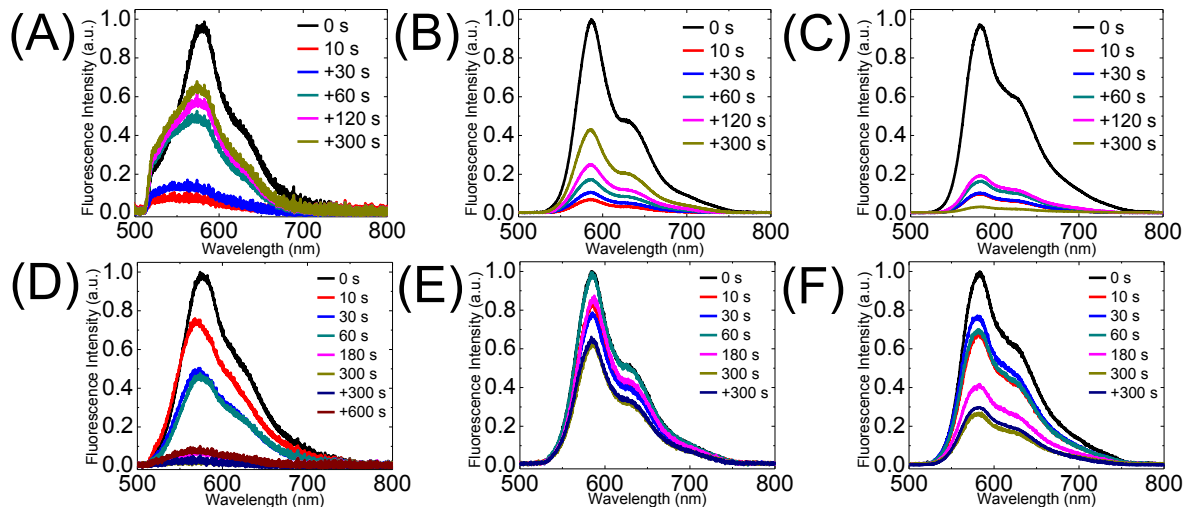


**Figure 3-13 Quenching response and recovery of (A-C) uncapped and (D-F) capped (A&D) 6 nm, (B&E) 13 nm, and (C&F) 30 nm MEH-PPV thin films on silica**

recovered the most percentage fluorescence in the measured time period here (**Figure 3-13A**) while thicker films were slow to recover as expected since the quenching is a collisional, diffusion-based process. Furthermore, all of the uncapped films suffered from rapid oxidative photobleaching within the study period, as indicated by the blue-shifting and spectral broadening, which is again most prominent in the thinnest film (**Figure 3-13A**). This degradation masked the recovery from quenching for uncapped films, especially at longer recovery time periods.

As expected, capped films on SiO<sub>2</sub>-coated silicon exhibited slower fluorescence quenching than uncapped films as a result of slower molecular diffusion through the porous silica capping membrane and laterally into the film. However, greater than 90% quenching did still occur within 300 s (5 min) of exposure using the 6.5 nm films. Recovery for the capped films was also slower after removal from the vapor source, again evidence of slowed diffusion (in this case, out of the film). However, it is notable that the films did eventually recover full fluorescence intensity after several hours and the peak location was identical to the initial peak location, confirming quenching and not photodegradation as the source of the intensity loss. These films could be used repeatedly with very similar responses, though exposure to the excitation light should be limited to prevent oxidative photobleaching as discussed above. The thicker films not only exhibited slower and less significant intensity losses as a result of slower diffusion times and larger concentration of quenchable material, but also showed much slower recovery, again suggesting diffusion as the mechanism for interaction with the polymer through these films.

**Figure 3-14A,B** shows the evolution of 2,4-DNT quenching behavior of the capped MEH-PPV films on both SiO<sub>2</sub>-coated silicon, flat silver, and plasmonic grating substrates. After 1200 s (20 min) of exposure, the film on SiO<sub>2</sub>-coated silicon had quenched 87.5% while the film on gratings had quenched 99.7%. The critical initial 60 s response to 2,4-DNT in the linear (i.e. unsaturated) quenching region was ~33% on the film on SiO<sub>2</sub>-coated silicon compared to more than 80% for the films on plasmonic gratings, corresponding to a quenching rate of 0.008 s<sup>-1</sup> and 0.057 s<sup>-1</sup> for SiO<sub>2</sub>-coated silicon and plasmonic gratings,

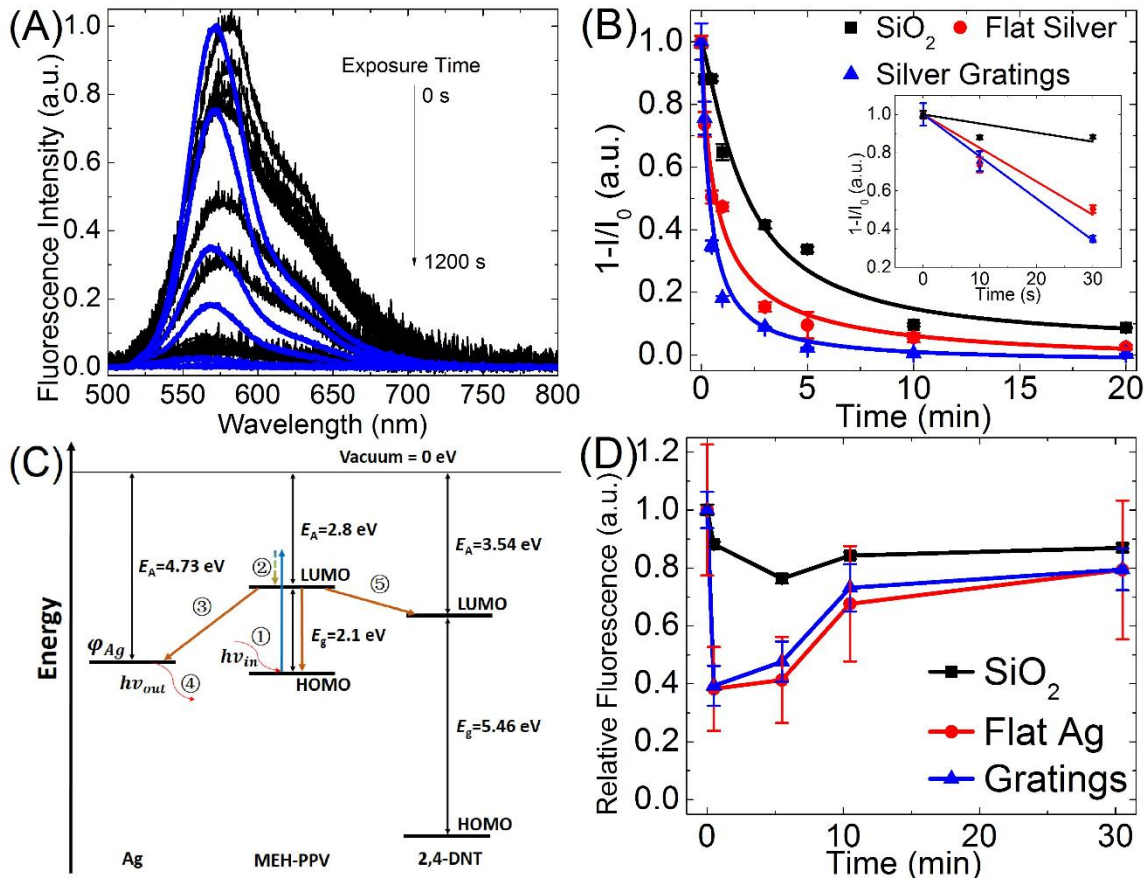


**Figure 3-14** (A) Spectra of progressive fluorescence quenching of MEH-PPV on SiO<sub>2</sub>-coated silicon (black) and plasmonic gratings (blue) by exposure to 2,4-DNT; (B) Quenching of capped MEH-PPV films on SiO<sub>2</sub>-coated silicon, flat silver, and silver plasmonic gratings (Inset); (C) Band diagram showing competing interactions of MEH-PPV, Silver, and 2,4-DNT in the grating setup; and (D) Recovery of capped MEH-PPV films on SiO<sub>2</sub>-coated silicon and silver substrates after 30 s quenching by 2,4-DNT.

respectively (**Figure 3-14B, inset**). The increase in initial quenching rate is roughly  $7\times$  that on  $\text{SiO}_2$ -coated silicon, which is attributed to a competition between excited state coupling to silver through SPCE (**Figure 3-14C: 1-4**) and non-radiative energy transfer to the impinging 2,4-DNT molecules (**Figure 3-14C: 1,5**). In the SPCE case, MEH-PPV fluorescence is increased due to rapid coupling of the emitted fluorophore to the silver, shorter fluorescence lifetime, and directed emission toward the detector, whereas fluorescence on  $\text{SiO}_2$ -coated silicon is isotropic and there is negligible modification of lifetime by  $\text{SiO}_2$ . On interaction with NA vapor, 2,4-DNT disrupts the radiative pathway and introduces an energetically favorable non-radiative pathway so long as the 2,4-DNT molecule is in close proximity to the MEH-PPV. The rate of fluorescence fall-off in the SPCE case is higher since more detectable photons are lost per interaction, namely, those coupled and rapidly re-radiated toward the detector by SPCE. This is important as it shows the utility of SPCE not only for increasing signal, but also improving observation of analyte interactions through dynamics in the preferential directed emission.

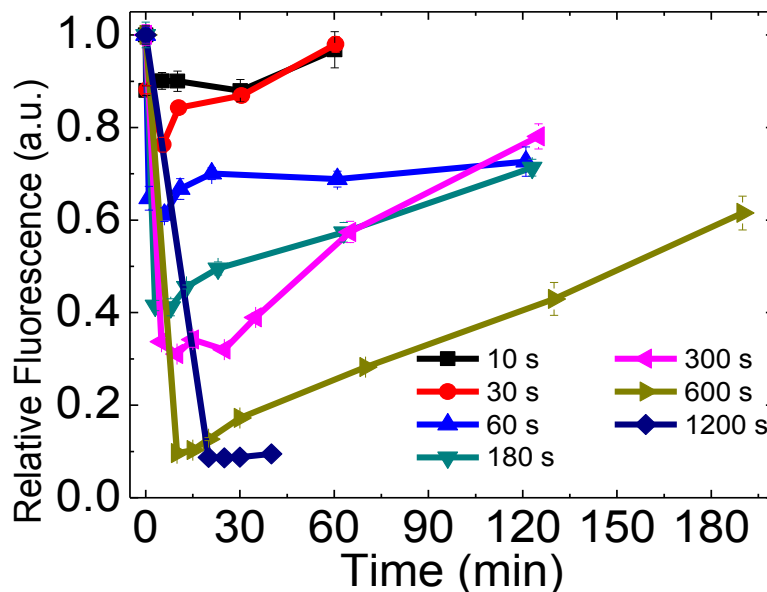


**Figure 3-15 Long-term fluorescence recovery after quenching by DNT.**

As a result of the preservation of the material from oxidation by the capping layer, the capped films recover gradually from their exposure (**Figure 3-14D**, **Figure 3-15**). For each sample, fluorescence recovery occurred at a rate ~20% the initial intensity per hour after an initial lag phase. This lag phase is thought to result from over-saturation of the polymer layer as well as slower diffusion out of the film due to the interaction between the NA molecules and the MEH-PPV. Thus, the degree of quenching and fluorescence recovery time could be used as an indicator of total exposure time or vapor pressure in an *in situ* measurement. Finally, the fluorescence recovery after DNT exposure continued with time such that films left unexposed for a few hours completely recovered to their initial fluorescence intensity and could be used repeatedly with nearly identical results to the first exposure event (i.e. no pre-sensitization).

### **3.4 Conclusions & Future Direction**

Low-cost metallic plasmonic gratings and ultra-thin oxide ( $\text{SiO}_2$ ) capping layer were evaluated as means to improve the stability, signal, and sensitivity of fluorescent conjugated polymer (FCP) chemosensors. Fluorescence of the resultant capped, plasmonic-enhanced films was enhanced more than seven-fold primarily by surface plasmon-coupled emission (SPCE). This enhancement permits two possible modes of sensor improvement: (1) the use of reduced excitation intensities to provide fluorescence similar to films on silica/glass and thus prolong the life of the device or (2) the use of similar excitation intensities to provide drastic improvements to signal-to-noise ratio and the sensitivity of the device. Sample fluorescence was preserved by the low-density capping layer both during active use and storage in ambient air for several months.

Meanwhile, the porosity in the capping layer allowed the MEH-PPV films to retain their rapid quenching response to nitroaromatic vapors, with thin capped films on gratings quenching at a rate more than 7 times faster than similar films on SiO<sub>2</sub>-coated silicon due to competition between excited state electron diffusion and relaxation pathways. Furthermore, MEH-PPV films exposed to 2,4-DNT were able to recover fluorescence with time, allowing for multiple use cycles and as dynamic sensors and the use of recovery after removal from the vapor source as a means of distinguishing between compounds. These unique properties show great promise toward enhancement of other FCP sensor systems for embedded sensors in real-world applications.

# **CHAPTER 4 MONITORING STEADY-STATE NITRO-AROMATIC VAPOR DIFFUSION THROUGH A HETEROGENEOUS LAMINATE THIN FILM**

## **4.1 Introduction**

As discussed in Chapter 2 and shown through experimental results in Chapter 3, fluorescent conjugated polymers (FCPs) such as poly-[2-methoxy-5-(2-ethylhexyloxy)-*p*-phenylenevinylene] (MEH-PPV) are quenched by nitroaromatic (NA) compounds such as 2,4-dinitrotoluene (2,4-DNT) through an energetically favorable electron transfer process resulting from the overlap of the 2,4-DNT LUMO level with the band gap of MEH-PPV [11, 13, 26]. This process results in a strong lights-off quenching response, which can be used under certain conditions to identify presence and quantity of 2,4-DNT vapor. It has been noted that extremely close molecular interaction of the quencher (2,4-DNT) with the signal transducer (MEH-PPV) is an essential aspect of the sensitivity of the fluorescence quenching mechanism. In the absence of a capping layer, 2,4-DNT vapor at room temperature diffuses freely and rapidly to its saturated vapor pressure (~290-300 ppb) as given by Fick's law [151]

$$J = -D_{ia} \partial \phi / \partial x \text{— Eq. 4.1}$$

where  $J$  is the diffusion flux,  $D_{ia}$  is the diffusivity, and  $\partial \phi / \partial x$  is the concentration gradient with space. Diffusion to and into the MEH-PPV film is unimpeded, allowing intermixing

and interaction of 2,4-DNT with individual MEH-PPV molecules on extremely short time scales and leading to rapid, complete quenching of the thin films [152, 153].

Adding the capping layer understandably increases the fluorescence quenching time at similar experimental conditions. The small void fraction measured for the capping oxide layer in Chapter 3 suggests closed, disconnected porosity [108, 115, 154], meaning that the pores consist of narrow, tortuous paths that may decrease the diffusivity of 2,4-DNT significantly with respect to that in ambient air. The restricted, effective diffusivity ( $D_e$ ) is given by [155]

$$D_e = \frac{D_{ia}\varepsilon_t\delta}{\tau} \quad \text{Eq. 4.2}$$

where  $D_{ia}$  is the free space diffusivity,  $\varepsilon_t$  is the layer porosity,  $\delta$  is the pore constrictivity or ratio of the molecular size to the pore diameter, and  $\tau$  is the tortuosity of the pore or ratio of the actual path length inside the pore to the actual layer thickness (~5 nm as measured by ellipsometry). While the oxide capping layer porosity is known ( $\varepsilon_t = 0.17$ ), the exact individual pore diameters and path lengths are unknown and will vary stochastically from pore to pore depending on the *in situ* silicon dioxide deposition characteristics. Thus,  $\delta/\tau$  can be thought of as a pore-specific restriction coefficient. It can be seen from Eq. 4.2 that the free space diffusivity is reduced by at least ~6-fold on entering the porous medium even in the absence of any restriction coefficient. Direct observation of 2,4-DNT diffusion through the porous oxide capping layer is not possible as the molecules must necessarily have navigated the pores before reaching the fluorescent MEH-PPV layer and onset of quenching. However, monitoring the effects of 2,4-DNT exposure on capped MEH-PPV thin films by fluorescence image analysis may provide valuable information about the

diffusion of 2,4-DNT through the porous layer and the MEH-PPV thin film itself, as well as possibly used to interpret rate constants of interaction between 2,4-DNT and MEH-PPV.

## 4.2 Experimental Section

### 4.2.1 Chemicals and Materials

Standard glass microscope slides were purchased from Fisher Scientific (Pittsburgh, PA) and silicon wafers from MEMC (St. Peters, MO). Polydimethylsiloxane (PDMS, Sylgard® 184, Dow Corning, Inc.), poly-[2-methoxy-5-(2-ethylhexyloxy)-p-phenylenevinylene] (MEH-PPV,  $M_n$  40,000-70,000), 2,4-Dinitrotoluene (2,4-DNT), 1,3-Dinitrobenzene (1,3-DNB), Nitrobenzene (NB), hydrofluoric acid (HF), ammonium fluoride ( $NH_4F$ ), and all organic solvents were purchased from Sigma-Aldrich (St. Louis, MO) and polymethylsilsesquioxane (PMSSQ, GR650F) from Techneglas (Perrysburg, OH).

### 4.2.2 Substrate Preparation

Two capped polymer-coated substrates were prepared for characterization and nitroaromatic sensing measurements: silicon oxide and silver plasmonic gratings. Silicon oxide was chosen due to its low fluorescence background with respect to glass slides. Before oxide growth on silicon, each 5 cm × 5 cm wafer piece was cleaned by sonication in successive baths of acetone, methanol, and deionized water (18.2 MΩ-cm) and then dipped in 1:10 HF:H<sub>2</sub>O for 1 minute. Dry thermal oxide was grown at 1100 °C by flowing 5 cfm oxygen in a quartz tube furnace and etched to different thicknesses by 1:15 HF:NH<sub>4</sub>F buffered oxide etching solution for 0-300 s [137]. Oxide thicknesses were verified by variable angle spectroscopic ellipsometry (VASE, J.A. Wollam, Inc.).

Silver plasmonic gratings were made by micro-contact printing as described previously [65]. Briefly, PDMS (5:1 base:crosslinker) was poured and cured over an isopropanol-cleaned HD-DVD to generate a master mold. Cured PDMS slabs were then cut into 1x1 cm<sup>2</sup> stamps and used to print the polymer ink, 3% w/v PMSSQ dispersed in ethanol, onto freshly-cleaned silicon. The stamp was peeled off after a few seconds and the ink was allowed to dry in ambient conditions. The polymer gratings were then transferred to an AJA RF Magnetron sputter system and a 2 nm titanium adhesion layer was deposited followed by 100 nm silver using 100 W RF power, 20 sccm argon flow, and 4 mTorr working pressure. Samples were then transferred to a nitrogen-purged glove box prior to further use.

Immediately prior to spin-casting MEH-PPV, all substrates were cleaned thoroughly with acetone, methanol, and 2-isopropanol, blown dry with nitrogen, and transferred to the glove box. MEH-PPV was dissolved in chloroform to 0.5 mg/mL and spin-cast at 3000 rpm for 30 seconds and stored in vacuum overnight to ensure removal of excess solvent. Some of these substrates were then transferred to a Kurt J. Lesker electron beam physical vapor deposition chamber and capped with 5 nm SiO<sub>2</sub> layer. All substrates were then stored in the glove box until measurement.

#### 4.2.3 Response to Nitroaromatics

Quenching response to 2,4-Dinitrotoluene (2,4-DNT), 1,3-Dinitrobenzene (1,3-DNB), Nitrobenzene (NB), and ammonium nitrate were tested according to a protocol similar to that by Chang *et al.* [13]. Briefly, a 20 mL glass vial was filled with 2 g dry powder (2 mL for liquid NB) and covered by several layers of cotton gauze to prevent direct physical

contact. Samples were placed into the container face-up on the cotton and capped for a specified period of time (10-1200 seconds). Before and after measurements were taken in triplicate and averaged for each sample condition.

### 4.3 Results and Discussion

#### 4.3.1 Response to Nitroaromatic Vapors

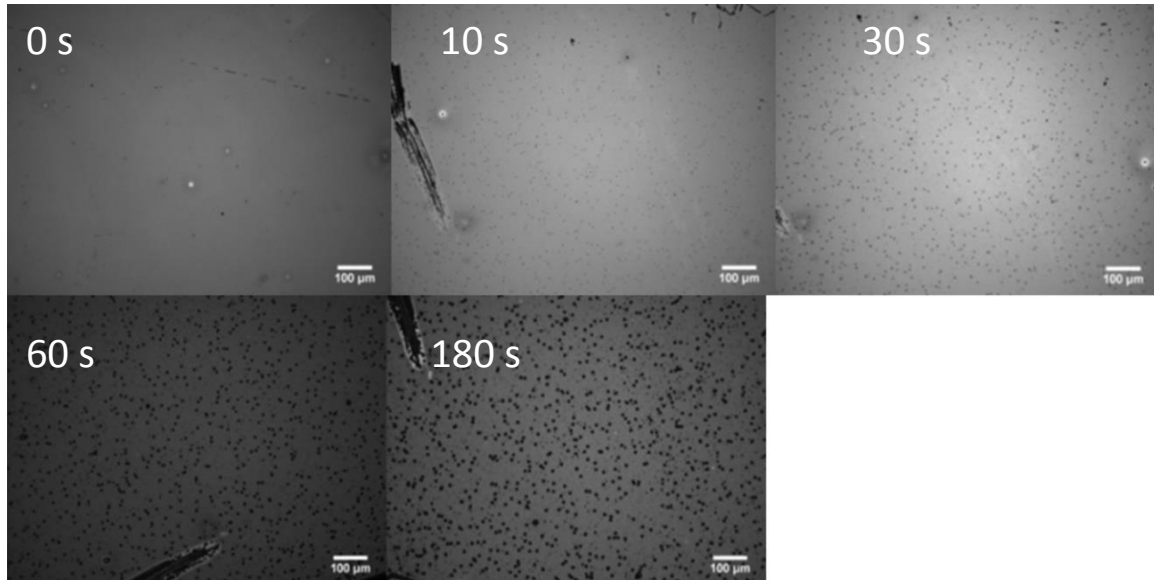


**Figure 4-1** Fluorescence images of capped 6.5 nm MEH-PPV thin film on SiO<sub>2</sub>-coated silicon on exposure to saturated 2,4-DNT vapor. Image Parameters: 10× objective, 475 nm excitation, 25% and 6% ND filters, 100 ms exposure time, and 200× gain.

**Figure 4-1** shows fluorescence images of the quenching response of capped 6.5 nm MEH-PPV thin films on SiO<sub>2</sub>-coated silicon to saturated 2,4-DNT vapor with increasing exposure time. In these images, higher pixel values (i.e. whiter points) indicate high fluorescence intensity whereas lower pixel values (i.e. darker points) indicate lower fluorescence intensity or quenching. The apparent increase in intensity between 0 seconds and 10 seconds exposure is an artifact caused by automatic baseline subtraction performed by the ImageJ analysis software. Interestingly, the quenching response is not uniform over the entire substrate surface, but instead occurs in two apparent stages as seen in the

fluorescence micrographs of the quenching event. Quenching appears to initiate at singular points or nodes in the film, indicated by the dark spots in the fluorescence micrographs at 10 seconds exposure and higher. The quenched (i.e. darkening) areas of the film expand radially with increasing exposure time, eventually coalescing and producing an entirely blackened area. This phenomenon was also seen with increasing MEH-PPV film thickness. By analyzing the spot count and areas using ImageJ particle analysis tool (here, quenched fluorescence is defined as a “particle”), we see that quenched areas both grow and become more numerous with increasing exposure time. **Figure 4-2** and **Figure 4-3** show box-and-whisker plots indicating the population ranges of areas MEH-PPV fluorescence quenched by 2,4-DNT. These population statistics help to visualize the

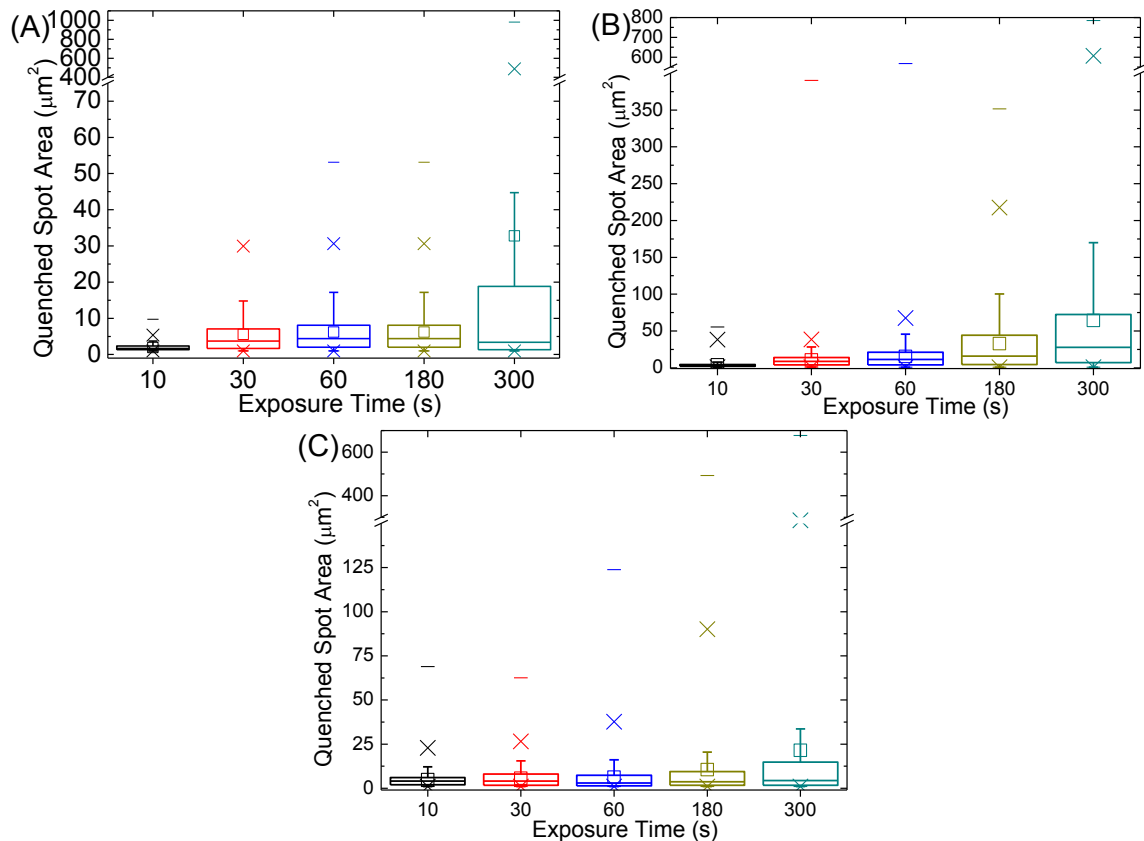


**Figure 4-2 (A-C)** Box-and-whisker plots of quenched spot areas of (A) 6.5 nm, (B) 13 nm, and (C) 30 nm capped MEH-PPV thin films after exposure to 2,4-DNT vapor.

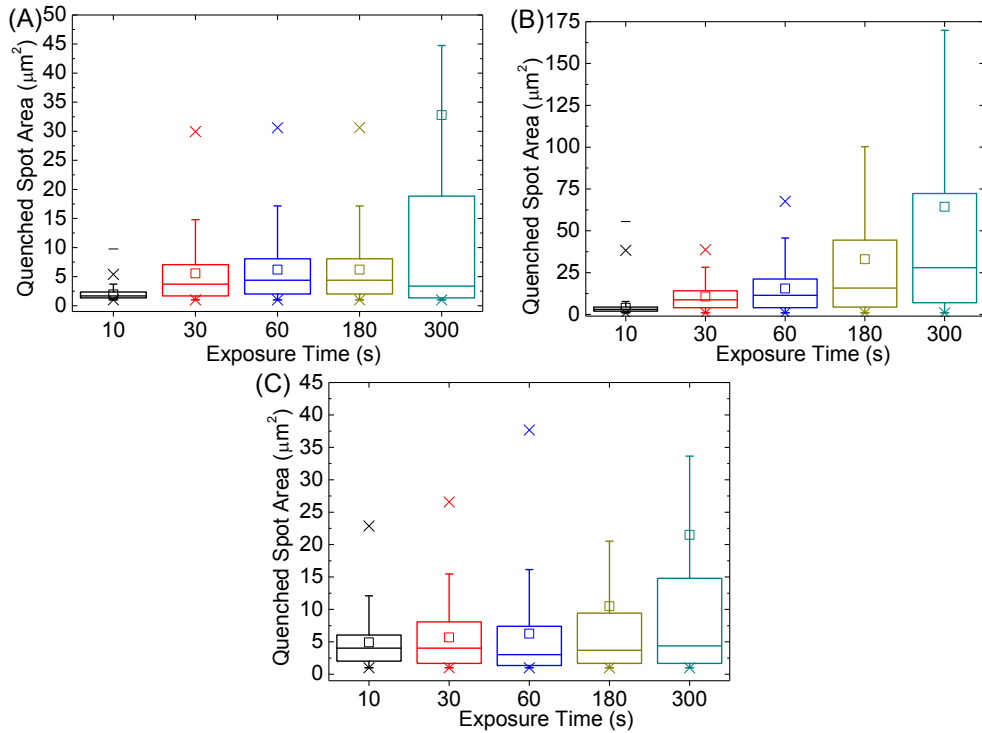


**Figure 4-3 Box-and-whisker plots from Figure 4-2 focused on means (□), numerical population 25/75 percentiles (boxes), and whiskers (outliers).**

growth in size of individual ‘particles’ (i.e. quenching regions of the capped MEH-PPV thin films) with increasing 2,4-DNT exposure time. As can be seen, average quenched region size increases rapidly with increasing exposure time from 10 to 180 s exposure. The 300 s exposure box and whisker is somewhat anomalous in that the average region size decreases for the thinnest film, as evidenced by the slight average decrease in **Figure 4-3A**. This appears inconsistent with the sequential growth of quenched areas in the images in **Figure 4-1** until considering the merger of individual particles to form a lower number of larger particles. This is evidenced by the drastic increase in size of the top 10% of quenched regions to nearly 1000 pixel diameter (**Figure 4-2A**). Meanwhile, we see that the largest particles for thicker films are consistently lower and trend downward with increasing MEH-PPV thickness (800 pixels for 13 nm film and 600 pixels for 30 nm film). We also

see in **Figure 4-3B,C** a much higher population of smaller quenched regions between 10 – 50 pixels in diameter. This is consistent with the hypothesis of the appearance of quenching being limited by both vertical and lateral diffusion of 2,4-DNT due to the increased volume of MEH-PPV to be quenched. The thicker films may also be more continuous and densely packed than the 6.5 nm film as evidenced by the increased refractive index trending toward the bulk refractive index of MEH-PPV (**Table 3-1**). This would have an increased effect on constrictivity for lateral diffusion, slowing quenching rates significantly.

#### 4.3.2 Comparison of Quenching Rates

Another significant difference between the 2,4-DNT fluorescence quenching on silicon and gratings was the apparent quenching rate (**Figure 3-14**). As mentioned in the previous chapter, the 60 s quenching response was 30% for films on silicon and 80% for films on gratings. Quenching by standard dipole-dipole interaction processes is best defined by the Stern-Volmer relation [26]

$$\frac{I_0}{I} = 1 + K_{SV}[Q] \text{ -- Eq. 4.3}$$

where  $I_0$  is the initial intensity,  $I$  is the intensity in the presence of quencher (analyte) molecule,  $[Q]$  is the analyte concentration, and  $K_{SV}$  is the quenching constant in units  $M^{-1}$ . As the samples were exposed to vapor in a small, enclosed volume, we can assume a steady-state vapor pressure is achieved if the exposure time is greater than the time for vapor to equilibrate in the chamber. From Fick's Law, the order of the time to reach a steady-state vapor pressure in the reaction chamber (i.e. head space of the 20 mL vial) is given by [155]

$$\langle x^2 \rangle \approx q_i D t \text{ -- Eq. 4.4}$$

where  $x$  is the height of the volume into which the 2,4-DNT vapor is expanding ( $\sim 1$  cm),  $D$  is the diffusivity of 2,4-DNT vapor in air at STP ( $D_{ia} = 2.03 \times 10^{-1}$  cm $^2$ /s) [156],  $t$  is the travel time, and  $q$  is a positive integer. Solving for  $t$  given the physical constraints of the vial test system provides an approximate vapor pressure equilibration time of 5 seconds. Since the first measurement was taken after 10 seconds exposure, a steady-state vapor condition can be assumed and the measured quenching response will be dominated by NA diffusion through the capping layer and into the polymer film. This diffusion-limited condition allows the use a modified form of the Stern-Volmer equation describing the quenching rate of a single analyte concentration over a period of time

$$\frac{I_0}{I} \approx 1 + K'_{SV} t \quad \text{Eq. 4.5}$$

where  $K'_{SV}$  is the modified quenching rate in units of s $^{-1}$  and comprises both diffusion and interaction rates. **Figure 4-4A** shows the time-based Stern-Volmer plot for substrate response to 2,4-DNT. The quenching response follows a linear trend for all substrates within the first few minutes of interaction, after which the signal from the film tends to zero and the ratio  $\frac{I_0}{I}$  becomes erratic and nonlinear. Thus, it is critical to isolate the linear region for calculation of  $K'_{SV}$  (**Figure 4-4B**).  $K'_{SV}$  on silicon was found to be 0.008 s $^{-1}$ , while the quenching rate on silver was 0.030 s $^{-1}$  and silver gratings was 0.057 s $^{-1}$ , an increase of 3.7-fold and 7.1-fold, respectively. Combining the enhanced rate with the photostability, recovery, and longevity afforded by the capping layer, this sensor represents a significant step toward a realizable portable fluorescence sensor unit for nitroaromatic detection.

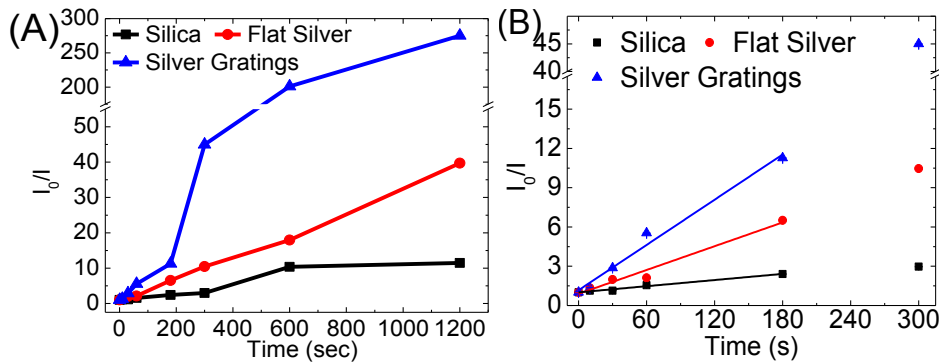


**Figure 4-4 (A & B)** Modified Stern-Volmer plots showing quenching rate of capped MEH-PPV thin films with exposure time to 2,4-DNT (line in B represents fit of linear region).

#### 4.3.3 Sensor Cross-reactivity to Other Nitroaromatics

Sensitivity of the films to other nitroaromatic compounds was also tested in a similar manner with a small amount (~2 g) of analyte at the bottom of a small glass vial covered in a small piece of cotton as a physical barrier. Films on both silicon and gratings quenched rapidly and completely in the presence of NB vapor while having slower responses to 1,3-DNB (**Figure 4-5B,C**). The higher response to NB is explained by its much higher vapor pressure, which allows faster diffusion into the polymer film while 1,3-DNB has a vapor pressure on the same order as 2,4-DNT and less electron structure destabilization (**Table 4-1**) [100]. The vapor-phase Stern-Volmer quenching rates were also analyzed for NB and 1,3-DNB (**Figure 4-5D,E**) and the rates results are summarized in **Table 4-1**. Notably, the response on gratings is proportionally less for 1,3-DNB than on silicon (~32% the 2,4-DNT response on gratings versus ~60% on silicon). Meanwhile, the rates for NB are higher owing to the higher vapor pressure of NB leading to faster achievement of vapor pressure inside the vial. As the vapor pressure of 1,3-DNB is higher than 2,4-DNT, it was thought that the lower quenching rate would be explained by the relative overlap of the LUMO level with the HOMO of the MEH-PPV. The overlap can

be considered favorable for quenching when the electron transfer reaction free energy change ( $\Delta G^\circ$ ) is negative (i.e. electron transfer is favored thermodynamically) [11-13, 157].

This form of  $\Delta G^\circ$  is approximated by the equation [13]

$$\Delta G^\circ = -e[E(P/P+) - E(Q/Q^-)] - \Delta E_{0-0},$$

where  $E(P/P+)$  is the oxidation potential of the polymer,  $E(Q/Q^-)$  is the reduction potential of the quencher,  $\Delta E_{0-0}$  is the lowest singlet 0–0 excitation energy of the polymer, and  $e$  is the electron unit charge, included to indicate the conversion between electrochemical potential and energy. For our calculations,  $E(P/P+)$  for MEH-PPV was given as 0.7 V [158],  $E(Q/Q^-)$  is given for each nitroaromatic compound in **Table 4-1** below [159]. The value of  $\Delta E_{0-0}$  was found graphically by noting the intersection of the normalized absorbance and emission spectra in accordance with [26] and given to be 2.2 eV for our samples. Estimated values for  $\Delta G^\circ$  were negative for all the nitroaromatics tested with TNT having the most favorable interaction, as expected given its highly electron-deficient nature. However, in this case, 1,3-DNB has a slightly more favorable interaction. The difference must come from the relative destabilization of the electron center by the methyl group of the 2,4-DNT [160-162].

Desorption of NB on removal from the vapor source was so rapid that the films on gratings had begun recovering fluorescence within the time frame that measurements were taken, typically less than 10 seconds from removal from the exposure vial (**Figure 4-5B and Inset**). Meanwhile, desorption of 2,4-DNT takes much longer, on the order of minutes to days depending on the length of exposure. This characteristic alone could be utilized as a means of distinguishing selectively between NB and other NA compounds in a field

sensing application. Immediate fluorescence recovery on removal from NB vapor is notably unapparent from the capped films on silicon, as seen from the small error bars for the NB points in **Figure 4-5A**. This does not preclude the occurrence of recovery, but the signal-to-noise ratio is low enough at those intensities such that the effect is unnoticeable at short recovery times. It also supports the idea that diffusion through the oxide layer into the polymer layer is less for the grating platform, but that quenching occurs primarily through extension of the RET distance by the metal such that the NB desorption from the film on gratings has a greater immediate effect on the fluorescence recovery.

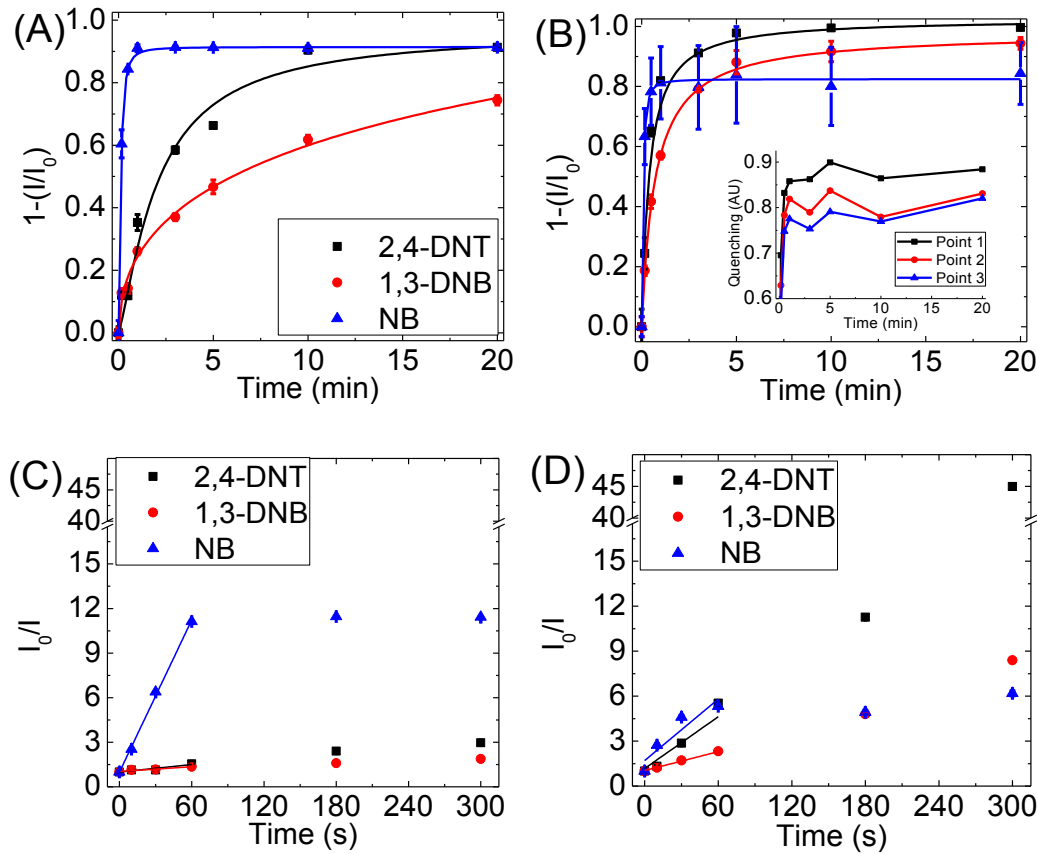


**Figure 4-5 (A & B)** Fluorescence quenching response to different nitroaromatic vapors of MEH-PPV thin films on (A)  $\text{SiO}_2$ -coated silicon and (B) silver plasmonic gratings; (C & D) Modified Stern-Volmer plots for (A) and (B), respectively (Note: Curves in A & B are guides to the eye. Curves in C & D represent linear fits to initial points for rate calculation).

**Table 4-1 Summary of Optical and Electrochemical Properties of Reactants and Reaction Rates**

	2,4,6-TNT	2,4-DNT	1,3-DNB	NB
$VP \text{ (mmHg)} [163]$	$8.02 \times 10^{-6}$	$1.47 \times 10^{-4}$	$9.00 \times 10^{-4}$	0.245
$VP_{rel}$	1	18	112	$3.05 \times 10^4$
$E_{red} \text{ (V)} [159]$	-0.7	-1.0	-0.9	-1.15
$\Delta G^\circ \text{ (eV)}$	-0.82	-0.52	-0.62	-0.37
$K_{sv,t} \text{ (Silica) (s}^{-1}\text{)}$	-	0.008	0.005	0.171
$K_{sv,t} \text{ (Silver) (s}^{-1}\text{)}$	-	0.030	-	-
$K_{sv,t} \text{ (Grating) (s}^{-1}\text{)}$	-	0.057	0.021	0.068

#### 4.4 Conclusions

Low-cost metallic plasmonic gratings and silica thin films were evaluated as means to improve the sensitivity and stability of conjugate polymer chemosensors for nitroaromatics. While the oxide deposition process reduced the initial intensity of the device by partial oxidation of the underlying polymer material, the fluorescence of the resultant films was preserved during storage in ambient air for several months. Metallic plasmonic gratings improved the initial intensity more than seven-fold with respect to films on an optimized SiO<sub>2</sub>-coated silicon. This enhancement permits two possible modes of sensor improvement: (1) the use of reduced excitation intensities to provide fluorescence similar to films on silica/glass and thus prolong the life of the device or (2) the use of similar excitation intensities to provide drastic improvements to signal-to-noise ratio and the sensitivity of the device. Microporosity in the silica layer allows these films to retain their rapid quenching response to nitroaromatic vapors, with thin capped films on gratings quenching more than 80% in 60 seconds, a rate more than 7 times faster than similar films on SiO<sub>2</sub>-coated silicon. More importantly, exposed films were able to recover fluorescence with time, allowing the potential for multiple use cycles and as dynamic sensors.

# **CHAPTER 5 CONCLUSIONS AND RECOMMENDATIONS FOR FUTURE WORK**

## **5.1 Conclusions**

Low-cost metallic plasmonic gratings and ultra-thin oxide ( $\text{SiO}_2$ ) capping layer were evaluated as means to improve the stability, signal, and sensitivity of fluorescent conjugated polymer (FCP) chemosensors. In Chapter 3, we found that fluorescence of the resultant capped, plasmonic-enhanced films was enhanced more than seven-fold, primarily by a process of surface plasmon-coupled emission. Furthermore, the enhanced fluorescent material was preserved from photo-oxidative damage by the semipermeable low-density  $\text{SiO}_2$  capping layer both during active use and storage in ambient air for several months. This layer screened out moisture and oxygen from penetrating into the polymer film by its high surface energy density, which attracts the moisture and effectively blocks the entrance to the infrequent, disconnected pores. Meanwhile, the same porosity in the capping layer allowed the MEH-PPV films to retain their rapid quenching response to nitroaromatic vapors, with thin capped films on gratings quenching at a rate more than 7 times faster than similar films on  $\text{SiO}_2$ -coated silicon due to competition between excited state electron diffusion and relaxation pathways.

Then, in Chapter 4, a few unique properties of the capped thin films were examined, including the fact that quenching occurs by a process of diffusion, first through the capping layer, then interweaving through the MEH-PPV film itself. This results in radially increasing quenching centers, which begin at nodes directly beneath the pores that do allow

access between ambient air and the polymer. The capped MEH-PPV thin films also exhibit different quenching speeds for different materials, as indicated by their time-dependent quenching rates, found by examining a variation on the Stern-Volmer plot looking at the ratio of fluorescence intensities over time for a steady-state diffusion of 2,4-DNT. The difference in rates is attributed to both the change in vapor pressure for different NA compounds as well as their diffusion through the MEH-PPV layer and energy-guided interaction (quenching rate itself) with MEH-PPV molecules.

Finally, these capped MEH-PPV films exposed to NA were able to recover the full initial fluorescence intensity with time. The speed with which the films recovered after removal from each vapor was also dependent on vapor pressure, with nitrobenzene recovering rapidly while 2,4-DNT recovers over the course of hours. This also has to do with the specific interaction, molecular size, and porosity of both MEH-PPV and capping layer films. The recovery itself allows for the films to be used in multiple use cycles with negligible effect to the quenching rate or intensity after previous exposures. These unique properties show great promise toward enhancement of FCP sensor systems for embedded sensors in real-world applications.

## 5.2 Future Direction

### 5.2.1 Surface Energy-Mediated Polymer Morphologies

As noted in Chapter 3, AFM imaging of the MEH-PPV thin films on SiO<sub>2</sub>-coated silicon and, to a lesser degree, plasmonic gratings revealed a complex, undulating MEH-PPV thin film morphology caused by the onset of surface energy-mediated spinodal dewetting from the pristine SiO<sub>2</sub> surface [111], a form of spinodal decomposition Film

instability arises at these growing undulations if the effective Hamaker constant is negative. Direct observation of this phenomenon requires that the thickness fluctuation, undulation growth rate, and Hamaker constant be such that AFM can be performed on the intermediate steps. While these steps were not able to be observed on MEH-PPV films on silica, the final result matches the characteristics of spinodal dewetting sufficiently to conclude it as such. The primary reason for MEH-PPV dewetting is due to a mismatch of surface energy density between the MEH-PPV ( $\gamma \approx 26 \text{ mJ/m}^2$  as measured on ITO) [142] and the freshly cleaned  $\text{SiO}_2$  surface ( $\gamma \approx 71\text{-}77 \text{ mJ/m}^2$ ) [113]. Significant improvements to polymer dissolution techniques were undertaken to reduce dewetting as much as possible, but some were unavoidable due to the use of chloroform as the solvent. Toluene, p-xylene, and other aromatic solvents may be used to alleviate some of the chemical pressures associated with particulate formation in a relatively poor solvent such as chloroform, but may lead to more orderly alignment through increased  $\pi\text{-}\pi$  interaction, which reduces the fluorescence efficiency of the material [143, 144]. Furthermore, “better” (i.e. more non-polar, aromatic) solvents would not address the underlying surface energy mismatch between MEH-PPV and  $\text{SiO}_2$ . Utilizing a non-polar self-assembled monolayer (SAM) such as octodecyltrichlorosilane (OTS) ( $\gamma \approx 20\text{-}25 \text{ mJ/m}^2$  [113]) may improve surface energy matching on  $\text{SiO}_2$ , but more care would need to be taken with regards to silver, especially given that increased distance from the surface as well as degradation and oxidation by silane and solvents reduce plasmonic coupling efficiency.

The film process used in this work was not modified to include OTS treatment since the capping layer effectively sandwiched the films and prevented further dewetting.

However, it is well-known that surface energy plays a role in organic semiconductor morphology, alignment, torsion, etc. all of which have effects on interactivity with nitroaromatics. Furthermore, certain morphological arrangements could affect the diffusion rate through the MEH-PPV layer by increasing or decreasing the space between molecules (i.e. porosity) due to steric hindrance and morphological disorder. It would be interesting to examine the changes in morphology, fluorescence, and NA reactivity that specific surface energy densities provide on same-thickness MEH-PPV thin films. For SiO<sub>2</sub>-coated silicon, various silanes with different active sites (COO<sup>-</sup>, NH<sub>2</sub>, SH, CH<sub>3</sub>, aryl ring, etc.) could be used to tune the surface energy density between hydrophilic and hydrophobic surfaces, which would affect how the films form on the surface, packing, dewetting (if any), and aggregation..

### 5.2.2 Molecularly Imprinted Fluorescent Conjugated Polymers

The focus of this work would to investigate and optimize material properties of a fluorescence-based conjugated polymer (FCP) sensor and integrate the optimized condition with plasmonic gratings for sensitive, selective detection of trace nitroaromatic (NA) vapors. The unique chemical and electrical properties of FCPs have been used to improve the sensitivity of a number of chem/bio sensor systems in recent years. Meanwhile, molecularly imprinted polymers (MIPs)—polymers designed to provide physical and chemical memory of a target template molecule—offer significant improvement to the selectivity of chemical sensors [9, 26, 50, 52, 92, 95, 97, 164, 165]. The chemical sensitivity of FCPs would be combined with the chemical selectivity of MIPs and optimized over a plasmonic grating substrate layer to enhance the signal provided by

the FCP MIP interaction with nitroaromatics. This work would leverage the experience and techniques developed in the course of previous projects on plasmonic-enhanced FCP-based sensors as well as molecular imprinting techniques developed in our labs to synthesize a powerful, sensitive, selective NA sensor. Molecular imprinting the FCPs would be investigated by spinning template-doped FCP thin films onto silicon and stabilized grating substrates with appropriate silanes (i.e. APTES) to encourage interaction, followed by annealing to physically “lock-in” the template. Rapid annealing at proper temperatures above the glass transition temperature of the FCP and below the decomposition temperatures of the FCP, APTES, and template should lead to FCP/APTES crystallization around the template molecules. Another option that would be investigated is solvent vapor annealing, which is advantageous in that it allows room-temperature film processing and may allow polymer reorganization around the template without loss of photoluminescence efficiency. Both vacuum and solvent extraction methods will be explored to optimize the imprinting process. Films will then be capped with a thin, protective oxide cap as has been done in the presented work or stabilized with a polymer additive [166] and exposed to various NA vapors and related interfering analytes to determine relative quenching rates.

### **5.3 Wider Implications of Research**

The goals and results of the plasmonic- (SPR)-enhanced conjugated polymer fluorescence-based chemosensor have major implications on the future of the field of portable fluorescence-based nitroaromatic sensors. Preventing photo-oxidation of conjugated polymers is significant enough, but capping the conjugated polymer film in

such a way that protection is afforded while the activity of the polymer is maintained is an important benchmark step toward the goal of achieving a free-standing, portable fluorescence sensor for NA vapors. Aside from polymer stability, this goal was hindered previously by a number of real-world constraints that do not appear readily from laboratory experiments but can be addressed through the use of our capped, SPR-amplified MEH-PPV device: power constraints on the excitation source and photodetectors, shelf life due to signal loss resulting from interaction with interfering analytes, and the ability to generate signals with high signal-to-noise ratio (SNR). While planar substrates provided no real benefit to signal-to-noise ratio, improvements to SNR can be facilitated through the intrinsic signal amplification provided by our SPR-based platform so that low-cost, low-power excitation sources and detection optics may be employed to read out the sensor responses while maintaining appropriate SNR to get actionable readings.

Also, in field deployment, it is necessary to recalibrate the device after a known exposure event. This platform in its current formulation allows the NA vapors to desorb freely after an exposure is complete, indicating that its reusability in the field is strong, but selectivity is relatively weak compared to MIPs in the presence of saturated vapors. However, further adaptation of the MIP technology to incorporate less caustic or aqueous-based precursor formulations may allow the use of MEH-PPV in such a device, which would impart selectivity and a level of permanency to the quenching behavior. This device would require template extraction after exposure or would be a one-use cartridge type device. Using metallic gratings produced by e-beam lithography would make this a

prohibitively expensive venture, but the micro-contact printing process allows the mass production of such devices less the cost of e-beam lithography.

# **APPENDIX A A COMPARATIVE EVALUATION OF MICROARRAY SLIDES AS SUBSTRATES FOR THE DEVELOPMENT OF PROTEASE ASSAY BIOSENSORS**

## **A-1 Introduction**

Arrayed biosensors are becoming popular diagnostic tools in a number of fields due to the high specificity and sensitivity of biomolecules to their target analytes [7, 73, 165]. DNA- and antibody-based microarrays are generally well-characterized examples of high-throughput biosensors used to detect proteome expression levels and the presence of biological contaminants from bulk slurry [167-171]. However, since immunoassays do not assess the activity of proteins, assays constituting a form of the protein's *in vivo* substrate have been developed which offer a more quantitative analysis of enzymes and toxins in a solution [172, 173]. Optimal function of such protease assays depends on the accessibility of the substrate to the enzyme active site, making directed protein immobilization on the assay platform a central focus of biosensor design [10, 174].

Most protein arrays produced today invoke the self-assembled monolayer (SAM) technique, which provides for orientation through careful selection of the chemical moieties used for protein binding [175, 176]. Substrates with a number of chemical functionalities have been developed such as aldehyde, epoxy, and N-hydroxysuccinimide esters [177]. More recently, high-surface area hydrogels and polymer matrices used originally only for adsorptive binding have been modified with amine-reactive groups to

provide covalent binding and increase the mean signal and signal-to-noise ratio, providing extremely sensitive assays for low-copy proteins [169, 178]. However, very few protease assay studies place the enzyme's substrate on the platform since the potential cross-reactivity of proteases limits the number of probes per slide [173].

The goal of this study was to evaluate commonly used microarray slides for their use as platforms in protease assay biosensors. We look at the detection of Botulinum Neurotoxin A (BoNTA), a high profile toxic protease that has come to prominence in recent years in light of the increased risk of bioterrorism, its ubiquity in nature, and ease of production [179-181]. Lack of a well-accepted means of rapid BoNTA detection has necessitated the continued development of biosensors [176, 182, 183]. Several groups have provided alternatives including enzyme-linked immunosorbent assay (ELISA) and mass spectrometry [184-186]. However, these technologies still require long incubation times and expensive equipment, while recent advances in fluorescence-based biosensors show their potential for detection of biological agents [183, 186, 187].

## A-2 Materials and Methods

### A-2-1 Slide Selection and Preparation

The potential use of different slide substrates for protease assay biosensors was evaluated by studying protein binding and stability characteristics of biotinylated SNAPtide-FITC, a fluorescently-labeled BoNTA protease substrate (SNAPtide-FITC, List Biological Laboratories, Inc., Campbell, CA) on Streptavidin-spotted slides. Unless otherwise noted, all bulk reagents were purchased from Sigma-Aldrich (St. Louis, MO). Nexterion slides AL<sup>®</sup> (aldehyde), E<sup>®</sup> (epoxy), H<sup>®</sup> (hydrogel), and P<sup>®</sup> (polymeric) were

purchased from Schott North America, Inc. (Elmsford, NY) and epoxysilane-treated slides (“Slide T”) were also made in-house. Briefly, plain glass slides were cleaned in piranha solution (3:1 H<sub>2</sub>SO<sub>4</sub>:H<sub>2</sub>O<sub>2</sub>) for 10 minutes, rinsed in fresh ddH<sub>2</sub>O (18.1 MΩ-cm), dried in clean air, and then heated to 100 °C for 1 hour to remove excess moisture. Cleaned slides were then incubated in 3% (v/v) 3-(glycidoxypropyl)-trimethoxysilane (GPTS) in toluene on a radial shaker for 30 minutes. GPTS-coated slides were then rinsed in fresh toluene and ethanol, blown dry, and cured at 150 °C for 30 minutes.

#### A-2-2 Protein Binding

All slides (AL, E, H, P, and T) were then scribed into 5 mm x 5 mm square elements and incubated with protein according to the manufacturer specifications with some modification. Each square was manually spotted with 0.1 µL 20 µg/mL Streptavidin in sodium-deficient HEPES buffer (20 mM, pH 7.2) in ambient air and then transferred to a preconditioned humidity chamber at 22°C and 90% relative humidity for 1 hour. After incubation, Slides AL®, E®, and T were washed in washing buffer (20 mM HEPES, pH 7.2, 0.1% (v/v) Tween-20) and Slides H® and P® in borate buffer (100 mM boric acid, 25 mM ethanolamine, 0.1% (v/v) Tween-20) with gentle shaking for 1 hour. Washing buffers were then decanted off and the slides were rinsed 3 x 5 minutes with plain HEPES buffer to remove remnant surfactant. After decanting the rinsing buffer, a 5 µL droplet of 20 µg/mL SNAPTide was placed on each slide and covered with a glass cover slip. Slides were then incubated for 1 hour in the dark at 22 °C, 90% RH before washing for 1 hour with washing buffer and rinsing again with plain HEPES to remove surfactant. Optimal spotting and washing conditions were determined by spotting 0.2 mg/mL Streptavidin and

varying both SNAPtide and surfactant concentrations from 5-200 µg/mL and 0.01-1.0% (v/v) in incubation and borate/wash buffers, respectively. Prior to assays, measurements, or storage, individual elements were separated by breaking along the scribed lines, providing single-spot square sensing elements. Fluorescence measurements were taken on an Olympus BX51W1 fluorescence microscope using an USB4000 spectrometer (Ocean Optics, Inc., Dunedin, FL) and OPT101 photodiode (Texas Instruments). Data were analyzed using OriginPro 8 (OriginLab Corporation, Northampton, MA).

#### A-2-3 Long-term Stability

SNAPtide-labeled slides were stored at 37 °C for 2 hours in buffer containing HEPES with 0.5% (v/v) glycerol, 0.05% (v/v) PVP, or 0.5% (v/v) trehalose. After taking fluorescence measurements to determine the most protective conditions, more slides were made and stored in either HEPES or additive-modified HEPES for up to 1 month in the dark at 4 °C with measurements taken periodically. All slides were acclimated to room temperature just prior to measurements.

#### A-2-4 Protease Assay

BoNTA light chain (List Biological Laboratories, Inc.) was diluted from 400 nM aliquots into 200 µL working concentrations of 1, 2, 3, 4, or 5 nM in microcentrifuge tubes with reaction buffer (20 mM HEPES pH 7.2, 1.25 mM DTT, 0.3 mM ZnCl<sub>2</sub>). After taking initial fluorescence measurements, chips were distributed into each solution plus a toxin-negative control and incubated in dark at 37 °C for 2 hours. Slides were briefly rinsed in fresh HEPES and measured again to obtain the change in fluorescence.

## A-3 Results

### A-3-1 Slide Selection and Protein Binding

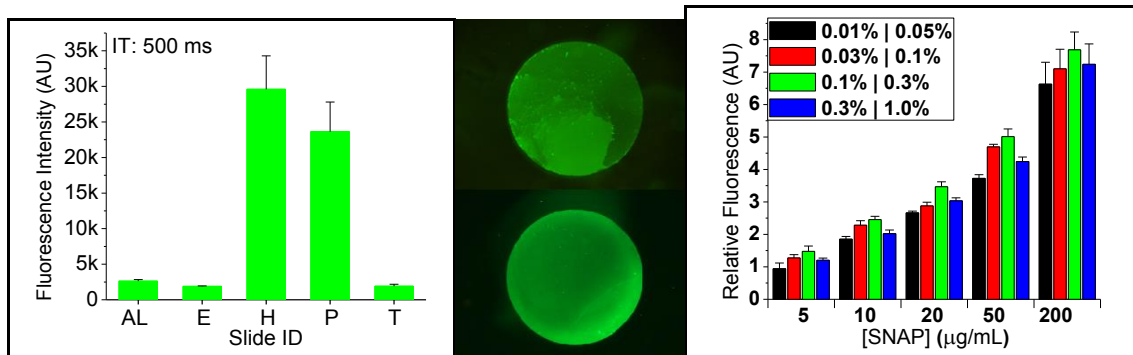


**Figure A-1 (A)** SNAP fluorescence intensities on different slide substrates (AL - aldehyde, E - epoxysilane, H - hydrogel, P - polymer, T - GPTS) (n=5); Optical micrographs of spots on Slide P without (B) and with (C) glycerol and humidity chamber; (D) Effect of increasing both SNAP and wash buffer surfactant concentrations on mean fluorescence intensity (% indicate concentration of surfactant in wash buffers before and after SNAP incubation) (n=10, FITC fluorescence intensity expressed as mean  $\pm$  SE).

SNAPtide-FITC is a synthetic peptide containing the native cleavage site for Botulinum Neurotoxin Type A. Cleavage of the substrate by the toxin releases the fluorophore and fluorescence is reduced. The decrease in fluorescence intensity is directly proportional to the amount of cleavage that has occurred and thus allows for accurate measurement of Botulinum toxin enzymatic activity. A comparison of SNAPtide fluorescence intensities on each of the slides tested before cleavage is shown in **Figure A-1A**. Slide H<sup>®</sup> was found to have the highest average intensity with  $29,592 \pm 4694$  counts (n=5) followed by Slide P<sup>®</sup> with  $23,651 \pm 4158$  counts (n=5). Meanwhile, Slides AL, E, and T registered roughly 10 times less fluorescence than Slide P<sup>®</sup>. The relatively large error bar for Slides H<sup>®</sup> and P<sup>®</sup> was due to drying artifacts during initial experiments as shown in **Figure A-1B**. Since these slides were to be used for protease assay under less than ideal conditions such as prolonged shaking and increased temperatures, the slides were

left on a radial shaker in HEPES buffer for a few hours at ~30 rpm, resulting in a 40% loss of signal for Slide H® and 20% loss for Slide P®. Since the flat substrates already had low signal-to-noise ratio and the hydrogel slides were relatively unstable, Slide P® was chosen for further experiments due to its optimal combination of signal intensity and stability.

However, buffer evaporation led to drying spot artifacts which limited their use. To overcome this problem, we tested different buffer additives (**Figure A-1B**). We found that uniform spot morphology was achievable through the combined use of buffer additives (Glycerol and PVP) and high humidity during incubation provided by the preconditioned humidity chamber (**Figure A-1B**). Both glycerol and PVP were tested as print additives, initially included at 0.5% (v/v) and 0.05% (v/v), respectively, which resulted in increased mean fluorescence intensity compared to unmodified buffer (see **Figure A-1B, Inset**). However, increasing PVP content beyond 0.1% prevented binding of Streptavidin (data not shown). The intra-spot coefficient of variation (defined as  $\text{CoV} = \sigma/\mu$ ) was also improved, going from 20.5% in unmodified buffer to 13.4% in PVP and 9.8% in glycerol. A typical spot achieved with glycerol additive is shown in Figure 1C.

The effects on chip fluorescence of increasing concentrations of both SNAPtide and surfactant were used to test the level of nonspecific binding in the 3D polymer slide (**Figure A-1C**). The expected logarithmic relationship between SNAPtide concentration and fluorescence was observed, indicating saturation of the basement Streptavidin layer. Increasing the surfactant fraction in the washing buffers also caused dose-dependent changes in fluorescence. Between 0.01-0.3% (v/v) Tween-20, fluorescence increased

uniformly across the range of SNAPtide concentrations used. Meanwhile, higher surfactant loading led to a significant decrease in fluorescence (blue column).

Finally, the effects of the buffer additives on stability of protein binding at elevated temperature conditions were tested. Of these, PVP offered the only protection to freshly-prepared chips (**Figure A-2A**), averaging 13% higher fluorescence than unmodified buffer after 2 hours. This protection was significant enough to warrant inclusion in both storage buffer and reaction buffers during actual assays. **Figure A-2B** shows the results of long-term storage on the mean fluorescence intensity. Black and red columns were spotted with glycerol in the spotting buffer and blue and teal with PVP. Their initial intensities, represented by red and blue for glycerol and PVP, respectively, are shown in the inset in comparison to unmodified buffer (black). Over the course of 1 month, PVP again provided ~15% more stable fluorescence than unmodified buffer in the case of glycerol-spotted slides.

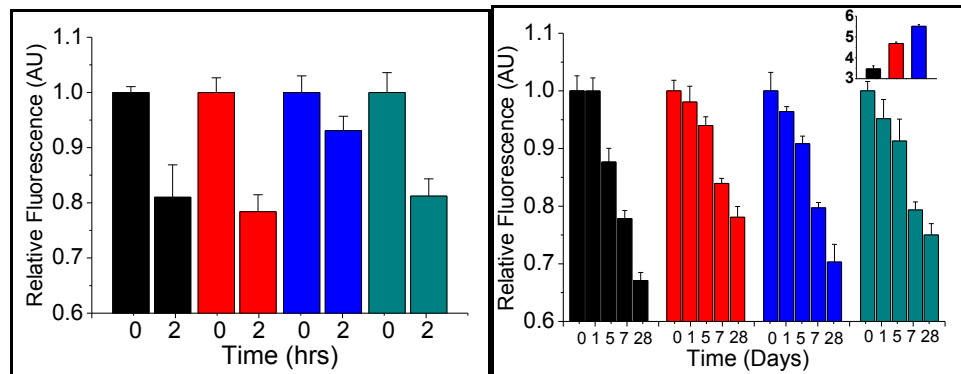


**Figure A-2 (A)** Effect of buffer additives on fluorescence stability at 37 °C (G = 0.5% Glycerol, P = 0.05% PVP, T = 0.5% Trehalose); **(B)** Effect of buffer additives on long-term binding stability at 4 °C (spotting/storage additives: black = Glycerol/HEPES, red = Glycerol/PVP, green = PVP/HEPES, blue = PVP/PVP), (Inset) Initial intensity of chips spotted with unmodified HEPES (black), HEPES + Glycerol (red), and HEPES + PVP (blue).

### A-3-2 Protease Assay

**Figure A-3A** below shows a schematic of the protease assay. Under assay conditions, SNAPtide is targeted and cleaved by BoNTA light chain, removing the fluorescent tag and leading to a drop in fluorescent signal intensity. A 2 hour assay at 37 °C provided a limit of detection around 3 nM, on the same order as the lethal dose (**Figure A-3B**). A linear correlation ( $R^2 = 0.92$ ) between protease concentration and fluorescence was seen, especially between 2-5 nM ( $R^2 > 0.99$ ). Increasing the assay time led to significant signal loss from the control sample, masking some of the activity of the toxin. However, as low as 1 nM could be distinguished from the control after 4 hours of assay time.

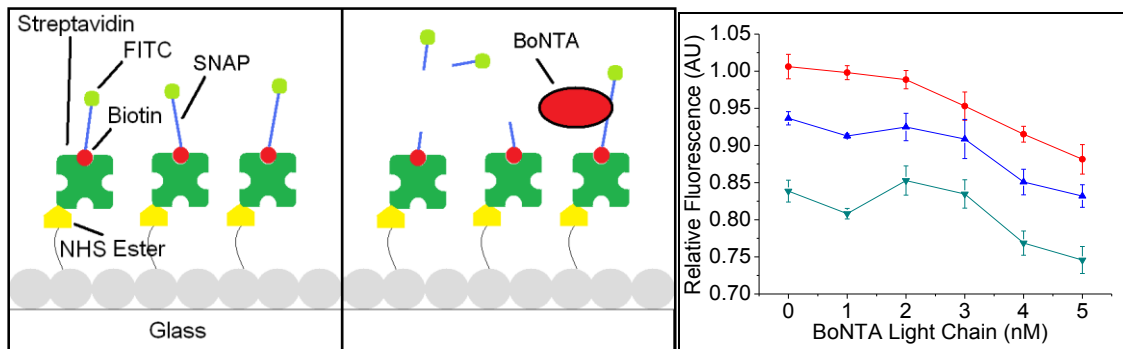


**Figure A-3 (A) Assay schematic and (B) Results of 2-hr assay of BoNTA light chain (● = 2 hrs, ▲ = 4 hrs, ▼ = 12 hrs)**

### A-4 Discussion

Amine-reactive coated glass slides are used as platforms for a number of diagnostic DNA and antibody microarrays. However, very few protease assays have been made using these slides due to their primary use as high-throughput qualitative microarrays and their potential as discrete sensing elements has so far not been explored [172]. Nexterion Slide

P®, with a surface coating of proprietary polymer matrix activated with N-hydroxysuccinimide (NHS) esters, was found to have good signal-to-noise ratio in comparison to flat glass and was more stable than hydrogel-coated slides. Surface amines such as those from lysine residues of Streptavidin bind readily to the slides, onto which at least one, perhaps multiple biotinylated SNAPtide molecules can then attach with very high affinity [188]. Binding a primary or basement layer of Streptavidin allows orientation of the fluorescently-labeled SNAPtide substrates into the solution and also prevents amines on the SNAPtide peptide from linking covalently to the slide. This ensures maximal access to the cleavage sites during assay and that the cleaved portion can be separated from the film.

Drying artifacts due to evaporation of the printing buffer result from inhomogeneous protein distribution throughout the incubation period. These effects have been addressed using print additives with higher vapor pressure than water, which are thought to replace water molecules around the protein as they evaporate [168]. Glycerol and PVP were both tested as print additives and while PVP led to higher mean fluorescence, glycerol was found to have the greatest improvement to spot morphology, reducing coefficient of variation by half compared to unmodified buffer. Increasing PVP concentration beyond a minimal per volume concentration limited the ability of Streptavidin to come in contact with the polymer surface, indicating its effectiveness as a blocking agent, but limiting its use as a spotting buffer additive [189].

Stability of protein bound to the slide is an important aspect of any sensor, especially since cleavage of the substrate peptide leads to a reduction in fluorescence. Both

Slide H® and P® had higher signal-to-noise than flat glass substrates, but suffered from instability in initial experiments. The higher signal loss from Slide H was attributed to the tendency of hydrogels to swell in the presence of aqueous buffers, which can lead to film degradation and leaching of material embedded deep in the hydrogel matrix [190]. The possibility that nonspecific binding was responsible was addressed by testing the effects of increasing SNAPtide and surfactant concentrations on the measured fluorescent signal [71]. The increasing signal with increasing surfactant fraction suggests the peptide was densely packed leading to self-quenching of the FITC fluorophores [28].

Assay of the toxin generally requires increased temperatures that simulate the *in vivo* conditions under which the toxin performs naturally [183]. Under assay conditions, the toxin should cleave the SNAPtide peptide, releasing the fluorescent label and leading to reduced on-chip fluorescence. However, a side-effect of increased temperature in this case was reduced protein stability to the film. Use of a FRET pair in future designs may allow for increased sensitivity since the ratiometric design is less susceptible to these artifacts. However, this detection scheme is still important as it does not require pull-down or concentration of the toxin from its bulk slurry prior to assay. This can reduce preparatory time prior to protease assay, which has been demonstrated effectively in qualitative immunoassays of biological agents [170].

In summary, we have examined key parameters in the application of recently developed microarray slides for protease assay biosensors. Nexterion Slide P® offers a combination of optimal intensity and stability in comparison with other available slides making it more amenable to sensor applications. The inclusion of buffer additives glycerol

and PVP were used to improve spot morphology during binding and extend the useful duty life for protease assays requiring elevated temperatures without affecting protease activity. Detection of BoNTA light chain was accomplished in the sub-lethal nM range within 2 hours. Future improvements should provide more sensitive detection and this facile detection scheme has the potential for use in a portable sensor system.

## **REFERENCES**

- [1] A. H. Maslow, "A theory of human motivation," *Psychological Review*, vol. 50, pp. 370-396, 1943.
- [2] S. G. Winter, "Specialised Perception, Selection, and Strategic Surprise: Learning from the Moths and Bees," *Long Range Planning*, vol. 37, pp. 163-169, 4// 2004.
- [3] C. Nylander, "Chemical and biological sensors," *Journal of Physics E: Scientific Instruments*, vol. 18, p. 736, 1985.
- [4] S. S. Arnon, R. Schechter, T. V. Inglesby, and et al., "Botulinum toxin as a biological weapon: Medical and public health management," *JAMA*, vol. 285, pp. 1059-1070, 2001.
- [5] J. Homola, *Surface plasmon resonance based sensors* vol. 4: Springer, 2006.
- [6] S. J. Toal and W. C. Trogler, "Polymer sensors for nitroaromatic explosives detection," *Journal of Materials Chemistry*, vol. 16, pp. 2871-2883, 2006.
- [7] M. K. Ram and V. R. Bhethanabotla, *Sensors for chemical and biological applications*. Boca Raton, Fl.: CRC Press, 2006.
- [8] S. Singh, "Sensors—An effective approach for the detection of explosives," *Journal of Hazardous Materials*, vol. 144, pp. 15-28, 2007.
- [9] C. R. Stringer, S. Gangopadhyay, and S. A. Grant, *Fluorescent imprinted polymers for detection of explosive nitro-aromatic compounds* vol. 7303. Bellingham, WA, ETATS-UNIS: Society of Photo-Optical Instrumentation Engineers, 2009.
- [10] E. Pazos, O. Vazquez, J. L. Mascarenas, and M. Eugenio Vazquez, "Peptide-based fluorescent biosensors," *Chemical Society Reviews*, vol. 38, pp. 3348-3359, 2009.

- [11] J.-S. Yang and T. M. Swager, "Fluorescent Porous Polymer Films as TNT Chemosensors: Electronic and Structural Effects," *Journal of the American Chemical Society*, vol. 120, pp. 11864-11873, 1998/11/01 1998.
- [12] D. T. McQuade, A. E. Pullen, and T. M. Swager, "Conjugated Polymer-Based Chemical Sensors," *Chemical Reviews*, vol. 100, pp. 2537-2574, 2000/07/01 2000.
- [13] C.-P. Chang, C.-Y. Chao, J. H. Huang, A.-K. Li, C.-S. Hsu, M.-S. Lin, *et al.*, "Fluorescent conjugated polymer films as TNT chemosensors," *Synthetic Metals*, vol. 144, pp. 297-301, 2004.
- [14] R. G. Smith, N. D'Souza, and S. Nicklin, "A review of biosensors and biologically-inspired systems for explosives detection," *Analyst*, vol. 133, pp. 571-584, 2008.
- [15] P. G. Del Rosso, M. F. Almassio, G. R. Palomar, and R. O. Garay, "Nitroaromatic compounds sensing. Synthesis, photophysical characterization and fluorescence quenching of a new amorphous segmented conjugated polymer with diphenylfluorene chromophores," *Sensors and Actuators B: Chemical*, vol. 160, pp. 524-532, 2011.
- [16] Y. Salinas, R. Martinez-Manez, M. D. Marcos, F. Sancenon, A. M. Costero, M. Parra, *et al.*, "Optical chemosensors and reagents to detect explosives," *Chemical Society Reviews*, vol. 41, pp. 1261-1296, 2012.
- [17] H. Li, J. Wang, Z. Pan, L. Cui, L. Xu, R. Wang, *et al.*, "Amplifying fluorescence sensing based on inverse opal photonic crystal toward trace TNT detection," *Journal of Materials Chemistry*, vol. 21, 2011.
- [18] Q. Zhou and T. M. Swager, "Method for enhancing the sensitivity of fluorescent chemosensors: energy migration in conjugated polymers," *Journal of the American Chemical Society*, vol. 117, pp. 7017-7018, 1995/07/01 1995.
- [19] H. Zheng, B. Ramalingam, V. Korampally, and S. Gangopadhyay, "Large sensitivity enhancement in semiconducting organic field effect transistor sensors through incorporation of ultra-fine platinum nanoparticles," *Applied Physics Letters*, vol. 103, pp. -, 2013.

- [20] S. Bok, V. Korampally, C. M. Darr, W. R. Folk, L. Polo-Parada, K. Gangopadhyay, *et al.*, "Femtogram-level detection of Clostridium botulinum neurotoxin type A by sandwich immunoassay using nanoporous substrate and ultra-bright fluorescent suprananoparticles," *Biosensors and Bioelectronics*, vol. 41, pp. 409-416, 3/15/2013.
- [21] J. Yinon, "Field detection and monitoring of explosives," *TrAC Trends in Analytical Chemistry*, vol. 21, pp. 292-301, 4// 2002.
- [22] C. T. J. Alkemade, W. Snelleman, G. D. Boutilier, B. D. Pollard, J. D. Winefordner, T. L. Chester, *et al.*, "A review and tutorial discussion of noise and signal-to-noise ratios in analytical spectrometry—I. Fundamental principles of signal-to-noise ratios," *Spectrochimica Acta Part B: Atomic Spectroscopy*, vol. 33, pp. 383-399, // 1978.
- [23] G. Adamo, Agro, x, D., S. Stivala, A. Parisi, *et al.*, "Signal to Noise Ratio of silicon photomultipliers measured in the continuous wave regime," in *Photonics Conference, 2014 Third Mediterranean*, 2014, pp. 1-3.
- [24] B. Sangho, P. K. Dasgupta, V. Korampally, L. Polo-Parada, W. Folk, K. Gangopadhyay, *et al.*, "Novel nanostructured platform and nanoparticles for sensitive detection of biological materials," in *Sensors, 2010 IEEE*, 2010, pp. 450-453.
- [25] B. Sangho, K. Venumadhav, P.-P. Luis, M. Vamsi, A. B. Gary, G. Keshab, *et al.*, "Confeito-like assembly of organosilicate-caged fluorophores: ultrabright suprananoparticles for fluorescence imaging," *Nanotechnology*, vol. 23, p. 175601, 2012.
- [26] J. Li, C. E. Kendig, and E. E. Nesterov, "Chemosensory Performance of Molecularly Imprinted Fluorescent Conjugated Polymer Materials," *Journal of the American Chemical Society*, vol. 129, pp. 15911-15918, 2007/12/01 2007.
- [27] R. Bogue, "Quantum dots: a bright future for photonic nanosensors," *Sensor Review*, vol. 30, pp. 279-284, 2010.
- [28] J. R. Lakowicz, *Principles of Fluorescence Spectroscopy*, 3 ed. New York: Springer Science+Business Media, LLC, 2003.

- [29] B. Valeur and M. N. Berberan-Santos, *Molecular fluorescence: principles and applications*: John Wiley & Sons, 2012.
- [30] M. Liu, Z. Lin, and J.-M. Lin, "A review on applications of chemiluminescence detection in food analysis," *Analytica Chimica Acta*, vol. 670, pp. 1-10, 6/18/ 2010.
- [31] M. Seidel and R. Niessner, "Chemiluminescence microarrays in analytical chemistry: a critical review," *Analytical and Bioanalytical Chemistry*, vol. 406, pp. 5589-5612, 2014/09/01 2014.
- [32] H. Becker, S. E. Burns, and R. H. Friend, "Effect of metal films on the photoluminescence and electroluminescence of conjugated polymers," *Physical Review B*, vol. 56, pp. 1893-1905, 1997.
- [33] A. Kraft, A. C. Grimsdale, and A. B. Holmes, "Electroluminescent Conjugated Polymers—Seeing Polymers in a New Light," *Angewandte Chemie International Edition*, vol. 37, pp. 402-428, 1998.
- [34] S.-A. Chen, T.-H. Jen, and H.-H. Lu, "A Review on the Emitting Species in Conjugated Polymers for Photo- and Electro-luminescence," *Journal of the Chinese Chemical Society*, vol. 57, pp. 439-458, 2010.
- [35] Y. Zhang, Y. Zelinsky, and V. May, "Plasmon-enhanced electroluminescence of a single molecule: A theoretical study," *Physical Review B*, vol. 88, p. 155426, 10/18/ 2013.
- [36] N. H. A. Rahman, A. Manut, and M. Rusop, "Review on Electroluminescence Behaviour of Organic Light Emitting Diode," *Advanced Materials Research*, vol. 832, pp. 455-459, 2014.
- [37] B. P. Chandra and A. S. Rathore, "Classification of Mechanoluminescence," *Crystal Research and Technology*, vol. 30, pp. 885-896, 1995.
- [38] M. Kumar, G. Chourasiya, R. K. Kher, B. C. Bhatt, and C. M. Sunta, "Theoretical investigations of localized, semi-localized and unified models of thermally stimulated luminescence: a review," *Indian Journal of Physics*, vol. 85, pp. 527-550, 2011/04/01 2011.

- [39] H.-J. Park, D. Vak, Y.-Y. Noh, B. Lim, and D.-Y. Kim, "Surface plasmon enhanced photoluminescence of conjugated polymers," *Applied Physics Letters*, vol. 90, pp. 161107-3, 2007.
- [40] T. S. Kuntzleman, A. E. Comfort, and B. W. Baldwin, "Glowmatography," *Journal of Chemical Education*, vol. 86, p. 64, 2009/01/01 2009.
- [41] J. Engebrecht, K. Nealson, and M. Silverman, "Bacterial bioluminescence: Isolation and genetic analysis of functions from *Vibrio fischeri*," *Cell*, vol. 32, pp. 773-781, 3// 1983.
- [42] E. A. Meighen, "Molecular biology of bacterial bioluminescence," *Microbiological Reviews*, vol. 55, pp. 123-142, March 1, 1991 1991.
- [43] E. H. White, E. Rapaport, H. H. Seliger, and T. A. Hopkins, "The chemi- and bioluminescence of firefly luciferin: An efficient chemical production of electronically excited states," *Bioorganic Chemistry*, vol. 1, pp. 92-122, 9// 1971.
- [44] J. R. Lakowicz and B. R. Masters, "Principles of Fluorescence Spectroscopy, Third Edition," *Journal of Biomedical Optics*, vol. 13, pp. 029901-2, 2008.
- [45] J. R. Lakowicz, *Principles of Fluorescence Spectroscopy*, Third Edition ed.: Springer, 2006.
- [46] R. Yuste, "Fluorescence microscopy today," *Nat Meth*, vol. 2, pp. 902-904, 12//print 2005.
- [47] K. Hara, T. Sato, R. Katoh, A. Furube, Y. Ohga, A. Shinpo, *et al.*, "Molecular Design of Coumarin Dyes for Efficient Dye-Sensitized Solar Cells," *The Journal of Physical Chemistry B*, vol. 107, pp. 597-606, 2003/01/01 2002.
- [48] J. Liu, Z. Diwu, W.-Y. Leung, Y. Lu, B. Patch, and R. P. Haugland, "Rational design and synthesis of a novel class of highly fluorescent rhodamine dyes that have strong absorption at long wavelengths," *Tetrahedron Letters*, vol. 44, pp. 4355-4359, 6/2/ 2003.

- [49] Q. A. Best, R. Xu, M. E. McCarroll, L. Wang, and D. J. Dyer, "Design and Investigation of a Series of Rhodamine-Based Fluorescent Probes for Optical Measurements of pH," *Organic Letters*, vol. 12, pp. 3219-3221, 2010/07/16 2010.
- [50] R. C. Stringer, S. Gangopadhyay, and S. A. Grant, "Detection of Nitroaromatic Explosives Using a Fluorescent-Labeled Imprinted Polymer," *Analytical Chemistry*, vol. 82, pp. 4015-4019, 2010/05/15 2010.
- [51] Z. Wang, Z. Y. Wang, J. Ma, W. J. Bock, and D. Ma, "Effect of film thickness, blending and undercoating on optical detection of nitroaromatics using fluorescent polymer films," *Polymer*, vol. 51, pp. 842-847, 2010.
- [52] R. C. Stringer, S. Gangopadhyay, and S. A. Grant, "Comparison of molecular imprinted particles prepared using precipitation polymerization in water and chloroform for fluorescent detection of nitroaromatics," *Analytica Chimica Acta*, vol. 703, pp. 239-244, 2011.
- [53] C. Geddes and J. Lakowicz, "Editorial: Metal-Enhanced Fluorescence," *Journal of Fluorescence*, vol. 12, pp. 121-129, 2002/06/01 2002.
- [54] J. R. Lakowicz, *Radiative decay engineering 5: metal-enhanced fluorescence and plasmon emission* vol. 337. Kidlington, ROYAUME-UNI: Elsevier, 2005.
- [55] K. Ray, R. Badugu, and J. R. Lakowicz, "Metal-Enhanced Fluorescence from CdTe Nanocrystals: A Single-Molecule Fluorescence Study," *Journal of the American Chemical Society*, vol. 128, pp. 8998-8999, 2006/07/01 2006.
- [56] V. N. Pustovit and T. V. Shahbazyan, "Resonance energy transfer near metal nanostructures mediated by surface plasmons," *Physical Review B*, vol. 83, p. 085427, 2011.
- [57] J. Malicka, I. Gryczynski, J. Kusba, Y. Shen, and J. R. Lakowicz, "Effects of metallic silver particles on resonance energy transfer in labeled bovine serum albumin," *Biochemical and Biophysical Research Communications*, vol. 294, pp. 886-892, 2002.
- [58] J. Lakowicz, J. Kuśba, Y. Shen, J. Malicka, S. D'Auria, Z. Gryczynski, *et al.*, "Effects of Metallic Silver Particles on Resonance Energy Transfer Between

- Fluorophores Bound to DNA," *Journal of Fluorescence*, vol. 13, pp. 69-77, 2003/01/01 2003.
- [59] M. Lunz, X. Zhang, V. A. Gerard, Y. K. Gun'ko, V. Lesnyak, N. Gaponik, *et al.*, "Effect of Metal Nanoparticle Concentration on Localized Surface Plasmon Mediated Förster Resonant Energy Transfer," *The Journal of Physical Chemistry C*, vol. 116, pp. 26529-26534, 2012/12/20 2012.
- [60] H. Aouani, O. Mahboub, N. Bonod, E. s. Devaux, E. Popov, H. Rigneault, *et al.*, "Bright Unidirectional Fluorescence Emission of Molecules in a Nanoaperture with Plasmonic Corrugations," *Nano Letters*, vol. 11, pp. 637-644, 2011/02/09 2011.
- [61] X. Cui, K. Tawa, H. Hori, and J. Nishii, "Tailored Plasmonic Gratings for Enhanced Fluorescence Detection and Microscopic Imaging," *Advanced Functional Materials*, vol. 20, pp. 546-553, 2010.
- [62] Y.-J. Hung, I. I. Smolyaninov, C. C. Davis, and H.-C. Wu, "Fluorescence enhancement by surface gratings," *Opt. Express*, vol. 14, pp. 10825-10830, 2006.
- [63] H. Szmacinski, K. Ray, and J. R. Lakowicz, "Effect of plasmonic nanostructures and nanofilms on fluorescence resonance energy transfer," *Journal of Biophotonics*, vol. 2, pp. 243-252, 2009.
- [64] C. R. Yonzon, E. Jeoung, S. Zou, G. C. Schatz, M. Mrksich, and R. P. Van Duyne, "A Comparative Analysis of Localized and Propagating Surface Plasmon Resonance Sensors: The Binding of Concanavalin A to a Monosaccharide Functionalized Self-Assembled Monolayer," *Journal of the American Chemical Society*, vol. 126, pp. 12669-12676, 2004/10/01 2004.
- [65] K. Bhatnagar, A. Pathak, D. Menke, P. V. Cornish, K. Ganapadhyay, V. Korampally, *et al.*, "Fluorescence enhancement from nanogap embedded plasmonic gratings by a novel fabrication technique with HD-DVD," *Nanotechnology*, vol. 23, p. 495201, 2012.
- [66] E. Kretschmann and H. Raether, "Radiative decay of non radiative surface plasmons excited by light (Surface plasma waves excitation by light and decay into photons applied to nonradiative modes)," *ZEITSCHRIFT FUER NATURFORSCHUNG, TEIL A*, vol. 23A, p. 2135, 1968.

- [67] A. Otto, "Excitation of nonradiative surface plasma waves in silver by the method of frustrated total reflection," *Zeitschrift für Physik*, vol. 216, pp. 398-410, 1968.
- [68] H. Raether, *Surface plasmons on smooth and rough surfaces and on gratings*. Berlin; New York: Springer-Verlag, 1988.
- [69] G. A. Burdick, "Energy Band Structure of Copper," *Physical Review*, vol. 129, pp. 138-150, 01/01/ 1963.
- [70] J. M. Pitarke, V. M. Silkin, E. V. Chulkov, and P. M. Echenique, "Theory of surface plasmons and surface-plasmon polaritons," *Reports on Progress in Physics*, vol. 70, p. 1, 2007.
- [71] R. A. Williams and H. W. Blanch, "Covalent immobilization of protein monolayers for biosensor applications," *Biosensors and Bioelectronics*, vol. 9, pp. 159-167, 1994.
- [72] M. Bras, V. Dugas, F. Bessueille, J. P. Cloarec, J. R. Martin, M. Cabrera, *et al.*, "Optimisation of a silicon/silicon dioxide substrate for a fluorescence DNA microarray," *Biosensors and Bioelectronics*, vol. 20, pp. 797-806, 2004.
- [73] J. E. Dover, G. M. Hwang, E. H. Mullen, B. C. Prorok, and S.-J. Suh, "Recent advances in peptide probe-based biosensors for detection of infectious agents," *Journal of Microbiological Methods*, vol. 78, pp. 10-19, 2009.
- [74] C. M. Darr, J. Castorena, V. Korampally, S. Gangopadhyay, and L. Polo-Parada, "A comparative evaluation of microarray slides as substrates for the development of protease assay biosensors," *Experimental and Molecular Pathology*, vol. 91, pp. 714-717, 12// 2011.
- [75] B. C. Harris, V. Korampally, C. Weilbaecher, L. Polo-Parada, S. Grant, and S. Gangopadhyay, "Protease biosensing on novel high surface area organosilicate nanoporous films," *Sensors and Actuators B: Chemical*, vol. 176, pp. 351-359, 1// 2013.
- [76] T. Förster, "Zwischenmolekulare energiewanderung und fluoreszenz," *Annalen der physik*, vol. 437, pp. 55-75, 1948.

- [77] O. V. Stepanenko, V. V. Verkhusha, I. M. Kuznetsova, V. N. Uversky, and K. K. Turoverov, "Fluorescent Proteins as Biomarkers and Biosensors: Throwing Color Lights on Molecular and Cellular Processes," *Current protein & peptide science*, vol. 9, pp. 338-369, 2008.
- [78] J. Zhang, Y. Fu, M. H. Chowdhury, and J. R. Lakowicz, "Enhanced Förster Resonance Energy Transfer on Single Metal Particle. 2. Dependence on Donor–Acceptor Separation Distance, Particle Size, and Distance from Metal Surface," *The Journal of Physical Chemistry C*, vol. 111, pp. 11784-11792, 2007/08/01 2007.
- [79] L. Zhao, T. Ming, L. Shao, H. Chen, and J. Wang, "Plasmon-Controlled Förster Resonance Energy Transfer," *The Journal of Physical Chemistry C*, vol. 116, pp. 8287-8296, 2012/04/12 2012.
- [80] C. S. Yun, A. Javier, T. Jennings, M. Fisher, S. Hira, S. Peterson, *et al.*, "Nanometal Surface Energy Transfer in Optical Rulers, Breaking the FRET Barrier," *Journal of the American Chemical Society*, vol. 127, pp. 3115-3119, 2005/03/01 2005.
- [81] T. Miyakawa and D. Dexter, "Phonon sidebands, multiphonon relaxation of excited states, and phonon-assisted energy transfer between ions in solids," *Physical Review B*, vol. 1, p. 2961, 1970.
- [82] F. Hirayama, "Intramolecular excimer formation. I. Diphenyl and triphenyl alkanes," *The Journal of Chemical Physics*, vol. 42, pp. 3163-3171, 1965.
- [83] E. A. Chandross and C. J. Dempster, "Intramolecular excimer formation and fluorescence quenching in dinaphthylalkanes," *Journal of the American Chemical Society*, vol. 92, pp. 3586-3593, 1970.
- [84] J. R. Lakowicz and G. Weber, "Quenching of fluorescence by oxygen. Probe for structural fluctuations in macromolecules," *Biochemistry*, vol. 12, pp. 4161-4170, 1973.
- [85] M. R. Eftink and C. A. Ghiron, "Fluorescence quenching studies with proteins," *Analytical biochemistry*, vol. 114, pp. 199-227, 1981.

- [86] T. L. Jennings, M. P. Singh, and G. F. Strouse, "Fluorescent Lifetime Quenching near  $d = 1.5$  nm Gold Nanoparticles: Probing NSET Validity," *Journal of the American Chemical Society*, vol. 128, pp. 5462-5467, 2006/04/01 2006.
- [87] R. R. Chance, A. Prock, and R. Silbey, "Molecular Fluorescence and Energy Transfer Near Interfaces," in *Advances in Chemical Physics*, ed: John Wiley & Sons, Inc., 2007, pp. 1-65.
- [88] A. K. Dwivedy, D. B. Parihar, S. P. Sharma, and K. K. Verma, "Charge-transfer complexes of 2,4,6-trinitrotoluene and m-dinitrobenzene with some amines," *Journal of Chromatography A*, vol. 29, pp. 120-125, 1967.
- [89] Q. Fang, J. Geng, B. Liu, D. Gao, F. Li, Z. Wang, *et al.*, "Inverted Opal Fluorescent Film Chemosensor for the Detection of Explosive Nitroaromatic Vapors through Fluorescence Resonance Energy Transfer," *Chemistry – A European Journal*, vol. 15, pp. 11507-11514, 2009.
- [90] K. Sablok, V. Bhalla, P. Sharma, R. Kaushal, S. Chaudhary, and C. R. Suri, "Amine functionalized graphene oxide/CNT nanocomposite for ultrasensitive electrochemical detection of trinitrotoluene," *Journal of Hazardous Materials*, vol. 248–249, pp. 322-328, 2013.
- [91] T.-H. Tran-Thi, R. Dagnelie, S. Crunaire, and L. Nicole, "Optical chemical sensors based on hybrid organic-inorganic sol-gel nanoreactors," *Chemical Society Reviews*, vol. 40, pp. 621-639, 2011.
- [92] C. Xie, B. Liu, Z. Wang, D. Gao, G. Guan, and Z. Zhang, "Molecular Imprinting at Walls of Silica Nanotubes for TNT Recognition," *Analytical Chemistry*, vol. 80, pp. 437-443, 2008/01/01 2007.
- [93] G. P. Anderson, S. C. Moreira, P. T. Charles, I. L. Medintz, E. R. Goldman, M. Zeinali, *et al.*, "TNT Detection Using Multiplexed Liquid Array Displacement Immunoassays," *Analytical Chemistry*, vol. 78, pp. 2279-2285, 2006/04/01 2006.
- [94] S. Y. Rabbany, W. J. Lane, W. A. Marganski, A. W. Kusterbeck, and F. S. Ligler, "Trace detection of explosives using a membrane-based displacement immunoassay," *Journal of Immunological Methods*, vol. 246, pp. 69-77, 2000.

- [95] R. C. Stringer, S. Gangopadhyay, and S. A. Grant, "Use of quantum dot-labeled imprinted polymer microparticles for detection of nitroaromatic compounds," pp. 767304-767304, 2010.
- [96] E. R. Goldman, A. L. Egge, I. L. Medintz, M. E. Lassman, and G. P. Anderson, "Application of a homogenous assay for the detection of 2,4,6-trinitrotoluene to environmental water samples," *ScientificWorldJournal*, vol. 5, pp. 445-51, May 23 2005.
- [97] E. L. Holthoff, D. N. Stratis-Cullum, and M. E. Hankus, "A Nanosensor for TNT Detection Based on Molecularly Imprinted Polymers and Surface Enhanced Raman Scattering," *sensors*, vol. 11, pp. 2700-2714, 2011.
- [98] M. Bhatt, J.-S. Zhao, F. Monteil-Rivera, and J. Hawari, "Biodegradation of cyclic nitramines by tropical marine sediment bacteria," *Journal of Industrial Microbiology and Biotechnology*, vol. 32, pp. 261-267, 2005.
- [99] D. Gao, Z. Wang, B. Liu, L. Ni, M. Wu, and Z. Zhang, "Resonance Energy Transfer-Amplifying Fluorescence Quenching at the Surface of Silica Nanoparticles toward Ultrasensitive Detection of TNT," *Analytical Chemistry*, vol. 80, pp. 8545-8553, 2008/11/15 2008.
- [100] H. Östmark, S. Wallin, and H. G. Ang, "Vapor Pressure of Explosives: A Critical Review," *Propellants, Explosives, Pyrotechnics*, vol. 37, pp. 12-23, 2012.
- [101] T. A. Skotheim, *Handbook of conducting polymers*: CRC press, 1997.
- [102] R. J. Young and P. A. Lovell, *Introduction to polymers*: CRC press, 2011.
- [103] G. Whitesides, J. Mathias, and C. Seto, "Molecular self-assembly and nanochemistry: a chemical strategy for the synthesis of nanostructures," *Science*, vol. 254, pp. 1312-1319, November 29, 1991 1991.
- [104] O. Ikkala and G. ten Brinke, "Functional Materials Based on Self-Assembly of Polymeric Supramolecules," *Science*, vol. 295, pp. 2407-2409, March 29, 2002 2002.

- [105] M. D. Wang, H. Yin, R. Landick, J. Gelles, and S. M. Block, "Stretching DNA with optical tweezers," *Biophysical Journal*, vol. 72, pp. 1335-1346, 3// 1997.
- [106] B. Maier and J. O. Rädler, "DNA on Fluid Membranes: A Model Polymer in Two Dimensions," *Macromolecules*, vol. 33, pp. 7185-7194, 2000/09/01 2000.
- [107] K. A. DILL, "Polymer principles and protein folding," *PRS*, vol. 8, pp. 1166-1180, 1999.
- [108] G. J. Hirasaki and G. A. Pope, "Analysis of Factors Influencing Mobility and Adsorption in the Flow of Polymer Solution Through Porous Media," 1974/8/1/.
- [109] A. Dobry and F. Boyer-Kawenoki, "Phase separation in polymer solution," *Journal of Polymer Science*, vol. 2, pp. 90-100, 1947.
- [110] E. F. Casassa, "Equilibrium distribution of flexible polymer chains between a macroscopic solution phase and small voids," *Journal of Polymer Science Part B: Polymer Letters*, vol. 5, pp. 773-778, 1967.
- [111] R. Xie, A. Karim, J. F. Douglas, C. C. Han, and R. A. Weiss, "Spinodal Dewetting of Thin Polymer Films," *Physical Review Letters*, vol. 81, pp. 1251-1254, 1998.
- [112] D. K. Owens and R. C. Wendt, "Estimation of the surface free energy of polymers," *Journal of Applied Polymer Science*, vol. 13, pp. 1741-1747, 1969.
- [113] D. Janssen, R. De Palma, S. Verlaak, P. Heremans, and W. Dehaen, "Static solvent contact angle measurements, surface free energy and wettability determination of various self-assembled monolayers on silicon dioxide," *Thin Solid Films*, vol. 515, pp. 1433-1438, 2006.
- [114] K. Venumadhav, Y. Minseong, R. Thiruvengadathan, K. D. Purnendu, G. Keshab, and G. Shubhra, "Entropy driven spontaneous formation of highly porous films from polymer–nanoparticle composites," *Nanotechnology*, vol. 20, p. 425602, 2009.
- [115] V. Korampally, V. K. Mamidi, B. Harris, K. Gangopadhyay, G. A. Baker, and S. Gangopadhyay, "Sub-minute formation of supported nanoporous mesoscale

- patterns programmed by surface energy," *Journal of Colloid and Interface Science*, vol. 364, pp. 546-554, 12/15/ 2011.
- [116] D. E. Laughlin and W. A. Soffa, "Spinodal Structures," in *Metals Handbook: Metallography and Microstructures*. vol. 9, J. Newby and K. Mills, Eds., ed: American Society for Metals, 1985.
- [117] E. Favvas and A. Mitropoulos, "What is spinodal decomposition?," *Journal of Engineering Science and Technology Review*, vol. 1, pp. 25-27, February 20, 2008.
- [118] B. J. Schwartz, "Conjugated polymers as molecular materials: how chain conformation and film morphology influence energy transfer and interchain interactions," *Annu Rev Phys Chem*, vol. 54, pp. 141-72, 2003.
- [119] S. Rochat and T. M. Swager, "Conjugated Amplifying Polymers for Optical Sensing Applications," *ACS Applied Materials & Interfaces*, vol. 5, pp. 4488-4502, 2013/06/12 2013.
- [120] I. D. W. Samuel, G. Rumbles, and C. J. Collison, "Efficient interchain photoluminescence in a high-electron-affinity conjugated polymer," *Physical Review B*, vol. 52, pp. R11573-R11576, 1995.
- [121] C. Deng, Q. He, C. He, L. Shi, J. Cheng, and T. Lin, "Conjugated Polymer-Titania Nanoparticle Hybrid Films: Random Lasing Action and Ultrasensitive Detection of Explosive Vapors," *The Journal of Physical Chemistry B*, vol. 114, pp. 4725-4730, 2010/04/08 2010.
- [122] M. Zheng, F. Bai, and D. Zhu, "Photophysical process of MEH-PPV solution," *Journal of Photochemistry and Photobiology A: Chemistry*, vol. 116, pp. 143-145, 1998.
- [123] J. C. Scott, J. H. Kaufman, P. J. Brock, R. DiPietro, J. Salem, and J. A. Goitia, "Degradation and failure of MEH-PPV light-emitting diodes," *Journal of Applied Physics*, vol. 79, pp. 2745-2751, 1996.
- [124] G. D. Hale, S. J. Oldenburg, and N. J. Halas, "Effects of photo-oxidation on conjugated polymer films," *Applied Physics Letters*, vol. 71, pp. 1483-1485, 1997.

- [125] M. Atreya, S. Li, E. T. Kang, K. G. Neoh, Z. H. Ma, K. L. Tan, *et al.*, "Stability studies of poly(2-methoxy-5-(2'-ethyl hexyloxy)-p- (phenylene vinylene) [MEH-PPV]," *Polymer Degradation and Stability*, vol. 65, pp. 287-296, 1999.
- [126] J. Yu, D. Hu, and P. F. Barbara, "Unmasking Electronic Energy Transfer of Conjugated Polymers by Suppression of O<sub>2</sub> Quenching," *Science*, vol. 289, pp. 1327-1330, August 25, 2000 2000.
- [127] D. Ghosh, G. S. Samal, A. K. Biswas, and Y. N. Mohapatra, "Laser-induced degradation studies of photoluminescence of PPV and CNPPV thin films," *Thin Solid Films*, vol. 477, pp. 162-168, 2005.
- [128] S. H. Kwon, S. Y. Paik, O. J. Kwon, and J. S. Yoo, "Triple-layer passivation for longevity of polymer light-emitting diodes," *Applied Physics Letters*, vol. 79, pp. 4450-4452, 2001.
- [129] F. Cucinotta, F. Carniato, G. Paul, S. Bracco, C. Bisio, S. Caldarelli, *et al.*, "Incorporation of a Semiconductive Polymer into Mesoporous SBA-15 Platelets: Toward New Luminescent Hybrid Materials," *Chemistry of Materials*, vol. 23, pp. 2803-2809, 2011/06/14 2011.
- [130] J. Toušek, J. Toušková, Z. Remeš, J. Čermák, J. Kousal, D. Kindl, *et al.*, "Exciton diffusion length and concentration of holes in MEH-PPV polymer using the surface voltage and surface photovoltage methods," *Chemical Physics Letters*, vol. 552, pp. 49-52, 2012.
- [131] J. R. Lakowicz, "Radiative decay engineering 5: metal-enhanced fluorescence and plasmon emission," *Analytical Biochemistry*, vol. 337, pp. 171-194, 2005.
- [132] P. Andrew, G. A. Turnbull, I. D. W. Samuel, and W. L. Barnes, "Photonic band structure and emission characteristics of a metal-backed polymeric distributed feedback laser," *Applied Physics Letters*, vol. 81, pp. 954-956, 2002.
- [133] M. Reufer, S. Riechel, J. M. Lupton, J. Feldmann, U. Lemmer, D. Schneider, *et al.*, "Low-threshold polymeric distributed feedback lasers with metallic contacts," *Applied Physics Letters*, vol. 84, pp. 3262-3264, 2004.

- [134] I. Samuel and G. Turnbull, "Organic semiconductor lasers," *Chemical Reviews-Columbus*, vol. 107, pp. 1272-1295, 2007.
- [135] M. S. Griffo, S. A. Carter, and A. L. Holt, "Enhanced photoluminescence of conjugated polymer thin films on nanostructured silver," *Journal of Luminescence*, vol. 131, pp. 1594-1598, 2011.
- [136] L. Danos, R. Greef, and T. Markvart, "Efficient fluorescence quenching near crystalline silicon from Langmuir–Blodgett dye films," *Thin Solid Films*, vol. 516, pp. 7251-7255, 2008.
- [137] J. Bühler, F.-P. Steiner, and H. Baltes, "Silicon dioxide sacrificial layer etching in surface micromachining," *Journal of Micromechanics and Microengineering*, vol. 7, p. R1, 1997.
- [138] Honeywell. (2001, August 26). *Modified and Improved BOEs*. Available: [http://www51.honeywell.com/sm/em/common/documents/2.4.7\\_metal\\_etching.pdf](http://www51.honeywell.com/sm/em/common/documents/2.4.7_metal_etching.pdf)
- [139] C. A. Schneider, W. S. Rasband, and K. W. Eliceiri, "NIH Image to ImageJ: 25 years of image analysis," *Nat Meth*, vol. 9, pp. 671-675, 2012.
- [140] J. N. Hilfiker, N. Singh, T. Tiwald, D. Convey, S. M. Smith, J. H. Baker, *et al.*, "Survey of methods to characterize thin absorbing films with Spectroscopic Ellipsometry," *Thin Solid Films*, vol. 516, pp. 7979-7989, 2008.
- [141] M. Tammer and A. P. Monkman, "Measurement of the Anisotropic Refractive Indices of Spin Cast Thin Poly(2-methoxy-5-(2'-ethyl-hexyloxy)-p-phenylenevinylene) (MEH-PPV) Films," *Advanced Materials*, vol. 14, pp. 210-212, 2002.
- [142] K.-X. Ma, C.-H. Ho, F. Zhu, and T.-S. Chung, "Investigation of surface energy for organic light emitting polymers and indium tin oxide," *Thin Solid Films*, vol. 371, pp. 140-147, 2000.
- [143] Y. Shi, J. Liu, and Y. Yang, "Device performance and polymer morphology in polymer light emitting diodes: morphology dependent emission spectra," *Macromolecular Symposia*, vol. 154, pp. 187-198, 2000.

- [144] Y. Shi, J. Liu, and Y. Yang, "Device performance and polymer morphology in polymer light emitting diodes: The control of thin film morphology and device quantum efficiency," *Journal of Applied Physics*, vol. 87, pp. 4254-4263, 2000.
- [145] M. Jørgensen, K. Norrman, and F. C. Krebs, "Stability/degradation of polymer solar cells," *Solar Energy Materials and Solar Cells*, vol. 92, pp. 686-714, 2008.
- [146] D. A. G. Bruggeman, "Berechnung verschiedener physikalischer Konstanten von heterogenen Substanzen. I. Dielektrizitätskonstanten und Leitfähigkeiten der Mischkörper aus isotropen Substanzen," *Annalen der Physik*, vol. 416, pp. 636-664, 1935.
- [147] O. Mirzov and I. G. Scheblykin, "Photoluminescence spectra of a conjugated polymer: from films and solutions to single molecules," *Physical Chemistry Chemical Physics*, vol. 8, pp. 5569-5576, 2006.
- [148] S. C. Kitson, W. L. Barnes, J. R. Sambles, and N. P. K. Cotter, "Excitation of molecular fluorescence via surface plasmon polaritons," *Journal of Modern Optics*, vol. 43, pp. 573-582, 1996/03/01 1996.
- [149] R. Aroca, G. J. Kovacs, C. A. Jennings, R. O. Loutfy, and P. S. Vincett, "Fluorescence enhancement from Langmuir-Blodgett monolayers on silver island films," *Langmuir*, vol. 4, pp. 518-521, 1988/05/01 1988.
- [150] T.-Q. Nguyen, I. B. Martini, J. Liu, and B. J. Schwartz, "Controlling interchain interactions in conjugated polymers: The effects of chain morphology on exciton-exciton annihilation and aggregation in MEH-PPV films," *The Journal of Physical Chemistry B*, vol. 104, pp. 237-255, 2000.
- [151] J. L. Lebowitz and H. Spohn, "Microscopic basis for Fick's law for self-diffusion," *Journal of Statistical Physics*, vol. 28, pp. 539-556, 1982/07/01 1982.
- [152] D. B. Jaynes and A. S. Rogowski, "Applicability of Fick's Law to Gas Diffusion1," *Soil Sci. Soc. Am. J.*, vol. 47, pp. 425-430, 1983 1983.
- [153] S. Webb and K. Pruess, "The Use of Fick's Law for Modeling Trace Gas Diffusion in Porous Media," *Transport in Porous Media*, vol. 51, pp. 327-341, 2003/06/01 2003.

- [154] M. R. Baklanov and K. P. Mogilnikov, "Non-destructive characterisation of porous low-k dielectric films," *Microelectronic Engineering*, vol. 64, pp. 335-349, 10// 2002.
- [155] J. Crank, "The mathematics of diffusion," 1975.
- [156] S. Clark, J. Dinan, L. Henning, M. Berg, P. White, and D. Cooper, "Soil Screening Guidance: User's Guide Attachment C: Chemical Properties for SSL Development," U. S. E. P. Agency, Ed., 2 ed. Washington, DC: Office of Solid Waste and Emergency Response, 1996.
- [157] S. W. Thomas, G. D. Joly, and T. M. Swager, "Chemical Sensors Based on Amplifying Fluorescent Conjugated Polymers," *Chemical Reviews*, vol. 107, pp. 1339-1386, 2007/04/01 2007.
- [158] Y. Li, Y. Cao, J. Gao, D. Wang, G. Yu, and A. J. Heeger, "Electrochemical properties of luminescent polymers and polymer light-emitting electrochemical cells," *Synthetic Metals*, vol. 99, pp. 243-248, 1999.
- [159] L. Meites, P. Zuman, and E. B. Rupp, *CRC Handbook Series in Organic Electrochemistry*: CRC press, 1977.
- [160] H. C. Bailey and R. J. Spanggord, "The relationship between the toxicity and structure of nitroaromatic chemicals," in *Aquatic Toxicology and Hazard Assessment, 6th Symposium, ASTM STP*, 1983, pp. 98-107.
- [161] M. Ramírez, H. Félix-Rivera, R. Sánchez-Cuprill, and S. Hernández-Rivera, "Thermal-spectroscopic characterization of acetone peroxide and acetone peroxide mixtures with nitrocompounds," *Journal of Thermal Analysis and Calorimetry*, vol. 102, pp. 549-555, 2010/11/01 2010.
- [162] H. Diez-y-Riega and H. Eilers, "Spectroscopic observation of neutral carbon during photodissociation of explosive-related compounds in the vapor phase," *Applied Optics*, vol. 52, pp. 7083-7093, 2013/10/10 2013.
- [163] W. M. Meylan, *Handbook of: Physical Properties of Organic Chemicals*: CRC Press, 1997.

- [164] A. Pokhriyal, M. Lu, V. Chaudhery, C.-S. Huang, S. Schulz, and B. T. Cunningham, "Photonic crystal enhanced fluorescence using a quartz substrate to reduce limits of detection," *Opt. Express*, vol. 18, pp. 24793-24808, 2010.
- [165] B. Van Dorst, J. Mehta, K. Bekaert, E. Rouah-Martin, W. De Coen, P. Dubrule, *et al.*, "Recent advances in recognition elements of food and environmental biosensors: A review," *Biosensors and Bioelectronics*, vol. 26, pp. 1178-1194, 2010.
- [166] S. Xiao, M. Nguyen, X. Gong, Y. Cao, H. Wu, D. Moses, *et al.*, "Stabilization of Semiconducting Polymers with Silsesquioxane," *Advanced Functional Materials*, vol. 13, pp. 25-29, 2003.
- [167] E. W. Olle, J. Messamore, M. P. Deogracias, S. D. McClintock, T. D. Anderson, and K. J. Johnson, "Comparison of antibody array substrates and the use of glycerol to normalize spot morphology," *Experimental and Molecular Pathology*, vol. 79, pp. 206-209, 2005.
- [168] P. Wu, Grainger, and D. W., "Comparison of hydroxylated print additives on antibody microarray performance," *Journal of Proteome Research*, vol. 5, p. 10, 2006.
- [169] M. Seidel and R. Niessner, "Automated analytical microarrays: a critical review," *Analytical and Bioanalytical Chemistry*, vol. 391, pp. 1521-1544, 2008.
- [170] C. A. Rowe-Taitt, J. W. Hazzard, K. E. Hoffman, J. J. Cras, J. P. Golden, and F. S. Ligler, "Simultaneous detection of six biohazardous agents using a planar waveguide array biosensor," *Biosensors and Bioelectronics*, vol. 15, pp. 579-589, 2000.
- [171] A. Y. Rubina, V. I. Dyukova, E. I. Dementieva, A. A. Stomakhin, V. A. Nesmeyanov, E. V. Grishin, *et al.*, "Quantitative immunoassay of biotoxins on hydrogel-based protein microchips," *Analytical Biochemistry*, vol. 340, pp. 317-329, 2005.
- [172] C. M. Salisbury, D. J. Maly, and J. A. Ellman, "Peptide Microarrays for the Determination of Protease Substrate Specificity," *Journal of the American Chemical Society*, vol. 124, pp. 14868-14870, 2002.

- [173] D. N. Gosalia, C. M. Salisbury, D. J. Maly, J. A. Ellman, and S. L. Diamond, "Profiling serine protease substrate specificity with solution phase fluorogenic peptide microarrays," *PROTEOMICS*, vol. 5, pp. 1292-1298, 2005.
- [174] S. V. Rao, K. W. Anderson, and L. G. Bachas, "Oriented immobilization of proteins," *Microchimica Acta*, vol. 128, pp. 127-143, 1998.
- [175] B. T. Houseman, E. S. Gawalt, and M. Mrksich, "Maleimide-Functionalized Self-Assembled Monolayers for the Preparation of Peptide and Carbohydrate Biochips†," *Langmuir*, vol. 19, pp. 1522-1531, 2002.
- [176] M. L. Frisk, W. H. Tepp, E. A. Johnson, and D. J. Beebe, "Self-Assembled Peptide Monolayers as a Toxin Sensing Mechanism within Arrayed Microchannels," *Analytical Chemistry*, vol. 81, pp. 2760-2767, 2009.
- [177] W. Kusnezow and J. D. Hoheisel, "Solid supports for microarray immunoassays," *Journal of Molecular Recognition*, vol. 16, pp. 165-176, 2003.
- [178] M. Uttamchandani, J. L. Neo, B. N. Z. Ong, and S. Moochhala, "Applications of microarrays in pathogen detection and biodefence," *Trends in Biotechnology*, vol. 27, pp. 53-61, 2009.
- [179] CDC1. (2010, December, 30). *Bioterrorism Agents/Diseases: By Category*. Available: <http://www.bt.cdc.gov/agent/agentlist-category.asp#catdef>
- [180] D. M. Gill, "Bacterial toxins: a table of lethal amounts," *Microbiological Reviews*, vol. 46, pp. 86-94, March 1982 1982.
- [181] C. Montecucco and G. Schiavo, "Structure and function of tetanus and botulinum neurotoxins.," *Quarterly Reviews in Biophysics.*, vol. 28, pp. 423-72, November 1995.
- [182] AOAC, "Official Methods of Analysis," in *17.7.01*, A. International, Ed., 17 ed. Gaithersburg, MD, 2000.

- [183] K. Bagramyan, J. R. Barash, S. S. Arnon, and M. Kalkum, "Attomolar Detection of Botulinum Toxin Type A in Complex Biological Matrices," *PLoS ONE*, vol. 3, p. e2041, 2008.
- [184] J. L. Ferreira, S. Maslanka, E. Johnson, and M. Goodnough, *Detection of botulinal neurotoxins A, B, E, and F by amplified enzyme-linked immunosorbent assay: Collaborative study* vol. 86. Gaithersburg, MD: AOAC International, 2003.
- [185] J. R. Barr, H. Moura, A. E. Boyer, A. R. Woolfitt, S. R. Kalb, A. Pavlopoulos, *et al.* (2005, December 30, 2010). Botulinum Neurotoxin Detection and Differentiation by Mass Spectrometry. *Emerging Infectious Diseases*. Available: <http://www.cdc.gov/ncidod/EID/vol11no10/04-1279.htm>
- [186] K. E. Sapsford, S. Sun, J. Francis, S. Sharma, Y. Kostov, and A. Rasooly, "A fluorescence detection platform using spatial electroluminescent excitation for measuring botulinum neurotoxin A activity," *Biosensors and Bioelectronics*, vol. 24, pp. 618-625, 2008.
- [187] M. Pires-Alves, M. Ho, K. K. Aberle, K. D. Janda, and B. A. Wilson, "Tandem fluorescent proteins as enhanced FRET-based substrates for botulinum neurotoxin activity," *Toxicon*, vol. 53, pp. 392-399, 2009.
- [188] N. M. Green, "Avidin," in *Advances in Protein Chemistry*. vol. Volume 29, J. J. T. E. C.B. Anfinsen and M. R. Frederic, Eds., ed: Academic Press, 1975, pp. 85-133.
- [189] D. T. Denhardt, "A membrane-filter technique for the detection of complementary DNA," *Biochemical and Biophysical Research Communications*, vol. 23, pp. 641-646, 1966.
- [190] J. P. Baker, H. W. Blanch, and J. M. Prausnitz, "Swelling properties of acrylamide-based amphotolytic hydrogels: comparison of experiment with theory," *Polymer*, vol. 36, pp. 1061-1069, 1995.

## **VITA**

Charles M. Darr (Chase) was born on November 2, 1984 in Little Rock, Arkansas. Chase received his Bachelor of Science degree in Biological Engineering from the University of Arkansas, Fayetteville, Arkansas, in 2006, where he was a Chancellor's Scholar and Sanford M. Wilbourn Biomedical Scholarship recipient. His senior design project, "A Children's Mobile Feeding Tube Device", was carried out with John Leach and Andrew Riester under the advisement of Dr. Thomas Costello. This project won 1<sup>st</sup> Place in the 2006 Gunlogson Environmental Design Competition at the annual ASABE national conference in Portland, Oregon. Chase then received his Masters of Science degree in Biomedical Engineering from the University of Arkansas in 2009 under the advisement of Dr. Jin-Woo Kim. He was married to Kathryn (neé Murphy) in July 2009 and joined the University of Missouri, Columbia, Missouri, in August 2009 with Dr. Shubhra Gangopadhyay and Dr. Luis Polo-Parada as co-advisors. He will be receiving his Ph.D. in Bioengineering from the University of Missouri, Columbia, Missouri, in December 2014. His current research interests include the study of the interface between nanomaterials and biological molecules, optical-based biosensors, and, more specifically, the application of nano-enabled biosensors for the early detection and elimination of cancer. Chase plans to continue pursuing these research areas in the future as well as using the knowledge, skills, and wisdom gained throughout his graduate career to educate and stimulate young minds toward interest, excellence, and advise them on the possibility of a career in science and engineering. Chase and Katie are due to have their first daughter in January 2015.